Stony Brook University

Magnetic Component of Strongly Coupled Quark-Gluon Plasma

A Dissertation Presented

by

Jinfeng Liao

to

The Graduate School

in Partial Fulfillment of the Requirements

for the Degree of

Doctor of Philosophy

in

Physics

Stony Brook University

August 2008

Stony Brook University

The Graduate School

Jinfeng Liao

We, the dissertation committee for the above candidate for the Doctor of Philosophy degree, hereby recommend acceptance of this dissertation.

Edward Shuryak – Dissertation Advisor
Professor, Department of Physics and Astronomy

Alfred Goldhaber – Chairperson of Defense
Professor, C. N. Yang Institute for Theoretical Physics

Thomas Hemmick
Professor, Department of Physics and Astronomy

Raju Venugopalan
Senior Scientist
Brookhaven National Laboratory

This dissertation is accepted by the Graduate School.

Lawrence Martin
Dean of the Graduate School

Abstract of the Dissertation

Magnetic Component of Strongly Coupled Quark-Gluon Plasma

by

Jinfeng Liao

Doctor of Philosophy

in

Physics

Stony Brook University

2008

In this dissertation we propose a new view of finite $T-\mu$ QCD based on a competition between *electrically* and *magnetically* charged quasiparticles (to be referred to as EQPs and MQPs below). That is, the QGP has a usual electric component and a magnetic component as well: the two components have their properties, like constituent mass/density/couping, changing with $T-\mu$, and different components become dominant in different regions. In particular we conjecture an equilibrium line between the two components and show that the strongly coupled quark-gluon plasma (sQGP) in 1-2T_c, which covers the equilibrium point at about 1.5T_c, has an important magnetic component which is a good liquid. We call it the magnetic scenario for sQGP.

In Part I, including Chapter 2-5, we present our study of the magnetic component of sQGP. In Chapter 2, single monopole motion in a few physically interesting configurations of electric field is studied, both classically and quantum mechanically. In Chapter 3, we report the details of our Molecular Dynamics (MD) simulations for

a strongly coupled plasma with both electric and magnetic charges and present MD results for the transport properties. Chapter 4 is dedicated to investigating the liquid nature of the magnetic component by applying our MD results and by analyzing recent lattice data. Chapter 5 shows how the magnetic scenario we proposed can help explain the very nontrivial static $\bar{Q}Q$ potentials at $T \approx T_c$ as measured in lattice calculations.

In Part II, including Chapter 6-7, we examine the electric component of sQGP. In Chapter 6 we will use the finite T potential model to calculate bound states of quarks and gluons beyond the binary, i.e. baryons, glueballs and polymer chains in sQGP. In Chapter 7 we use the lattice results of baryonic susceptibilities as a diagnosis to probe the quark, diquark and baryon contents in sQGP.

To the memory of my mother.

Contents

List of Figures

List of Tables

Acknowledgements

My four years at Stony Brook as a PhD student have been so wonderful, only because of the many people I am so indebted to.

First of all I thank my advisor, Edward Shuryak. Working with him is a unique experience. His penetrating intuition and lightening ideas are invaluable sources without which the present dissertation couldn't have been done. While Derek acknowledged that in his dissertation with the term "His crazy ideas", I'd like to make it fair by commenting that "His crazy ideas" are perfectly suited for the sQGP (which is such a crazy system after all) physics and have been advancing the whole field.

I also thank Gerry Brown. His tireless efforts to teach us students all kinds of physics, especially during the lunch discussions, have indeed broadened and sharpened my understanding of physics in general. In particular I appreciate his warm-hearted help on the career of young students like me.

I want to thank all the rest of the nuclear theory group. My research benefitted very much from the intensive and instructive discussions with Tom Kuo, Ismail Zahed, Jac Verbaarschot, and Derek Teaney. Their many critical questions during my many talks at our group also helped me to improve the work as well as the presentation. My thanks go to Claudia Ratti and Michael Lublinsky for their many helps on my research as well as on my application for postdoc. I also want to say thank you to Enrique Moreno-Mendez and Jeremy Holt with whom I shared not only the same office but also the numerous delightful conversations inside and outside physics. I also thank all the other fellow students (and some experimental students as well) for interesting discussions, in particular Shu Lin, Clint Young, Keun-Young Kim, Kevin Dusling, Sung-Tae Cho, John Chen and Rei Wei. I am grateful to Boris Gelman (our former postdoc) for important help on the MD simulations and discussions about transport coefficients and to Jorge Casalderrey-Solana (our former student) for discussions on hydro and jet physics.

I'd like to thank Fred Goldhaber, Tom Hemmick, Raju Venugopalan, Volker Koch, Xin-Nian Wang and Nu Xu for the various discussions and helps. Especially I want to take this chance to thank Pengfei Zhuang, my former advisor

for BS and MS at Tsinghua: without you and Xiaozhong's continuous help and encouragement, I couldn't have gone so far along this road.

I am grateful to our secretary Diane Aveni for many helps. I also thank the main office crew, in particular Pat Peiliker whose help was essential during my early months at Stony Brook.

There are still many wonderful friends that I need to thank, in particular: Zhongkui Tan, Shu Lin, Qiuzhe Xie and Li Cui, Yan Zhang, Rui Wei, Tao Sun, Lei Zhu, Jingbin Li and John Chen. While my academical life involves only the three colors of QCD, you guys have made my daily life as colorful as the rainbow!

It would be impossible at all to finish such a big project (i.e. PhD) without the endless support from family. I am so indebted to my parents-in-law who came here for more than a year helping us to survive the toughest time after the birth of my daughter: without them being here, the hard core of this dissertation (the paper PRC75:054907,2007.) could not have been produced. I want to say thank you to my father for his support and patience to eventually see me achieving the highest academic degree.

I should thank Brooke even though she can't read the words yet. To be frank, she is a huge "drag" to my research, but on top of that she brings enormous joys and surprises to me and makes all the hard time worthy of it. I appreciate this most wonderful gift from my Stony Brook years, as the name "Brooke" marks it permanently.

Finally, and most most importantly, I acknowledge the priceless love and support from Yi. She was brave enough to quit her nice job at Beijing about three years ago and came to accompany me across the "murky" tunnel toward PhD. She contributed significantly to the endeavor for the title Dr. and even brought me the great little Brooke. Without her, not only this dissertation couldn't have been finished, but the whole life would not be as meaningful any more.

Chapter 1

Introduction

1.1 Quantum Chromodynamics and Quark-Gluon Plasma

Quantum Chromodynamics (QCD) is the fundamental theory of the strong interaction. It is a non-Abelian gauge theory, with symmetry group $SU(N_c)$ (N_c=3). The matter content includes $N_f = 6$ flavors of quarks, named u, d, s, c, b, t. The most nontrivial feature of QCD, and of many QCD-like non-Abelian theories (say theories with different N_c, N_f from QCD), is the asymptotic freedom, which in very naive terms says the running coupling becomes weak at very high energy scale (or very small space-time distance). Asymptotic freedom has been firmly established experimentally, and in that regime perturbative calculations (pQCD) are reliable and successful.

However this feature of the QCD beta function also indicates that at low enough energy scale, which occurs more often in nature (say in normal nuclei), the coupling inevitably runs to be strong, leading to very rich nonperturbative dynamics. One most distinct of these phenomena is that the perturbative degrees of freedom, i.e. the quarks and gluons in the Lagrangian, actually does not appear in the physical spectrum of the QCD vacuum. Instead hundreds of hadrons, normally baryons and mesons, are found experimentally, and these hadrons could be explained as various bound states of quarks and gluons.

Actually it was clear to physicists from its "infant stage" that the QCD vacuum is a very complicated condensed matter. In particular the QCD vacuum is characterized by two famous phenomena: 1) color confinement, i.e. colored objects like a single quark or gluon are never observed to propagate freely in the vacuum and are thus conjectured to be permanently confined inside color neutral states like hadrons; 2) the spontaneous breaking of (approximate) chiral symmetry for light quark sector (i.e. u, d quarks). While the

nature of the latter was more or less understood as an instanton effect (e.g. in the instanton liquid model), the former has been standing as a challenge for decades and remains mysterious. The difficulty is, as we emphasize, not only that the coupling is so strong that perturbation theory is not applicable, but that we are even *not* so sure what is the relevant degrees of freedom for the phenomenon (like the instanton for chiral symmetry breaking). Monopoles are believed to be the "player" for confinement via the dual superconductor picture and have been studied on the lattice for many years. We will come to more discussions along this line in the next section.

A very good introduction covering most of the subjects in this section with further references can be found in e.g.[1].

1.1.1 Quark-Gluon Plasma and the QCD Phase Diagram

Due to these difficulties in understanding the QCD vacuum, physicists started around the 70's to think about "violently" exciting the vacuum to such a degree that the QCD fundamental particles, i.e. quarks and gluons, will be the direct dynamical objects. Theoretically it was first shown by Edward Shuryak (who also invented the name) [2][3] that the quark-gluon plasma (QGP) is a high-temperature phase of QCD, in which free color charges are screened by the medium rather than confined in neutral objects. Furthermore according to asymptotic freedom for high enough temperature $T >> \Lambda_{QCD}$ this phase is expected to become *weakly* coupled (wQGP), with most of interactions characterized by small coupling $\alpha_s(p \sim T) << 1$. In this domain wQGP is essentially a near-ideal gas of its fundamental constituents, quarks and gluons.

These thoughts have developed into detailed studies of QCD thermodynamics, i.e. the various properties of QCD matter under given external conditions like temperature T and baryonic density n_B or equivalently the baryonic chemical potential μ_B. The most important tool for these studies is the lattice QCD, or lattice gauge theory in general. With more than thirty years of accumulation and with the skyrocketing computer power, lattice calculation has become a major method, and in many cases the only way, of producing reliable nonperturbative results. Today QCD thermodynamics at $\mu = 0$ has been thoroughly explored by lattice practitioners, while its nonzero μ domain became approachable on the lattice only recently.

In QCD thermodynamics, the most interesting questions are related to possible QCD phase transitions: it is expected that with increasing T and/or μ, there should be a deconfinement phase transition as well as a chiral restoration, with quarks/gluons being librated from hadrons upon the former and with

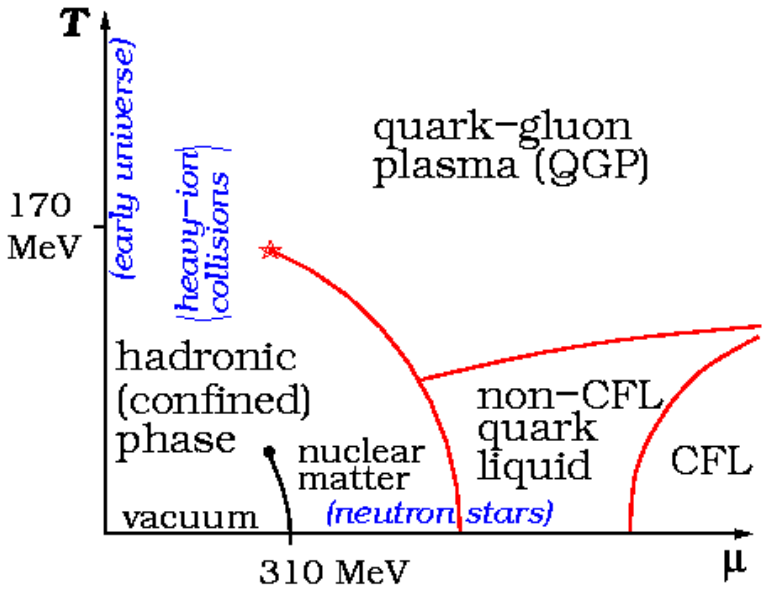

Figure 1.1: A schematic QCD phase diagram, the horizontal axis is quark chemical potential $\mu_q = \mu_B/3$. (from http://en.wikipedia.org/wiki/Image:QCD_phase_diagram.png)

light quarks coming back to their current masses (from Lagrangian) rather than the constituent masses upon the latter. Without explicit reasons, the two transitions (as shown by lattice calculations) seem to happen about the same critical temperature T_c and/or chemical potential μ_c. With two external parameters $T - \mu$ one can have a QCD phase diagram, telling what phase the QCD matter is in at given $T - \mu$. Current understanding of QCD phase diagram can be summarized in Fig.1.1.

1.1.2 Relativistic Heavy Ion Collisions

QGP is experimentally studied via heavy ion collisions, at CERN SPS and last years at BNL RHIC collider, at temperatures reaching up to about $T \approx 2T_c$.

Taking RHIC as an example, two beams of gold nuclei are accelerated to very high energy and then guided to collide with a center-of-mass energy $\sqrt{s} = 200GeV$ per nucleon. The space-time evolution of RHIC collision is generally believed to be the following: two high energy nuclei, extremely Lorentz contracted and in the form of Color Glass Condensate(CGC)[4][5], collide violently, and after the collision point most leading nucleons fly apart with a lot of energy deposited in the collision zone, creating a fireball longitudinally

expanding very fast; due to certain mechanism, the fireball reaches thermal equilibrium at the scale of $1fm$, after which pressure develops and transverse flow starts; due to expansion the system cools down, and the QGP phase (at $T > T_c$) lasts for about $4-5fm$, after which a mixed phase at $T_c \approx 170MeV$ starts and again lasts for about $4-5fm$; finally the system cools into the hadronic rescattering stage for about $4-5fm$, experiencing first a chemical freezeout (a point after which the abundance of each particle specie does not change anymore) at T a little less than T_c and a thermal freezeout (a point after which the system is so dilute that any scattering stops and particle p_T spectrum does not change further) at $T \approx 120MeV$.

There are four detectors at RHIC, including Phenix, Star, Brahms, and Phobos. A lot of data have been accumulated and analyzed since 2000. Their main discoveries are summarized in the RHIC white papers [6][7][8][9].

1.1.3 The Discovery of Strongly Coupled Quark-Gluon Plasma and Theoretical Developments

It became apparent around 2003 [10][11][12] that the quark-gluon plasma discovered at Relativistic Heavy Ion Collision (RHIC) is the most "perfect liquid" ever known. A new name was given to this strongly coupled quark-gluon plasma, sQGP. Theorists have since been taking the big challenge to explain the remarkable properties of sQGP with diverse approaches, ranging from those borrowed from classical plasmas to AdS/CFT duality: for recent reviews see [13][14]. Below we briefly summarize the major experimental discovery and the theoretical developments in understanding the discovery.

The Experimental Discovery of the "Perfect Liquid"

Success of hydrodynamical description [15][16][17][18] of observed collective flows have indicated, that all dissipative lengths are very short and thus the produced matter cannot be a weakly coupled gas but rather a near-perfect (small viscosity) liquid. These features are further complemented by very high jet losses and robust heavy quark charm (equilibration) observed, well beyond what pQCD predicted.

Collective flows, related with explosive behavior of hot matter, were observed at RHIC and studied in detail: the conclusion is that they are reproduced by the ideal hydrodynamics remarkably well. Indeed, although these flows affect different secondaries differently, yet their spectra are in quantitative agreement with the data for all of them, from π to Ω^-. At non-zero impact parameter the original excited system is deformed in the transverse

plane, creating the so called elliptic flow described by

$$v_2(s, p_t, M_i, y, b, A) =< cos(2\phi) > \tag{1.1}$$

where ϕ is the azimuthal angle and the others stand for the collision energy, transverse momentum, particle mass, rapidity, centrality and system size. Hydrodynamics explains all of those dependences, for about 99% of the particles[1].

Bound States in sQGP

Shuryak and Zahed [19] argued that marginally bound states create resonances which can strongly enhance transport cross section. Similar phenomenon does happen for ultracold trapped atoms, due to Feshbach-type resonances at which the binary scattering length $a \to \infty$, which was indeed shown to lead to a near-perfect liquid. van Hees, Greco and Rapp[20] studied $\bar{q}c$ resonances, and found enhancement of charm stopping.

Combining lattice data on quasiparticle masses and interparticle potentials, one finds a lot of quark and gluon bound states [21][22] which contribute to thermodynamical quantities and help explain the "pressure puzzle" [21], an apparent contradiction between heavy quasiparticles near T_c and rather large pressure.

Classical Molecular Dynamics for non-Abelian plasmas

Another direction, pioneered by Gelman et al [23], is to use experience of classical strongly coupled electromagnetic plasma. Their model for the description of strongly interacting quark and gluon quasiparticles as a classical and non-relativistic Non-Abelian Coulomb gas. The sign and strength of the inter-particle interactions are fixed by the scalar product of their classical *color vectors* subject to Wong's equations. The EoM for the phase space coordinates follow from the usual Poisson brackets:

$$\{x^m_{\alpha\, i}, p^n_{\beta\, j}\} = \delta^{mn}\delta_{\alpha\beta}\delta_{ij} \quad \{Q^a_{\alpha\, i}, Q^b_{\beta\, j}\} = f^{abc}\, Q^c_{\alpha\, i} \tag{1.2}$$

For the color coordinates they are classical analogue of the $SU(N_c)$ color commutators, with f^{abc} the structure constants of the color group. The classical color vectors are all adjoint vectors with $a = 1...(N_c^2 - 1)$. For the non-Abelian group SU(2) those are 3d vectors on a unit sphere, for SU(3) there are 8

[1]The remaining $\sim 1\%$ residing at larger transverse momenta $p_t > 2GeV$ are influenced by hard processes and jets.

dimensions minus 2 Casimirs=6 d.o.f.[2].

This cQGP model was studied using Molecular Dynamics (MD), the equations of motion were solved numerically for $n \sim 100$ particles. It also displays a number of phases as the Coulomb coupling is increased ranging from a gas, to a liquid, to a crystal with anti-ferromagnetic-like color ordering. The measured transport properties, when extrapolated to the sQGP parameters suggest that the phase is liquid-like, with a diffusion constant $D \approx 0.1/T$ and a shear viscosity to entropy density ratio $\eta/s \approx 1/3$. The second paper of the same group[24] discussed the energy and the screening at $\Gamma > 1$, finding large deviations from the Debye theory.

The first study combining classical MD with quantum treatment of the color degrees of freedom has been attempted by the Budapest group [25].

AdS/CFT

Another approach that has recently attracted much interest is related to the so called AdS/CFT correspondence between strongly coupled $\mathcal{N}$=4 supersymmetric Yang-Mills theory (a relative of QCD) and weakly coupled string theory in Anti-de-Sitter space (AdS) in the classical SUGRA regime. A few very interesting transport properties have been calculated via this method, for example, the shear viscosity, the energy loss drag coefficient, the diffusion constant, the jet quenching parameter, etc. The suggested values, as borrowed to QGP, give reasonable estimates for RHIC. While the applicability is under debate, the progress along this direction is very fast, see e.g. reviews in [13][14].

1.2 The Magnetic Scenario for sQGP

The main goal of this dissertation is to introduce a new view of finite $T - \mu$ QCD based on a competition between *electrically* and *magnetically* charged quasiparticles (to be referred to as EQPs and MQPs below). That is, the QGP has a usual electric component and a magnetic component as well: the two components have their properties, like constituent mass/density/coupling, changing with $T - \mu$, and different components become dominant in different regions. In particular our works to be presented will show that in sQGP regime the magnetic component is dominant and liquid-like. We call it the magnetic scenario for sQGP.

[2] Although color EoM does not look like the usual canonical relations between coordinates and momenta, they actually are pairs of conjugated variables, as can be shown via the so called Darboux parametrization, see [23] for details.

It is different from the traditional approach, which puts the *confinement* phenomenon at the center of the discussion, dividing the temperature regimes into two basic phases (as shown in Fig.1.1): (i) confined or hadronic phase at $T < T_c$, and (ii) deconfined or quark-gluon plasma (QGP) phase at $T > T_c$.

We, on the other hand, focus on the competition of EQPs and MQPs and divide the phase diagram differently, into (i) the "magnetically dominated" region at $T < T_{E=M}$ and (ii) "electrically dominated" one at $T > T_{E=M}$. In our opinion, the key aspect of the physics involved is the *coupling strength* of both interactions. So, a divider is some *E-M equilibrium* region at intermediate T-μ. Since it does *not* correspond to a singular line, one can define it in various ways: the most direct one is to use a condition that electric (e) and magnetic (g) couplings are equal

$$e^2/4\pi\hbar c = g^2/4\pi\hbar c = 1 \tag{1.3}$$

The last equality follows from the celebrated Dirac quantization condition [26]

$$\frac{eg}{4\pi\hbar c} = 1 \tag{1.4}$$

Besides equal couplings, the equilibrium region is also presumably characterized by comparable densities as well as masses of both electric and magnetic quasiparticles[3].

The "magnetic-dominated" low-T (and low-μ) region (i) can in turn be subdivided into the *confining* part (i-a) in which electric field is confined into quantized flux tubes surrounded by the condensate of MQPs, forming t'Hooft-Mandelstam "dual superconductor" [27] [28], and a new *"postconfinement"* region (i-b) at $T_c < T < T_{E=M}$ in which EQPs are still strongly coupled (correlated) and still connected by the electric flux tubes. We believe this picture better corresponds to a situation in which string-related physics is by no means terminated at $T = T_c$: rather it is at its maximum there. Then if leaving this "magnetic-dominated" region and passing through the equilibrium region by increase of T and/or μ, we enter either the high-T "electric-dominated" QGP or a color-electric superconductor at high-μ replacing the dual superconductor (with diquark condensate taking place of monopole condensate).

A new phase diagram explaining this viewpoint pictorially is shown in Fig.1.2. Below we explain the underlying physical thoughts in more details.

[3]Let us however remind the reader that the E-M duality is of course not exact, in particular EQPs are gluons and quarks with spin 1 and 1/2 while MQPs are spherically symmetric "hedgehogs" without any spin.

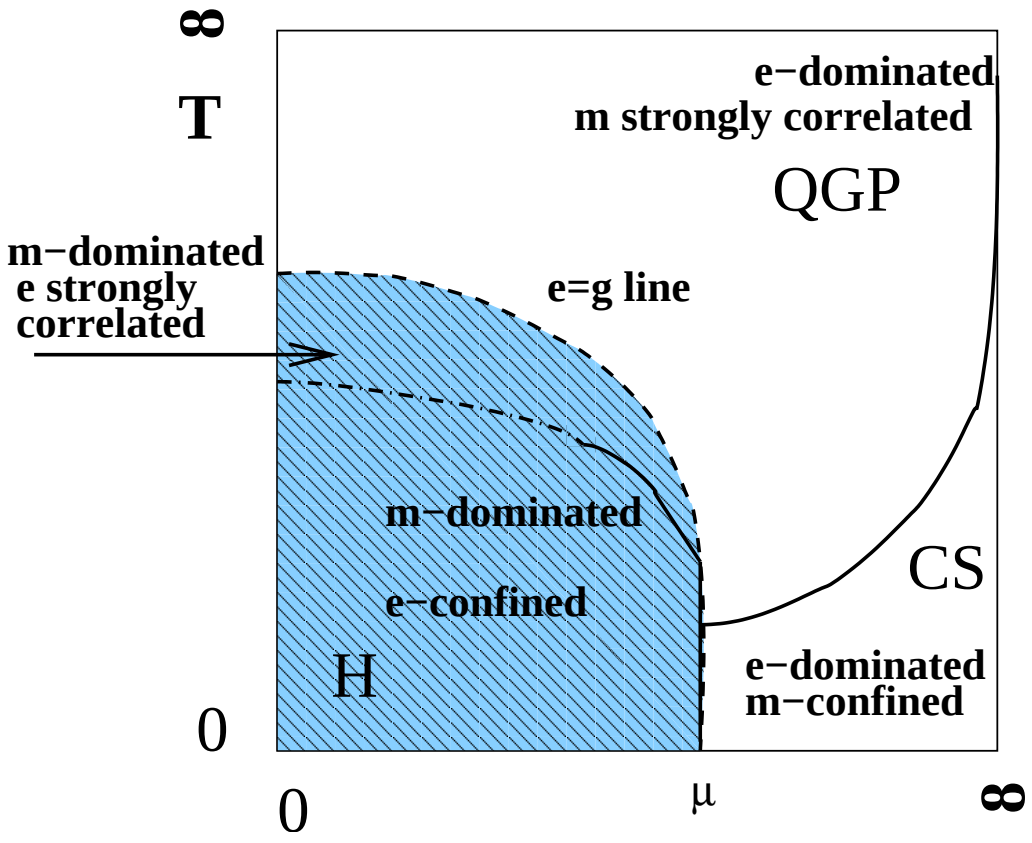

Figure 1.2: (color online) A schematic phase diagram on a ("compactified") plane of temperature and baryonic chemical potential $T-\mu$. The (blue) shaded region shows the "magnetically dominated" region $g < e$, which includes the e-confined hadronic phase as well as "postconfined" part of the QGP domain. The light region includes the "electrically dominated" part of QGP and also color superconductivity (CS) region, which has e-charged diquark condensates and therefore obviously m-confined. The dashed line called "e=g line" is the line of electric-magnetic equilibrium. The solid lines indicate true phase transitions, while the dash-dotted line is a deconfinement cross-over line.

1.2.1 Electric-magnetic dualities in supersymmetric theories

Progress in supersymmetric (SUSY) Quantum Field Theories was originally stimulated by a desire to get rid of perturbative divergencies and solve the so called hierarchy problems. However in the last 2 decades it went much further than just guesses of possible dynamics at superhigh energies. A fascinating array of nonperturbative phenomena have been discovered in this context, making them into an excellent theoretical laboratory. However we think that their relevance to QCD-like theories are neither understood not explored in a sufficient depth yet.

Studies of instantons in these theories have resulted in exact beta functions and other tools, which have allowed Seiberg to get quite complete picture of the phase structure of $\mathcal{N} = \infty$ SUSY gauge theories [29].

This was enhanced in the context of $\mathcal{N} = 2$ SUSY gauge theories by Seiberg and Witten [30], who were able to show how physical content of the theory changes as a function of Higgs VeVs (in a "moduli space" of possible vacua[4]). Singularities in moduli space were identified with the phase transitions, in which one of the MQPs gets massless. Seiberg and Witten have found a fascinating set of *dualities*, explaining where and how a transition from one language to another (e.g. from "electric" to "magnetic" to "dyonic" ones) can explain what is happening at the corresponding part of the moduli space, in the simplest and most natural way.

One lesson from those works, which is most important for us, is what happens with the strength of electric e and magnetic coupling g near the phase transition. As e.g. monopoles gets light and even massless at some point, the "Landau zero charge" in the IR is enforced by the $U(1)$ beta function of the magnetic QEDs, making them weakly coupled in IR, $g << 1$. The Dirac quantization (1.4) therefore demands that the electric coupling must get large $e >> 1$, enforcing the "strongly coupled" electric sector in this region.

Since two pillars of this argument – $U(1)$ beta function and Dirac quantization – do not depend on supersymmetry or any other details of the SW theory, we therefore now propose it to be a generic phenomenon. We thus conjecture it to be also true near the QCD deconfinement transition $T \approx T_c$, explaining why phenomenologically we see a strong coupling regime there.

The high-T limit, on the other hand, is similar to large-VEV domain of moduli space: here the $SU(N)$ asymptotic freedom in UV plus screening makes the electric charge small. Thus here MQPs are heavy and strongly coupled.

[4]The moduli space is the manifold spanned by the parameters labelling all the possible degenerate vacua.

1.2.2 Lessons from lattice gauge theory

Static potentials

One of the principal reasons we proposed to change the traditional viewpoint of putting confinement at the center, can be explained using lattice data on the $T-$dependence of the so called "static potentials". The traditional reasoning points to the free energy $F(r,T)$ associated with static quark pair separated by a distance r, and defines the deconfinement as the disappearance of a (linearly) growing "string" term in it, so that at $T>T_c$ there is a finite limit of the free energy at large distances, $F(\infty,T)$. This phenomenon has often been referred to as a "melting of the confining string" at T_c.

However, as explained by Polyakov nearly 3 decades ago [31], the string actually should not disappear at T_c: at this point its energy gets instead *compensated* by the entropy term so that the $free$ energy $F=U-TS$ vanishes. As detailed lattice studies revealed, in fact the energy and entropy associated with a static quark pair are strongly peaked exactly at $T\approx T_c$, see Fig.1.3. The potential energy is really huge there, reaching about 4 GeV(!), while the associated entropy reaches the equally impressive value of about 20. Nothing like that can be explained on the basis of Debye-screened weakly coupled gas of EQPs – the usual picture of QGP until few years ago. We think that the explanation of such large energy and huge number $\sim exp(20)$ of occupied states can only be obtained if several correlated quasiparticles are bound to heavy charges, presumably in the form of gluonic chains or "polymers" [22] conducting the electric flux from one charge to another.

Therefore, the "deconfinement" seen in disappearing linear term in free energy is actually restricted to static (or adiabatically slowly moving) charges, while for finite-frequency motion of light or even heavy (charmed) quarks one still should find mesonic bound states even in the deconfined phase [21]. Lattice studied of light quark and charmonium states [32][33] found that they indeed persist till $T\approx 2T_c$: this conclusion was dramatically confirmed by experimental discovery that J/ψ suppression at RHIC is smaller than expected and is consistent with a new view, that J/ψ is *not* melting at RHIC (where $T<2T_c$).

One set of well-known lattice studies have tried to answer the following questions: Is a "dual superconductor" picture consistent with what is observed on the lattice? In particular, is the shape and field distribution inside the confining strings in agreement with that in the Abrikosov flux tube of a superconductor (Abelian Higgs model)? As one can read e.g. in [34], the answer seems to be a definite yes. Can one define in some way monopoles and their paths, and are those (in average) consistent with dual Maxwell equations? As

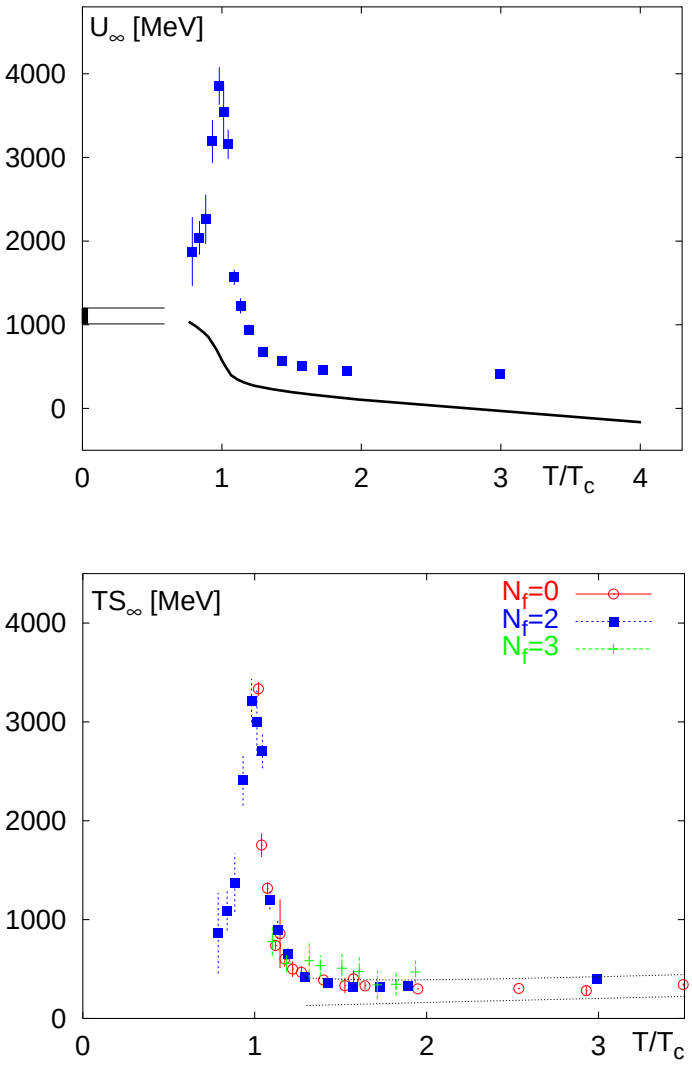

Figure 1.3: The energy (a) and entropy (b) (as $TS_\infty(T)$) derived from the free energy of two static quarks separated by large distance, in 2-flavor QCD (from arXiv:hep-lat/0510094).

one can read in e.g. [35], the answer seems to be also yes.

Unfortunately, those studies (as reviewed in [36]) were mostly concentrated in the vacuum $T = 0$, while we are interested in the deconfined plasma $T > T_c$. Is there any general reason to think that MQPs play an important role here as well? The most important argument[5] is the persistence of *static magnetic screening* at all T, up to infinitely high T.

Screening

Although static magnetic screening was shown to be absent in perturbative diagrams [37], it has been conjectured by Polyakov [31] to appear nonperturbatively at the "magnetic scale" which at high T is

$$\Lambda_M = e^2 T \tag{1.5}$$

The magnetic screening mass and monopole density should thus be

$$M_M = C_M \Lambda_M, \qquad n_M = C_n \Lambda_M^3 \tag{1.6}$$

with some numerical constants C_M, C_n.

To illustrate current lattice results, we show the T-dependence of the electric and magnetic screening masses calculated by Nakamura et al [38], see Fig.1.4. Note that electric mass is larger than magnetic one at high T, but vanishes at T_c (because here electric objects get too heavy and effectively disappear). The magnetic screening mass however grows toward T_c, which is consistent with its scaling estimate

$$M_M^2 \sim (e^2 T)^2 \tag{1.7}$$

(Another estimate of the magnetic screening can be done in the dual language as

$$M_M^2 \sim g^2 n_M / T \sim g^2 (e^2 T)^3 / T \tag{1.8}$$

which is a perturbative (small magnetic coupling g) loop: note that it agrees with the former one due to Dirac condition $e \sim 1/g$.)

If one uses screening masses to get an idea about density of electric and magnetic objects, one finds that the point at which electric and magnetic masses are equal should be close to the *E-M equilibrium* point we emphasized at the beginning of this section. This argument places the equilibrium

[5]Note a principal difference with all electromagnetic plasmas, which have no magnetic screening at all. For example, solar magnetic flux tubes are extended for a millions of km, with unimpeded flux.

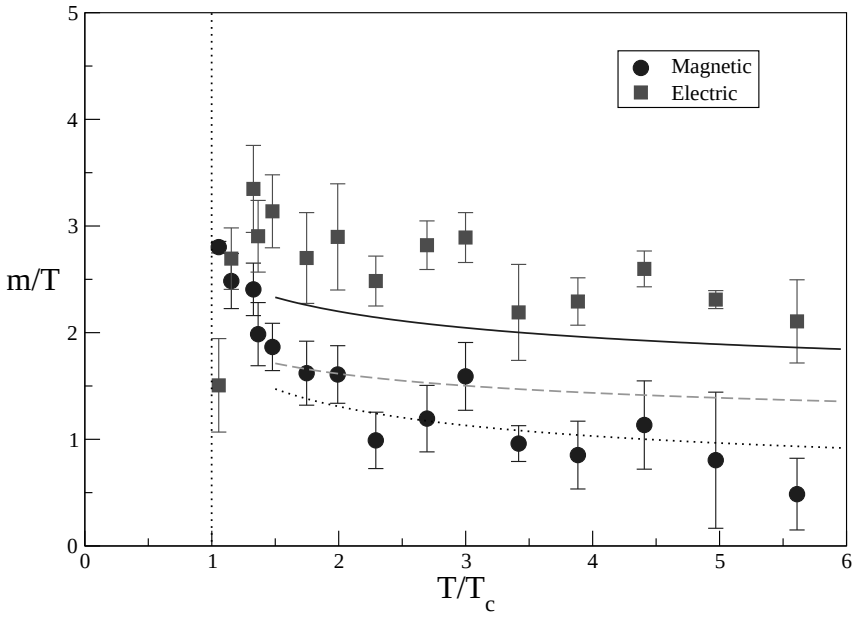

Figure 1.4: Temperature dependence of electric and magnetic screening masses according to Nakamura et al (from hep-lat/0311024). The dotted line is fitted by the assumption, $m_g \sim g^2 T$. For the electric mass, the dashed and solid lines represent LOP(leading-order perturbation) and HTL(hard-thermal loop) resummation results, respectively.

temperature somewhere in the region of

$$T_{E=M} \approx (1.2 - 1.5) T_c = 250 - 300\, MeV \tag{1.9}$$

.

High-T monopoles

The total pressure related to the magnetic (3d) sector of the theory and especially the spatial string tension are other observable related to MQPs above T_c: for a short recent summary see [39]. Two important points made by Korthals-Altes are: (i) MQPs must be in the *adjoint* color representation, to explain data on k-strings and magnetic pressure; (ii) there seems to be a nontrivial small "diluteness" parameter of the MQPs ensemble

$$\delta = \frac{\sigma_1}{M_M^2} \approx \frac{(N-1) n_M}{M_M^3} \approx \frac{1}{20} \tag{1.10}$$

The fact that screening takes place at distances *smaller* than the average inter-MQP one is a clear indication that screening is not a Debye-type weak coupling one, but rather the opposite *strongly* coupled (correlated) screening[6].

Dyons

A very special sector of MQPs are particles with both charges. Because they produce parallel electric and magnetic fields, they have nonzero ($\boldsymbol{EB}$) and thus the topological charge. In fact, as shown by Kraan et al [40], finite-T instantons can be viewed as being made of N_c self-dual dyons: for a very nice AdS/CFT "brane-based" construction leading to the same conclusion, see [41].

Topology is in turn associated with the Dirac zero eigenvalues for fermions, which can be located and counted on the lattice quite accurately. Furthermore, a "visualization" of dyons inside lattice gauge field configurations (using variable non-trivial holonomy) has been developed into a very sensitive tool [42], revealing multi-dyon configurations and their dynamics. One can verify that they make a rather dilute but highly correlated systems: in fact closed chains of up to 6 dyons of alternating charges have been seen. The self-dual dyon density and other properties, as well as their relation to instantons and confinement are summarized in a recent paper [43]. It is enough to mention only that self-dual dyons, like instantons, are electrically screened [3][44] and thus rapidly disappear into the QGP at $T > T_c$. Around T_c their density can thus be related to the instanton density

$$n_{dyon} \sim N_c n_{instantons}/T \sim 3 fm^{-3} \tag{1.11}$$

and the mass to the instanton action

$$M_{dyon} = T * S_{instanton}/N_c \sim (3-4)T \tag{1.12}$$

Both are of the order of the density (and the mass) of the electric (gluon and quark) quasiparticles at $1.5T_c$, confirming a suggested E-M equilibrium in this region.

[6] If a reader may have doubts that a correlated screening may produce such a result, here is an example from the physics of the QCD instantons. The typical inter-instanton distance $n^{-1/4} \sim 1\, fm$ is 5 times *larger* than the screening length of the topological charge $R_{top} = 1/M(\eta') = .2\, fm$: the corresponding ratio for monopoles seem to be around $\delta^{-1/3} \sim 3$. In both cases we don't know how exactly the opposite charges are correlated: pairs or chains are two obvious possibilities.

1.2.3 Higgs phenomenon in QGP?

In this subsection we would like to comment, in a brief form, on a number of questions which are invariably asked in connection with Higgs phenomenon and monopoles at $T > T_c$.

Naively, there is no simple and direct way to apply the lessons from supersymmetric theories such as $\mathcal{N}$=2 Seiberg-Witten theory to QCD-like setting. The former has scalar fields and flat "moduli space" of possible vacua, while the latter has neither scalars nor supersymmetry to keep the moduli space flat.

At finite T the role of Higgs field is delegated to temporal component A_0 of the gauge field: and in fact in gluodynamics there is a spontaneous breaking of the $Z(N_c)$ symmetry at $T > T_c$ because the corresponding effective action $S_{eff}(< A_0 >)$ has N_c discrete degenerate minima[7].

Furthermore, the corresponding effective action gets small near T_c and large fluctuations in "Higgs VEV" $< A_0 >$ are seen in lattice configurations; so one may think first about a generic case in which it is some (color matrix valued) constant in each configuration, to be averaged with appropriate weight $exp[-S_{eff}(< A_0 >)]$ later. Thus one may think about an explicit adjoint Higgs breaking of the color group, parameterized by $N_c - 1$ real VEVs (e.g. for $SU(3)$ $Tr < A_0\lambda^a >$with Gell-Mann diagonal matrices a=3,8). Such breaking makes all gluons massive, except the remaining unbroken $N_c - 1$ U(1)'s which remain massless. These remaining U(1)'s are the Abelian gauge fields which define magnetic charges of the monopoles and their long-range interactions (and electric ones, in the case of dyons).

Finally, the last comment about one lesson from SUSY theories which we don't think can be transferred into the QCD world: these are the enforced properties of monopoles (and many other topological objects like branes) which happen to be "BPS states" with their Coulomb interactions being exactly cancelled by massless scalar exchanges. As a result, such objects can often "levitate" in SUSY settings.[8] In QCD we however do not see or need massless scalars, leaving the usual Coulomb and Lorentz forces dominant at large distances.

1.2.4 Electric-Magnetic Duality and Running Couplings

Let us begin with comments on some theoretical issues related with situations in which both "electric" and "magnetic" particles are present at the same time. For pure gauge fields electric/magnetic duality simply means rewriting

[7]Fermions will lift this degeneracy, as is well known.

[8]In non-SUSY theories BPS states in general can have finite mass, but at low velocities interact weakly with each other.

magnetic field B as gradient and electric field E as a curl of a "dual" potential: however there are nontrivial questions about the sources (and boundary conditions). The electric objects – quarks – are traditionally present in the Lagrangian as Noether charges, while monopoles are solitonic solutions carrying topological charges. Can "magnetic" formulation be consistently defined, interchanging their roles and putting monopoles in the Lagrangian instead? Can even a situation be found in which both formulations are similar? These ideas were discussed starting from the paper [45].

Since *both description should describe the same theory* serious issues of consistency appear. At the quantum mechanics level the famous Dirac condition must be held, demanding that while one of them may be small, the other must necessarily be large. At the level of quantum field theory the Dirac condition elevates into a requirement that two couplings must run in the *opposite directions*

$$\tilde{\beta}(\alpha)_E + \tilde{\beta}(\alpha)_M = 0 \tag{1.13}$$

where the beta functions are $\tilde{\beta}(\alpha) \equiv \frac{\mu}{\alpha}\frac{d\alpha}{d\mu} = 2\beta(g)/g$ for the electric and magnetic couplings respectively, with $\beta(g) \equiv \mu\frac{dg}{d\mu}$ being the usual beta function. This indeed is what happens in Seiberg-Witten solution, in which electric coupling is weak at large momenta due to asymptotic freedom, and magnetic is weak at small ones due to U(1) "Landau pole".

As it is known for 30 years, QGP at very *high* T can be described perturbatively, with e.g. small quark and gluon effective masses $M/T \sim \sqrt{\alpha_{electric}} << 1$. The monopoles in this case are heavy composites which play a minor role, although they are strongly interacting and form an interesting sub-sector in which perturbative analysis is impossible. However as T goes down and one approaches the deconfinement transition $T \to T_c$, the inverse is expected to happen: electrically charged particles – quarks and gluons – are getting heavier and more strongly coupled. There is strong evidence that both phenomena do happen: lattice data show that quark (baryon) masses seem to be large in sQGP near T_c[46], while RHIC's "perfect liquid" supports the idea of strong coupling.

However at this point one may ask what happens with monopoles: as $T \to T_c$ the same logic suggests that they must become lighter and more important. At some point their masses (and roles) get comparable to that of the electric objects, after which the tables are turned and their fortune reversed. Electric objects gets strongly coupled and complicated while monopoles gets lighter, proliferate and eventually take over the bulk, expelling electric fields into the flux tube. As shown in [47], this may happen in the plasma phase, before confinement transition is reached. Following these thoughts, here are two questions, on which we will be focused in Chapter 4: (i) Is there evidence that

the magnetic coupling does run in the opposite direction? (ii) How small does the magnetic coupling become at $T \to T_c$, and is a perturbative description of magnetic plasma possible? As the reader will see in this Dissertation, we will answer "yes" to the first and "no" to the second question.

(A digression about the most symmetric $\mathcal{N}$=4 SYM theory which is conformal. How do we know that its coupling does not run? One may calculate the first coefficient of the beta function, and will indeed see that the negative gauge contribution is nicely cancelled by fermions and scalars. But there are infinitely many coefficients, and one has to check them all! An elegant way to prove the case is based on another outstanding feature of the $\mathcal{N}$=4 SYM: this theory is (nearly) $self-dual$ under electric-magnetic duality. As we discussed above, the Dirac condition requires the product of electric and magnetic couplings to be constant. But, as shown by Osborn [48], in Higgs case the multiplet of (lowest) magnetic objects of the $\mathcal{N}$=4 SYM theory include 5 scalars, 4 fermions (monopoles plus one gluino zero mode occupied), plus 1 spin-1 particle (3 polarizations), exactly the same set of states as in the original electric multiplet (gluon-gluinoes-Higgses). Thus effective magnetic theory has the *same* Lagrangian as the original electric formulation and the same beta function. That would conflict with requirement that both couplings run in the opposite direction, unless they do not run at all!)

1.3 The Structure of The Dissertation

The rest of this Dissertation is organized as follows.

In Part I, including Chapter 2-5, we present our study of the magnetic component of sQGP. In Chapter 2, single monopole motion in a few physically interesting configurations of electric field will be studied, both classically and quantum mechanically. In Chapter 3, we report the details of our Molecular Dynamics (MD) simulations for a strongly coupled plasma with both electric and magnetic charges and present MD results for the transport properties. Chapter 4 is dedicated to investigating the magnetic component of sQGP by applying our MD results and by analyzing recent lattice data. Chapter 5 shows how the magnetic scenario we proposed can help explain the very nontrivial static $\bar{Q}Q$ potentials at $T \approx T_c$ as measured on the lattice.

In Part II, including Chapter 6-7, we examine the electric component of sQGP. In Chapter 6 we will use the finite T potential model to calculate bound states of quarks and gluons beyond the binary, i.e. baryons, glueballs and polymer chains in sQGP. In Chapter 7 we will use the lattice results of baryonic susceptibilities as a diagnosis to probe the quark, diquark and baryon

contents in sQGP.

Finally we summarize the results and make conclusions in Chapter 8.

Part I

The Magnetic Component of sQGP

Chapter 2

Classical and Quantum Motion of Single Monopole

With the ultimate goal of understanding a many-body system of mixed electric charges and monopoles, I will start with a detailed study of the motion of a single monopole, both classically and quantum mechanically, in the presence of various configurations of electrostatic fields. This will manifest the unique features of monopole motion as driven by the Lorentz-type coupling, which is very important for our later investigation of the full dynamics in the many-body setting.[1]

2.1 Monopole Motion in the Field of One Static Electric Charge

The simplest few-body system with magnetic charge is made of two particles: one has electric charge and the other has magnetic charge. In a more general sense we should consider them as two dyons, both with nonzero electric as well as magnetic charges. This problem has been very well studied for many years in both classical and quantum mechanics, and it has fascinated the physicists with many unusual features. See for example [50][51][52].

In such problems one has both electric and magnetic fields. We have the electric field from an E-charge (at space point $\boldsymbol{r}_e$) to be

$$\boldsymbol{E}(\boldsymbol{r}) = \frac{e}{4\pi} \frac{\boldsymbol{r} - \boldsymbol{r}_e}{|\boldsymbol{r} - \boldsymbol{r}_e|^3} \tag{2.1}$$

[1] The works in the present chapter are based on [49][47].

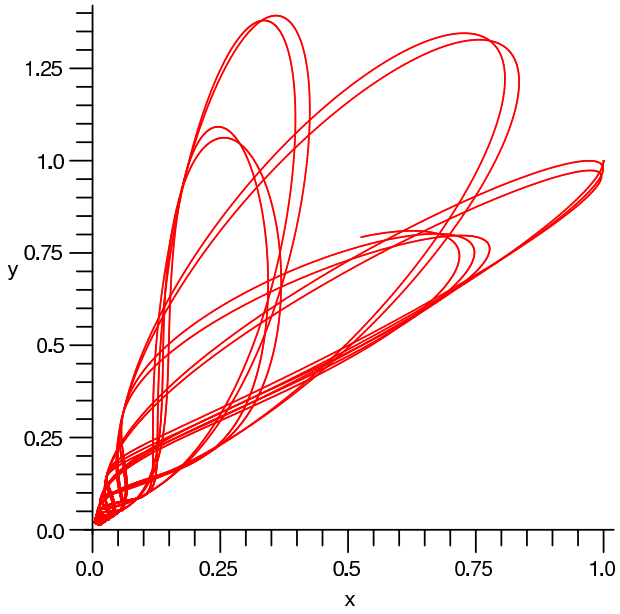

Figure 2.1: The trajectory (projected on x-y plane) of a dyon in the field of an opposite electric charge resting at the origin (in arbitrary unit).

and magnetic field from a M-charge (at space point $\boldsymbol{r}_g$) to be

$$\boldsymbol{B}(\boldsymbol{r}) = \frac{g}{4\pi}\frac{\boldsymbol{r}-\boldsymbol{r}_g}{|\boldsymbol{r}-\boldsymbol{r}_g|^3} \tag{2.2}$$

The interaction between one moving dyon (e_1, g_1) and the other (e_2, g_2) is given by the Coulomb and $O(v/c)$ Lorentz forces

$$\begin{aligned}\boldsymbol{F}_{12} = \quad & \frac{e_2\cdot e_1 + g_2\cdot g_1}{4\pi}\frac{\boldsymbol{r}}{r^3} \\ & + \frac{e_2\cdot g_1 - g_2\cdot e_1}{4\pi}\frac{\boldsymbol{v}_2}{c}\times\frac{\boldsymbol{r}}{r^3} + O(v^2/c^2)\end{aligned} \tag{2.3}$$

with $\boldsymbol{r} = \boldsymbol{r}_2 - \boldsymbol{r}_1$. Here we have used the Lorentz-Heaviside units in which $\boldsymbol{E}$ and $\boldsymbol{B}$ have the same unit and so are the charges e and g.

As early as in 1904, J. J. Thompson found the even two non-moving charges have a nonzero angular momentum $\boldsymbol{J}$ carried by rotating *electromagnetic field (more precisely the Poynting vector)*. Indeed, for an E-charge and a M-charge

(separated by $\boldsymbol{r}$) as sources, it is

$$\boldsymbol{J}_{field} = \int d^3x \boldsymbol{x} \times (\boldsymbol{E} \times \boldsymbol{B})/c = \frac{eg}{4\pi c}\hat{r} \tag{2.4}$$

This angular momentum depends only on the value of charges, independent on how far or close they may be. Its direction is radial, pointing from the E-charge to the M-charge. As a side remark, an alternative way to arrive at the Dirac quantization condition is by requiring any angular momentum (including the above $\boldsymbol{J}$) to be a multiple of half $\hbar$.

Even earlier, in 1896 Poincare observed that the motion of a monopole (and generally a dyon) in an electric charge's Coulomb field is confined on the surface of a cone (thus called the Poincare Cone), as shown in Fig.2.1. Their relative motion (angular rotation and radial bouncing) is always confined inside a cone simply because of the conservation of total angular momentum including the relative rotation and the field's angular momentum (2.4) as well. When getting closer to each other the two particles are forced to relatively rotate faster and faster thus experiencing effective repelling which makes them bouncing radially. Another way to explain the conical motion is to notice that a magnetic charge is making Larmor circles around the electric field; it shrinks near the charge because the field gets stronger there.

Quantum mechanics of such two-dyon system has been worked out in great details since 1970s, especially the many bound states are calculated, see e.g. [50][51] for reviews and further references.

In the following subsection, we analyze one important issue that was not studied before: the induced magnetic current from the moving monopole.

2.1.1 The Induced Magnetic Current from the Monopole Motion

At a distance $\boldsymbol{R}$ from the charge as demonstrated in Fig.2.2, its Coulomb electric field $\boldsymbol{E_R} = \frac{e}{4\pi R^2}\hat{R}$ will stir the magnetic monopole into Larmor motion with radius r_L on the Poincare cone — a small patch of the whole space solid angle. The cone angle is determined by (with v_t the monopole velocity transverse to $\hat{r}$)

$$\cot\theta = \frac{(ge)/4\pi c}{Mv_t r} \tag{2.5}$$

The numerator is precisely the field angular momentum of the charge-monopole pair $L_{EM} = (ge)/4\pi c$, while the denominator is the monopole's kinetic angular momentum $L_v = Mv_t r$ with respect to the origin. The above formula, rewritten as $\cot\theta = L_{EM}/L_v$, reflects the interplay between angular momenta

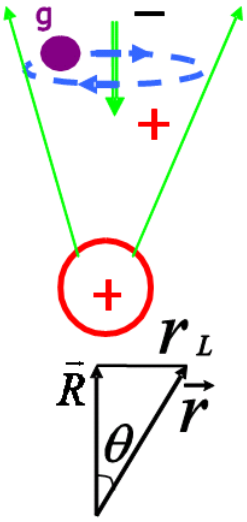

Figure 2.2: Demonstration of the induced magnetic current from monopole motion in the field of an electric charge, see text for details.

of the electromagnetic field and of the particle motion. Though superficially L_v is defined through v_t and r, it is actually a conserved quantity uniquely related to the cone angle θ, see [53] for detailed discussion.

In turn, the monopole forms a loop of magnetic current gL_v/Mr on the cone. Now if we consider many monopoles are running around the static electric charge e, i.e. it is placed within a neutral gas of monopoles with mass M and charge $\pm g$, then the induced magnetic current density will be $J_M = |g|n_L L_v/Mr$ with n_L the monopole density. The direction of the current explains the sign of induced electric dipole[2]. Using dual Maxwell's equation $\bigtriangledown \times \boldsymbol{E} = -\frac{1}{c}\boldsymbol{J}_M$, one finds that such electric dipole is opposite to the usual induced dipoles in dielectric, so in this sense the induced magnetic current from the moving monopole produces an *anti*-screening effect. The charge repels such a dipole: thus the monopoles will fly away from the charge.

To make this statement quantitative, let's calculate the curl of magnetic current around $\boldsymbol{R}$. To do that we need to require that the Larmor circle to be fairly small, for two important reasons: (i) if it is not small then one has to take into account the variation of electric field strength which will warp the circle; (ii) a small Larmor radius enables one to approximate the $\bigtriangledown \times J_M$

[2]Note that although monopoles with $\pm g$ rotate in opposite directions, they produce currents of the same sign, so it is not necessary to distinguish them.

by integrating $\boldsymbol{J}_M$ along the circumference and dividing it by the area of the circle. Small Larmor radius r_L means small angle θ, i.e. $L_v << L_{EM}$. Density of monopoles n_L with angular momentum L_v at R, is related to total monopole density n by $n_L = f_L n$, with f_L some function of R and θ. In such case, the result comes out as:

$$\begin{aligned} \left(\bigtriangledown \times \boldsymbol{J}_M \right)_{\boldsymbol{R}} &= \frac{|g| n_L (L_v/Mr)(2\pi r_L)}{\pi r_L^2} \hat{R} \\ &= \eta \, (c/\lambda_L^2) \, \boldsymbol{E}_{\boldsymbol{R}} \end{aligned} \tag{2.6}$$

Here $\lambda_L = (Mc^2/g^2 n)^{1/2}$ is defined in the same way as the London penetration length (which is usually defined only for superconductor). Interestingly enough one arrives at the second London equation with a modification coefficient

$$\eta = 2 f_L \cos\theta = 2 f_L \, \frac{L_{EM}}{\sqrt{L_{EM}^2 + L_v^2}} \approx 2 f_L \tag{2.7}$$

To end this analysis, we emphasize again its main point: motion of monopoles in the Coulomb field of the electric charge can produce certain anti-screening effect similarly to that in the dual superconductor of condensed monopoles, under the important condition that the field is strong enough, which specifically means that monopoles' bombarding angular momentum L_v is much less than the field angular momentum L_{EM}. The effect discussed here and the well-known Meissner effect of (dual) superconductor share the same mechanism, namely magnetic particles are scattered by the Lorentz force, inducing currents which anti-screen the field. On the other hand, there is a big difference between the two. Meissner effect is only present in superconductors, which expels arbitrarily weak magnetic field. A thermal plasma of monopoles does not have it, and thus distributed weak fields can be present in the bulk. However, strong enough fields can be expelled by the plasma into flux tubes, which are in principle metastable. Solar plasma (for example) has both weak diffusive magnetic fields as well as magnetic flux tubes (visible in telescopes as substructure of the famous solar "dark spots").

2.2 Monopole Motion in the Field of a Static Electric Dipole

A very interesting and important few-body problem is a magnetic monopole moving in the field of a static electric dipole. This is a starting point for

studying a "color"-electric dipole(quark-anti-quark) surrounded by a gas of weakly interacting monopoles which, as we argue, may be very much relevant for understanding confinement. Also as far as we know, this system seems never been studied before.

2.2.1 The Classical Motion

In classical mechanics, we have the EoM for the monopole (of mass M and magnetic charge g) to be the following:

$$M\frac{d^2\boldsymbol{r}}{dt^2} = g\boldsymbol{E}_d \times \frac{d\boldsymbol{r}}{dt} \tag{2.8}$$

with $\boldsymbol{E}_d$ the electrostatic field from the dipole with $\pm e$ charges sitting at $\pm a$ on z axis:

$$\boldsymbol{E}_d = \frac{e}{4\pi}\left[\frac{\boldsymbol{r}-a\hat{z}}{|\boldsymbol{r}-a\hat{z}|^3} - \frac{\boldsymbol{r}+a\hat{z}}{|\boldsymbol{r}+a\hat{z}|^3}\right] \tag{2.9}$$

It will be much convenient to work in the cylinder coordinate (ρ, ϕ, z). By running this EoM numerically with various initial conditions, we can directly obtain real time trajectories of the monopole.

A lot of very complicated and very different motions have been found, sensitively depending on the initial conditions. Roughly one may divide these trajectories into two categories: "trapping" cases (see Fig.2.3) and "escaping" cases (see Fig.2.4). By "trapping" cases we mean the monopole starts with $|\boldsymbol{r}| \sim a$ and after a relatively long time it still remains within distance $\sim a$ from the dipole, while in "escaping" cases the monopole begins moving further and further away from the dipole after a somewhat short time. Due to limited space we show below only few pictures for both cases. Let's just emphasize one particular feature as clearly revealed in Fig.2.3: the monopole is bouncing back and forth between the two electric charges, because of the effective repulsion when it is getting close to the charges (as has been explained in the charge-monopole motion). We have found many such cases which look like two standing charges playing E-M "ping-pong" with the monopole. In a sense the monopole is accurately "guided", or forced, by Lorentz force to collide head-on with the charges: here the Lorentz force provides a mechanism for enhancing the collision rate between particles in a mixture of electric/magnetic particles. This phenomenon as shown here is dual to the famous "magnetic bottle", a device invented for containment of hot electromagnetic plasmas, provided magnetic coils at its ends are substituting the electric dipole and a moving monopole replaced by the electric charge.

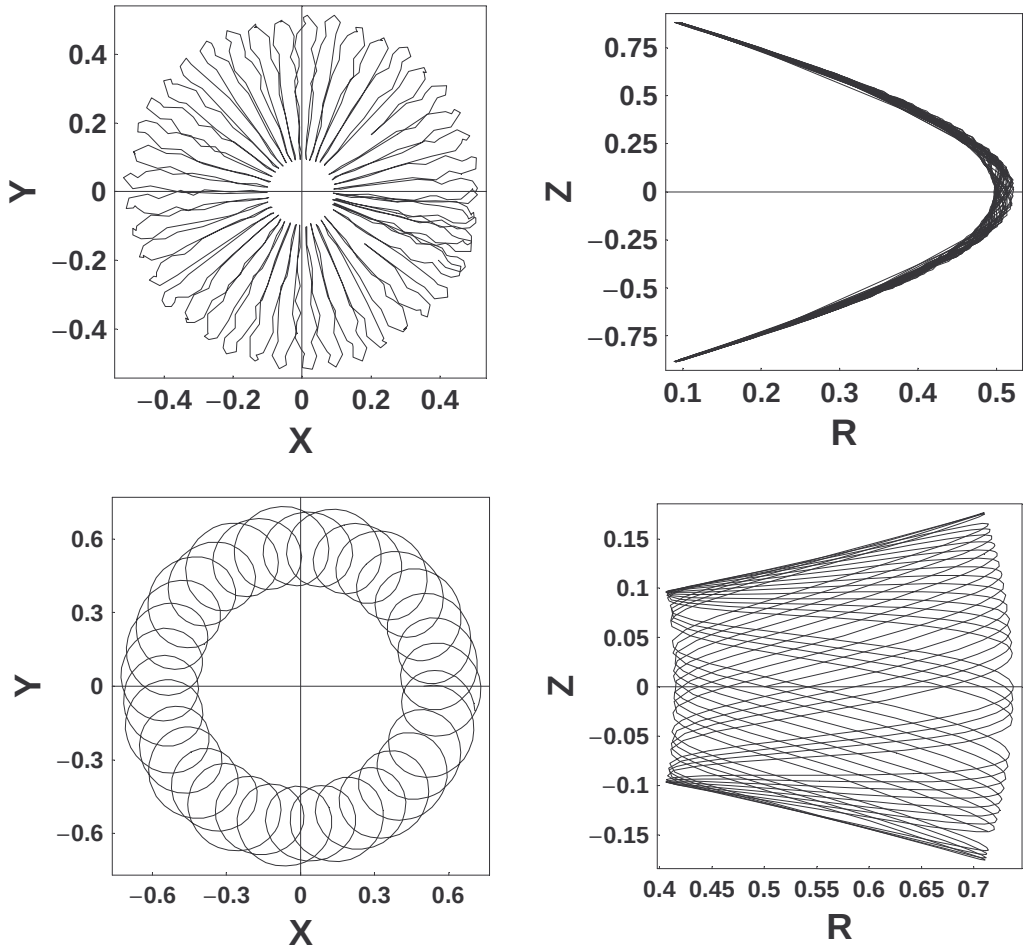

Figure 2.3: Trajectory of monopole motion in a static electric dipole field (with charges at $\pm 1\,\hat{z}$) as (left panel)projected on x-y plane and (right panel)projected on R-z plane ($R = \sqrt{x^2 + y^2}$). The top and bottom parts are for two different initial conditions. All lengths are in unit of a, see text.

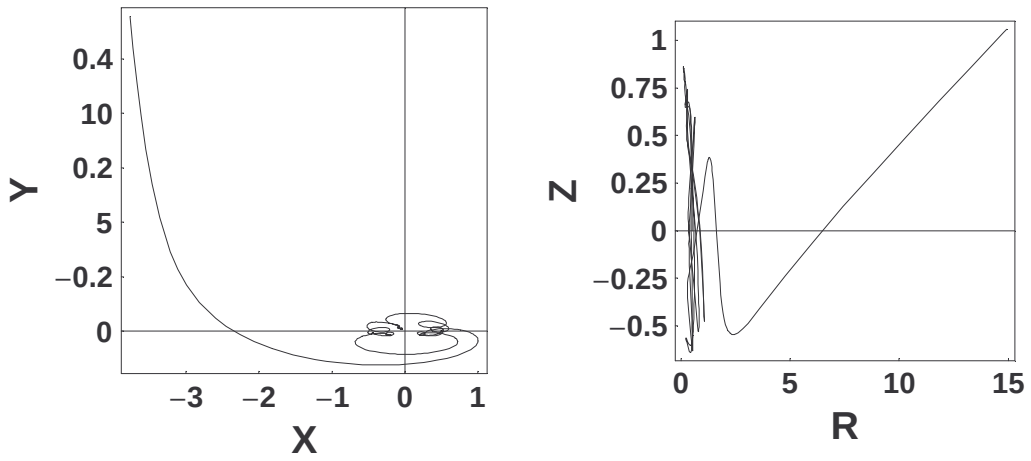

Figure 2.4: Trajectory of monopole motion in a static electric dipole field (with charges at $\pm 1\,\hat{z}$) as (left panel)projected on x-y plane and (right panel)projected on R-z plane ($R = \sqrt{x^2 + y^2}$). All lengths are in unit of a, see text.

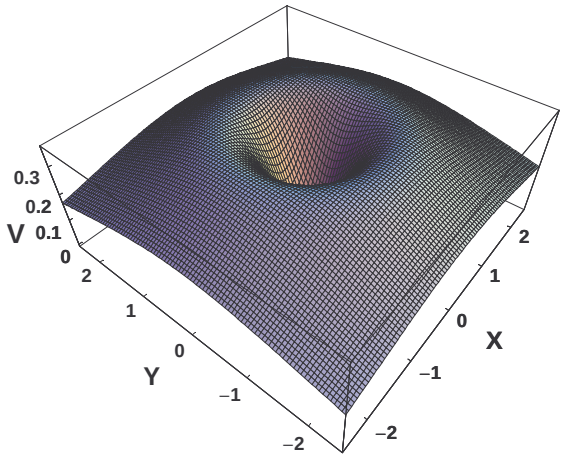

Figure 2.5: (color online) Quantum mechanical effective potential for a monopole in a static electric dipole field. See text for details. Lengths are in unit of a, and potential in $\frac{\hbar^2}{2ma^2}$, see text.

2.2.2 The Quantum Effective Potential

Now let's turn to the quantum mechanics of such system. One can write down the following Hamiltonian for the monopole:

$$\hat{\mathcal{H}} = \frac{(\boldsymbol{p} + g\boldsymbol{A}_e/c)^2}{2M} \tag{2.10}$$

Here $\boldsymbol{A}_e$ is the electric vector potential of the dipole electric field, which can be thought of as a dual to the normal magnetic vector potential of a magnetic dipole made of monopole-anti-monopole. By symmetry argument we can require the vector potential as $\boldsymbol{A}_e = A_e^\phi(\rho, z)\hat{\phi}$ and the monopole wavefunction as $\Psi = \psi(\rho, z)e^{if\phi}$ with f the z-angular-momentum quantum number. Then the stationary Schroedinger equation is simplified to be

$$[\frac{\boldsymbol{p}_\rho^{\,2} + \boldsymbol{p}_z^{\,2}}{2M} + V_{eff}]\psi = E\psi \tag{2.11}$$

$$V_{eff} = \frac{\hbar^2}{2Ma^2}[\frac{1}{\rho/a}(\frac{ge}{\hbar c}\frac{\rho A_e^\phi}{e} + f)]^2 \tag{2.12}$$

To go further one has to specify a gauge (which is equivalent to choosing some particular dual Dirac strings for the charges) so as to explicitly write down A_e^ϕ. We use the gauge which corresponds to the situation with one Dirac string going from the positive charge along positive $\hat{z}$ axis to $+\infty$ and the other going from the negative charge along negative $\hat{z}$ axis to $-\infty$. This gives us:

$$A_e^\phi = -\frac{e}{4\pi\rho}[2 + \frac{z-a}{\sqrt{\rho^2 + (z-a)^2}} - \frac{z+a}{\sqrt{\rho^2 + (z+a)^2}}] \tag{2.13}$$

To give an idea of the effective potential we show Fig.2.5 where $V_{eff}(\rho, z, f) = V_{eff}(\sqrt{x^2+y^2}, z, f)$ is plotted for the x-y plane with $z = 0$ and $f = 0$. From the plot we can see that there must also be quantum resonance states with the monopole bounded around the dipole for a long time before eventually decaying away. Namely one can find states with $E = \hbar\omega + i\Gamma$ with $\Gamma << \hbar\omega$ and count how many there are.

2.3 Monopole Motion in the Field of an Electric Flux Tube

In this section we study the monopole motion in a very special situation, namely its scattering in the field of an electric flux tube. This can be viewed

as an idealized version of the electric dipole in the previous section, in the sense that an electric flux tube is an infinitely separated pair of charges with electric field lines being compressed into a tube structure. The physical motivation is to study possible formation of electric flux tube in the post-confinement regime just above T_c, as we already discussed in the Introduction. To that end, a detailed knowledge of the monopole scattering in the flux tube field and the induced magnetic currents will be essential.

2.3.1 Classical Scattering of Monopole in the Flux tube Field

Let us consider an electric flux tube field in the $\hat{z}$ direction with monopole bombarding into it, as demonstrated in Fig.2.6. The monopole from outside which moves into it will be turned away by Lorentz force and eventually leave the field region. Although its energy remains unchanged, the momentum is changed, which means that there could be an effective pressure acting from the monopole on the tube if one considers there are many monopoles surrounding the flux tube and getting scattered off it. The situation however is simple only if the strength of the field in the tube is such that particles penetrate only very small part of its radius. (One can then further simplify the problem into flat surface, with effective current floating in wall separating field-free and field regions, as is the case for magnetic flux tube in solar plasma.) In such case the induced magnetic current from such scattering will strengthen the original electric field inside the tube according to one of the dual Maxwell's equations $\bigtriangledown \times \boldsymbol{E} = -\frac{1}{c}\boldsymbol{J}_M$, similar to what we analyzed in the Section.2.1. If however, the monopoles can penetrate into the flux tube beyond its center and exit on the far side, they start generating a counter-rotating current which eventually may destroy the flux tube field. To further shed light on this point, more careful analysis of the induced current during scattering of these bombarding monopoles will help.

The lower panel of Fig.2.6 (transverse projection of the upper) shows a few trajectories (with different ending points A, B, B', C, C') in the constant field E region (within tube radius R), starting from the same initial point I (at the bottom) with same velocity v (thus curled with same Larmor radius $r_L = Mvc/gE$), yet with different impact parameter b as they are aiming at different angles. The impact parameter is related to the monopole's incoming angular momentum by $L_v = \pm Mvb$ depending on whether the velocity orients toward left or right at the initial point (noting the positive $\hat{z}$ is pointing into the page in the figure). For example, the red curve($I \rightarrow A$) is for $b = 0$ and $L_v = 0$, the blue solid/dashed curves is for certain nonzero b and same

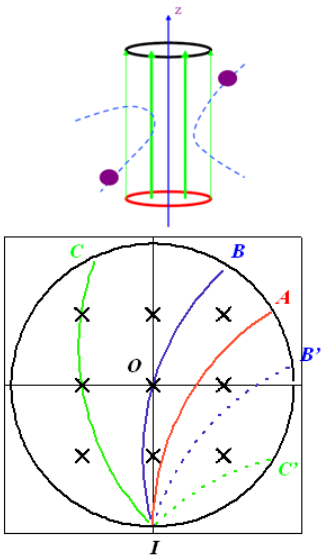

Figure 2.6: Demonstration of the induced magnetic current from monopole motion in the field of an electric flux tube, see text for details.

$|L - v|$ yet opposite signs (with $I \to B$ positive and $I \to B'$ negative), and the green solid/dashed curves for even larger b and $|L_v|$ (with $I \to C$ positive and $I \to C'$ negative).

We now consider the currents J_b produced by various trajectories. In particular let's examine how the combined current j_b of two trajectories with same b and $\pm|L_v|$ changes with b. The important observation is the following: trajectories with *small b or small* $|L_v|$, like $I \to A$, contribute *counterclockwise currents*, while trajectories with *large b or large* $|L_v|$, like $I \to C, C'$, contribute *clockwise currents*, and there is a *critical b or* $|L_v|$ (which is precisely the solid blue curve $I \to B$ going right through the center of tube) beyond which the current inversion happens. Some simple algebra leads to the following *critical angular momentum of the current inversion*:

$$|L_c| = Mvb = \frac{g\Phi_E}{2\pi c} \tag{2.14}$$

with $\Phi_E = E\pi R^2$ the electric flux. By interpreting the right-hand-side as the electric-magnetic field angular momentum in this cylindrical setting, we simply have critical momentum $|L_c| = L_{EM}$ which coincides with the analysis in the previous example. Very importantly, strong electric field means large

$|L_c|$ and stable flux tube, while weak field (with small $|L_c|$) prefers becoming diffusive in the bulk rather than being expelled into flux tube.

Such current inversion phenomenon is very important. The counterclockwise currents (from small L_v) strengthen the original field[3], while the clockwise currents (from large L_v) weaken them. Thus the current inversion is like a "para/dia-electric" inversion, in macroscopic language, and it kills the flux tubes.

To summarize the lesson from this classical example, the value of the angular momentum plays essential role in the monopole scattering by the flux tube. If particles have typical momentum $\bar{p}$ and the radius of the tube is R the angular momentum is $\bar{L} \sim \bar{p}R$. When $\bar{L}$ is small or equivalently the electric field is strong, the motion is still basically radial and the pressure argument works. In the opposite limit of large $\bar{L} \sim \bar{p}R >> L_{EM}$ or weak field, the induced currents have both signs and cancel each other, and there is no reason for flux tube to exist. Thus there must be some *critical* value of $\bar{p}R$ above which there is no flux tube solution, depending on exact magnitude of currents induced in channels with different angular momentum, to be evaluated quantum mechanically below. Analysis and detailed calculation along this line will be continued in Chapter 5.

2.3.2 Quantum Scattering of Monopole in the Flux tube Field

In this subsection we solve exactly the quantum scattering of monopole in the flux tube field. The electric field, with flux Φ_E and size R, is described in cylindrical coordinate (r, ϕ, z) by the following:

$$\boldsymbol{E} = \begin{cases} E_I \hat{z} = \Phi_E/(\pi R^2)\ \hat{z} & , \quad r \leq R \\ 0 & , \quad r > R \end{cases} \tag{2.15}$$

The corresponding dual vector potential reads:

$$\boldsymbol{C} = C_\phi\, \hat{\phi} = \begin{cases} \frac{\Phi_E}{2\pi R}\, \frac{r}{R}\ \hat{\phi} & , \quad r \leq R \\ \frac{\Phi_E}{2\pi R}\, \frac{R}{r}\ \hat{\phi} & , \quad r > R \end{cases} \tag{2.16}$$

The string tension is given by

$$\sigma = \Phi_E^2/(2\pi R^2) \tag{2.17}$$

[3]Note that in the (dual) superconductor case [54], the Abrikosov vortex is exactly supported by supercurrent of scattered condensate in lowest possible angular momentum, namely $L_v = 0$ channel.

According to Dirac quantization, the flux can be normalized via $(g\Phi_E)/(4\pi\hbar c) = d/2$. While the results obtained below can be used for general d, we are particularly interested in the $d = 2$ case.[4]

A monopole with mass M moving in such a field is governed by the following Hamiltonian: in the non-relativistic case

$$\mathcal{H}_{NR} = (\boldsymbol{p} + \frac{g}{c}\boldsymbol{C})^2/(2M) \tag{2.18}$$

while in relativistic case it is

$$\mathcal{H}_R = \sqrt{\left(\boldsymbol{p} + \frac{g}{c}\boldsymbol{C}\right)^2 c^2 + M^2\, c^4} \tag{2.19}$$

The conserved quantities are
1) total energy ϵ;
2) longitudinal momentum p_z;
3) hence one can use longitudinal energy $\epsilon_z = p_z^2/2M$ and transverse energy $\epsilon_t = \epsilon - \epsilon_z$ to be conserved separately;
4) the angular momentum $L_z = r\,(p_\phi + \frac{g}{c}C_\phi)$.
The conservation of both ϵ_t and L_z implies that the monopole is rejected back (unless $L_z = 0$) when it approaches the center of the tube, due to generic centrifugal barrier $\sim L_z^2/(2Mr^2)$ which dominates at small r.

Quantum mechanical motion of single monopole is described by wave function Ψ which is a scattering solution to $\mathcal{H}\Psi = \epsilon\Psi$ with $\mathcal{H}$ from eq.(2.18). Making use of conserved quantities, we may decompose the wave function into $\Psi = f(r)e^{im\phi}e^{iK_z z}$, with energy[5] $\epsilon = \epsilon_z + \epsilon_t = (\hbar K_z)^2/2M + (\hbar k)^2/2M$ and angular momentum $L_z = m\hbar$. Let's first introduce several parameters involved later in the solution, including:

$$\nu = m + d \tag{2.20}$$
$$\gamma = 1 + |m| \tag{2.21}$$
$$\alpha = (kR)^2/(4d) - m/2 \tag{2.22}$$

We repeat that $d = (g\Phi_E)/(2\pi\hbar c)$ tells how much flux is going through the tube. The meaning of ν can be explained as follows: it is quantized (integer-valued) form of a relation between velocity, canonical momentum and dual field

[4]There are strong evidences from lattice study of high-T magnetic QCD which supports the idea that monopoles in QGP have such charges that $d = 2$ and their total numbers scale as $N_c^2 - 1$, see e.g.[39]

[5]Here we first deal with non-relativistic case, while later the treatment will be generalized to relativistic case which turns out to be rather straightforward.

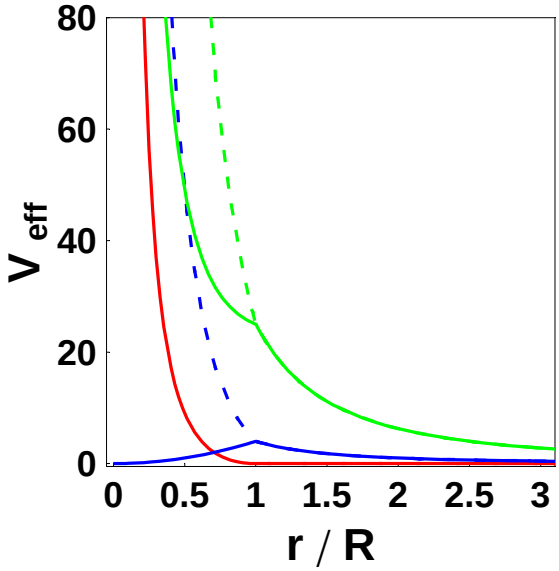

Figure 2.7: The effective potential V_{eff} as a function of r/R for $\nu = 0$(red), $\nu = \pm 2$(blue solid/dashing), and $\nu = \pm 5$(green solid/dashing).

$M\boldsymbol{v} = \boldsymbol{p} + g\boldsymbol{C}$ projected (via their cross-product to $\boldsymbol{r}$) to angular momenta. Classical path $I \to A$ in Fig.2.6 which has velocity at large distances directed toward the tube center corresponds to $\nu = 0$. The $m = 0$ channel is the one corresponding to $I \to B$ path: it goes through the center because it experiences no centrifugal barrier $\sim m^2/r^2$. As we will see below, this correspondence will explain the signs of the currents, generated in each partial waves.

The Schrodinger equation can then be reduced to the following cylindrical radial equation

$$\frac{1}{r}\frac{d}{dr}\left(r\frac{d\,f}{dr}\right) + \left[k^2 - V_{eff}\right] f_{k,\nu} = 0 \tag{2.23}$$

The effective potential takes the form:

$$V_{eff} = \frac{1}{r^2} \times \begin{cases} \left[\nu + d\cdot(r^2/R^2 - 1)\right]^2 & , \quad r \le R \\ \nu^2 & , \quad r > R \end{cases} \tag{2.24}$$

Examples of V_{eff} for several ν values are shown in Fig.2.7.

The equation could be exactly solved both inside and outside the tube, as shown separately below:
i) $r \le R$ (inside), the solution is given by confluent hypergeometric function

${}_1F_1[x]$:

$$f^{(i)}_{k,\nu} = A_{k,\nu}\; e^{-\frac{dr^2}{2R^2}} \left(\frac{dr^2}{R^2}\right)^{\frac{\gamma-1}{2}} {}_1F_1\left[\gamma/2-\alpha,\gamma,\frac{dr^2}{R^2}\right] \tag{2.25}$$

ii) $r > R$ (outside), the solution is expressed by two Hankel functions $H^{(1,2)}_\nu[x]$ with proper phase shift $\delta_{k,\nu}$:

$$f^{(ii)}_{k,\nu} = \frac{B_{k,\nu}}{2}\left[H^{(2)}_\nu[kr] + e^{i2\delta_{k,\nu}} H^{(1)}_\nu[kr]\right] \tag{2.26}$$

Finally the two functions should be connected smoothly at $r = R$, which determines:
the normalization constants A, B satisfying (with $J_\nu[x], Y_\nu[x]$ Bessel functions)

$$\begin{aligned} \mathcal{R}_{AB} &= \frac{A_{k,\nu}}{B_{k,\nu}} \\ &= e^{i\delta_{k,\nu}} \frac{(\cos\delta_{k,\nu})J_\nu[kR] - (\sin\delta_{k,\nu})Y_\nu[kR]}{e^{-d/2}\, d^{(\gamma-1)/2}\, {}_1F_1[\gamma/2-\alpha,\gamma,d]} \end{aligned} \tag{2.27}$$

and the phase shift $\delta_{k,m}$ being

$$\begin{aligned} \delta_{k,\nu} &= \arctan\left[\frac{J_{\nu+1}[kR] - GJ_\nu[kR]}{Y_{\nu+1}[kR] - GY_\nu[kR]}\right] \\ G &= \left[\nu - (\gamma-1-d) - (1-2\alpha/\gamma)\cdot d\cdot \tilde{F}\right] \Big/ (kR) \\ \tilde{F} &= {}_1F_1[\gamma/2-\alpha+1,\gamma+1,d] \Big/ {}_1F_1[\gamma/2-\alpha,\gamma,d] \end{aligned} \tag{2.28}$$

However exceptions to eq.(2.27,2.28) can occur when it so happens that ${}_1F_1[\gamma/2-\alpha,\gamma,d] = 0$. In such situation the alternative equations are the following:

$$\begin{aligned} \mathcal{R}_{AB} &= \frac{A_{k,\nu}}{B_{k,\nu}} \\ &= \frac{e^{i\delta_{k,\nu}}\,(kR)\,[(\cos\delta_{k,\nu})J_{\nu+1}[kR] - (\sin\delta_{k,\nu})Y_{\nu+1}[kR]]}{e^{-d/2}\, d^{(\gamma+1)/2}\,(2\alpha/\gamma-1)\,{}_1F_1[\gamma/2-\alpha+1,\gamma+1,d]} \end{aligned} \tag{2.29}$$

$$\delta_{k,\nu} = \arctan\left[\frac{J_\nu[kR]}{Y_\nu[kR]}\right] \tag{2.30}$$

The coefficient $B_{k,\nu}$ should be determined by calculating the current at

$r \to \infty$ and matching the physical boundary current. To this point, our problem of finding quantum mechanic solutions (with arbitrary k, ν) for monopole scattering off flux tube have been all set. With these analytical solutions at hand, a few discussions are in order below.

Scattering Amplitude

Now we discuss the boundary condition and determine the scattering amplitude. As a scattering problem, we expect an incident current described by transverse plane wave, say e^{ikx}, in the cylindrical setup. Thus we write down the asymptotic wave function as[6]

$$\Psi_k(r \to \infty) = e^{ikx} + \left[\sum_\nu \mathcal{F}_{k,\nu}(\phi)\right] \frac{e^{ikr}}{\sqrt{r}} \tag{2.31}$$

Expanding $e^{ikx} = e^{ikr\cos\phi}$ also in terms of $e^{im\phi}$ and comparing the above to the large r limit of $f^{(ii)}_{k,\nu}(r)$ from eq.(2.26), we obtain the normalization constant B as

$$B_{k,\nu} = e^{i\pi(\nu/2-d)} \tag{2.32}$$

with the feature $|B_{k,\nu}|^2 = 1$ independent of k, ν values[7].

The partial-wave scattering amplitude is determined via phase shift as

$$\mathcal{F}_{k,\nu}(\phi) = \frac{e^{-i\pi/4}}{\sqrt{2\pi k}} \left[e^{i(2\delta_{k,\nu} - d\pi)} - 1\right] e^{im\phi} \tag{2.33}$$

This gives the partial-wave scattering cross section, or more precisely transverse cross "length", as

$$S_{k,\nu} = \frac{4}{k} \sin^2(\delta_{k,\nu} - d\pi/2) \tag{2.34}$$

The total cross section is a sum of the above over all ν.

Examples of $\delta_{k,\nu}$ and $S_{k,\nu}$ as functions of k for several values of ν are plotted in Fig.2.8.

[6]Here we temporarily normalize the incoming current as just $v = \hbar k/M$ while in later section additional factor from density n will be included.

[7]One should keep open mind in that different boundary conditions lead to different weights $B_{k,\nu}$ among partial waves. It is not clear if there could be choices other than the ones used here which can best describe the thermal monopole scattering by flux tube field. An extreme example is superconductor which picks only $B_{k,0}$ with all others vanishing.

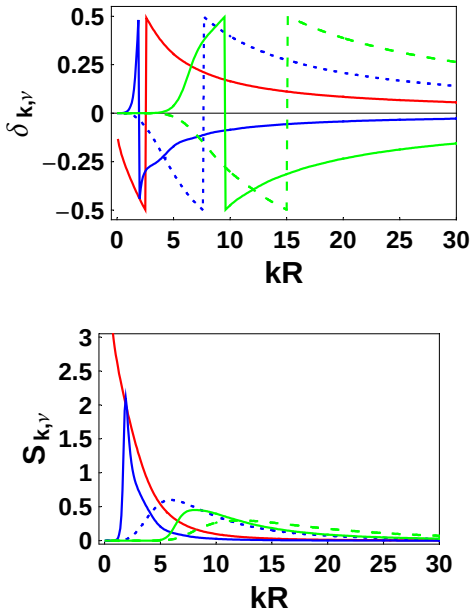

Figure 2.8: (upper) Scattering phase shift $\delta_{k,\nu}$ and (lower) scattering cross section $S_{k,\nu}$ as a function of kR for $\nu = 0$(red), $\nu = \pm 2$(blue solid/dashing), and $\nu = \pm 5$(green solid/dashing).

Before closing this subsection,we'd like to point out that the phase of coefficient given in (2.32) is related to the choice of e^{ikx} as asymptotic incident state (while its unity amplitude is general). Physically an incident particle can come in from any direction besides $\hat{x}$ axis, with equal probability, so an average over all possible orientation of initial $\boldsymbol{k}$ is called for. This can be achieved by first doing calculation using (2.32) and averaging over the ϕ dependence at the end, and the effect of this procedure is simply the entire suppression of interference terms among different partial waves.

Magnetic Current

The magnetic current generated by single monopole during scattering process can be calculated by

$$\boldsymbol{j}_M = \frac{ig\hbar}{2M}\left[(\bigtriangledown\Psi^*)\Psi - (\bigtriangledown\Psi)\Psi^*\right] + \frac{g^2}{Mc}(\Psi^*\Psi)\boldsymbol{C} \tag{2.35}$$

The nontrivial part is the $\hat{\phi}$ component: [8]

$$J_M^\phi(k|r) = \sum_{\nu=-\infty}^{\infty} j_M^\phi(k,\nu|r) \tag{2.36}$$
$$= \frac{g\hbar}{Mr}\sum_{\nu=-\infty}^{\infty}\left[\nu - d\cdot(1-\frac{r^2}{R^2})\cdot\theta[1-\frac{r}{R}]\right]|f_{k,\nu}|^2$$

with $\theta[x]$ the unit step function: $\theta[x]=1$ for $x>0$ and vanishes otherwise. We may further combine $\pm|\nu|$ terms and rewrite it as

$$J_M^\phi(k|r) = \frac{g\hbar}{Mr}\sum_{\nu=0}^{\infty}\tilde{j}_M^\phi(k,\nu|r) \tag{2.37}$$
$$\tilde{j}_M^\phi(k,0|r) = -d\cdot(1-\frac{r^2}{R^2})\cdot\theta[1-\frac{r}{R}]\,|f_{k,0}|^2$$
$$\tilde{j}_M^\phi(k,\nu|r) = \nu\cdot\left[|f_{k,\nu}|^2-|f_{k,-\nu}|^2\right]$$
$$-d\cdot(1-\frac{r^2}{R^2})\cdot\theta[1-\frac{r}{R}]\cdot\left[|f_{k,\nu}|^2+|f_{k,-\nu}|^2\right]$$

This expression implies two important points: first, significant contribution to magnetic current comes from small r part as is evident from $1/r$ dependence, so partial waves with large amplitude at small r (namely small $|\nu|$ channels) are important; second, according to $j_M^\phi \propto \nu$ at $r>R$, partial waves with m symmetric to d, namely a pair of $\pm|\nu|$ channels, tend to produce opposite currents which substantially cancel each other. It is worth emphasizing that only $\nu=0$ partial wave (the one picked by the whole condensate in ANO vertex case, see e.g. [54]) will benefit from the first point and at the same time NOT suffer from the second point.

Clearly for each given k the total current $J_M^\phi(r)$ should be built up from summing currents of all partial waves , namely summing $j_M^\phi(k,\nu|r)$ over quantum numbers ν. One is naturally concerned with the convergence of such infinite summation, which is basically determined by the large $|\nu|$ behavior. We can expect that large $|\nu|$ partial waves contribute very little to the total current, which bears two simple physical arguments: from energy point of view, states with $|\nu|$ experience centrifugal potential $V(r)\sim\hbar^2|\nu|^2/2Mr^2$ while the kinetic energy being $E_k=\hbar^2k^2/2M$, so if $kR<|\nu|$ then $E_k<V(r=R)$ which means it is very hard for the particle to "climb" up the potential barrier all the way into the tube; from the impact parameter perspective, states with $|\nu|$ and

[8] $\hat{r}$ component is zero and $\hat{z}$ component is totally irrelevant and can also be set to zero by replacing $e^{iK_z z}$ with real $\sin,\cos$ functions.

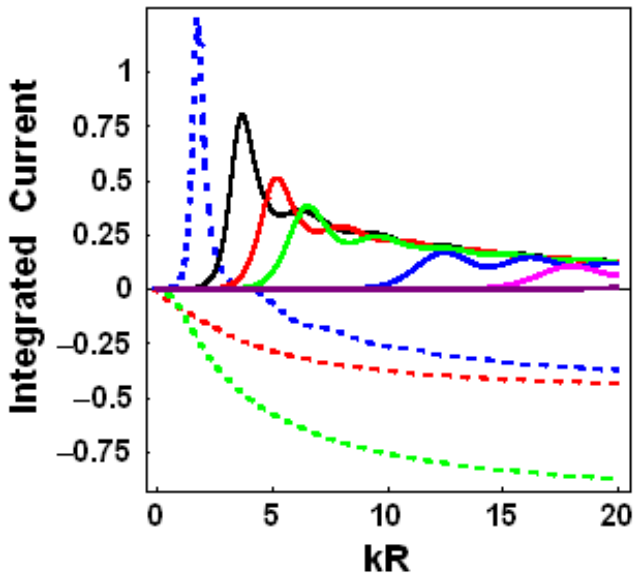

Figure 2.9: Integrated current $\mathcal{I}_\nu$ as a function of kR for different values of ν: dashed lines are for $\nu = 0$(red), $\nu = 1$(green), $\nu = 2$(blue), while solid lines are for $\nu = 3$(black), $\nu = 4$(red), $\nu = 5$(green), $\nu = 10$(blue), $\nu = 20$(magenta), and $\nu = 30$(purple).

k have semiclassical impact parameter $b \sim |\nu|/k$, so if $kR < |\nu|$ then $b > R$ which means the incident particle will be largely missing the central part and thus very little scattered, leading to negligible induced currents. This conclusion has been confirmed by extensive numerical calculation and practically for given kR all partial waves with $\nu \geq 1.5kR$ are vanishingly small, as is evident from Fig.2.9 to be explained in next subsection.

The Total Current

Now we perform the radial integration of the current J_M^ϕ over r which will be needed in Chapter 5:

$$\int_0^R J_M^\phi dr = \frac{g\hbar}{M}\mathcal{I}(kR) = \frac{g\hbar}{M}\sum_{\nu=0}^{\infty}\mathcal{I}_\nu(kR) \tag{2.38}$$

$$\mathcal{I}_\nu(kR) = \int_0^R dr\, \tilde{j}_M^\phi(k,\nu|r)/r$$

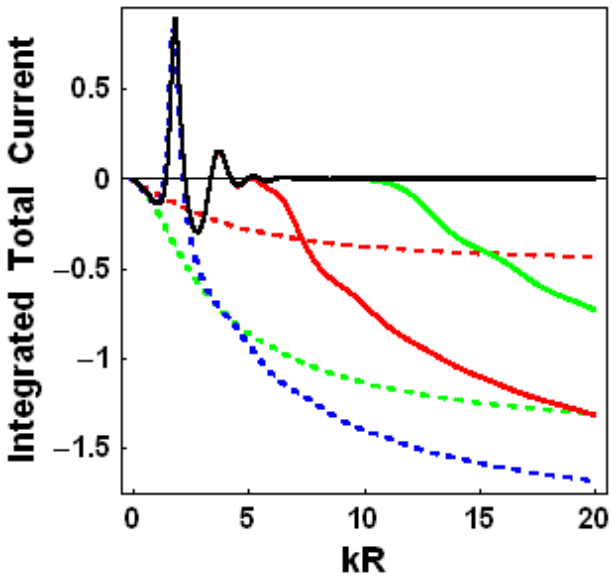

Figure 2.10: Integrated total current $\mathcal{I}$ as a function of kR for different values of summation cut ν_{cut}: dashed lines are for $\nu_{cut} = 0$(red), $\nu_{cut} = 1$(green), $\nu_{cut} = 2$(blue), while solid lines are for $\nu_{cut} = 5$(red), $\nu_{cut} = 10$(green), $\nu_{cut} = 20$(blue), and $\nu_{cut} = 30$(black).

In Fig.2.9 we plot $\mathcal{I}_\nu$ versus kR for various ν. The interesting observation is that the integrated current is negative for $\nu < 2$, positive for $\nu > 2$, while for $\nu = 2$ partially positive (at small kR) and negative (at large kR). This result from quantum mechanics perfectly agrees with our conclusion from classical treatment in the Introduction part, not only qualitatively but even quantitatively: the critical angular momentum for current inversion observed here $L_c = \nu_c\hbar$ with $\nu_c = 2$ coincides with that predicted by eq.(2.14) once our flux $g\Phi_E = d\,2\pi\hbar c$ with $d = 2$ is plugged in.

Now we perform the final step: namely summing $\mathcal{I}_\nu$ over ν to obtain the integrated total current $\mathcal{I}$. This is done numerically, with summation cut $\nu \leq \nu_{cut}$ applied, see Fig.2.10 for results for various ν_{cut}. As can be seen, for the displayed regime $kR \leq 20$ the summation is converged enough as soon as $\nu_{cut} \geq 20$, as the curves with $\nu_{cut} = 20$ and $\nu_{cut} = 30$ coincide on top of each other and are hardly distinguishable. It is this numerically evaluated function $\mathcal{I}(kR)$(with our highest cut $\nu_{cut} = 30$) that will be used in subsequent sections.

The behavior of this function $\mathcal{I}(kR)$ has rather nontrivial wiggle structure: the general trend is oscillatory, with a modest negative part at small $kR < 1.42$ (basically from negative contribution from $\nu = 0, 1$) followed by a rather high

positive peak (dominantly from $\nu = 2$) between $1.42 \to 2.24$. These first two structures, first negative then positive, basically cover the interesting region of kR(see discussion in next paragraph). Suppose there is a flux tube with certain R, then at low temperature the typical $\bar{k}$ is small and $\bar{k}R$ falls within negative region which supports the flux tube, while at high temperature the larger $\bar{k}$ brings $\bar{k}R$ beyond the negative region into the tremendous positive region which will kill the flux tube. So there is a transition with the border at $kR = 1.42$: beyond this point higher partial waves with $\nu \geq 1.5 \times 1.42 = 2.13$ (which is also close to the classical critical value $\nu_c = 2$) will become dominant. By Comparison of this curve with the red dashed one (only $\nu = 0$), which corresponds to what superconductor can do, one understands why a condensate does much better in confining a flux tube than a normal thermal ensemble can do. The first negative peak, actually the best point[9] for flux tube formation, locates at

$$k_m R = 1.076 \quad with \quad \mathcal{I}(k_m R) = -0.140 \tag{2.39}$$

Partial Wave with $\nu = d$ and Possible Resonance

The effective potential V_{eff} with $\nu = d$ or equivalently $m = 0$ is special in that it vanishes at the center $r = 0$, while for all other $\nu \neq d$ states there will be diverging term $\sim (\nu - d)^2\hbar^2/2Mr^2$. The shape of it (see Fig.2.7) actually indicates possibility for resonance to occur. Whether there could be resonance solution or not depends on the competition of the localization energy and the potential barrier whose peak value is $E_{p.} = d^2\hbar^2/2MR^2$ at $r = R$. To settle this one can look at the condition for the wave function (2.25) to be zero right upon $r = R$ (which is very close to the resonance situation and gives estimate of kinetic energy). This yields the series of particular values of k: $k_0 R = 2.576$, $k_1 R = 5.632$, $k_2 R = 8.729$, $k_3 R = 11.847$, ... Thus clearly to have one resonance level, one needs at least $E_{p.} > \hbar^2 k_0^2/2M$ namely $d > 2.576$. Indeed by fine search for resonance structure in scattering phase shift we identified one resonance in the case of $d = 4$, see Fig.2.11, with $k_{res.} \approx 2.77$ very close to the above k_0 and narrow width $\Gamma_k \sim 0.1/R$. Nothing similar was found in $d = 2$. With large enough d the occurrence of resonance should be a general

[9]One might argue that there will be an even larger negative peak at $kR \approx 2.77$, however to reach that point one requires much larger $\bar{k}$ which usually means broader distribution over k around $\bar{k}$, and that will easily make the total contribution rather small after cancellation with the adjacent large positive peak.

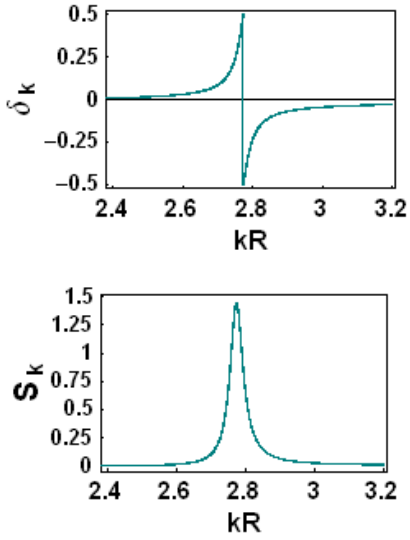

Figure 2.11: (Upper) Phase shift and (lower) scattering cross section as functions of kR for $\nu = d = 4$ which show resonance structure, see text.

phenomenon and the induced current produced by these resonance states actually will spoil the original flux tube field as monopole in such state stays in the center of tube and "pushes" field outward rather than inward: remember the large positive peak in $\mathcal{I}(kR)$ (black curve in Fig.2.10) is precisely due to the contribution from $\nu = d$ partial waves.

Quantum Mechanical Motion of Single Relativistic Monopole

In this subsection we generalize the obtained solutions to relativistic case. Now one has to solve Klein-Gordon equation (since monopoles are scalar particles) instead of Schrodinger equation:

$$\left[\epsilon^2 - M^2\,c^4 - \left(\boldsymbol{p} + \frac{g}{c}\boldsymbol{C}\right)^2 c^2\right]\Psi = 0 \tag{2.40}$$

Fortunately it turns out that by again writing eigenstate of energy ϵ as $\Psi = f_{k,\nu}(r)e^{im\phi}e^{iK_z z}$ one recovers exactly the same radial equation as eq.(2.23) except for changing $k = \sqrt{(2M\epsilon)/\hbar^2 - K_z^2}$ to the following

$$k = \sqrt{(\epsilon^2 - M^2\,c^4)/(\hbar c)^2 - K_z^2} \tag{2.41}$$

So all the exact wave functions obtained in non-relativistic case are still solutions to the Klein-Gordon equation after the above replacement of k in eq.(2.25)(2.26). This change of k should be done for all the relevant formulae above.

Another important change is for the current equation (2.36): due to relativistic effect the mass M should be replaced by ϵ/c^2 , namely

$$j_M^{\phi}(k,\nu|r) = \frac{g\hbar}{(\epsilon/c^2)r}\left[\nu - d\cdot(1-\frac{r^2}{R^2})\cdot\theta[1-\frac{r}{R}]\right]|f_{k,\nu}|^2 \tag{2.42}$$

The same replacement should also be applied to integration over current in eq.(2.38). All other aspects remain pretty much the same as in non-relativistic case and we skip further discussion.

The quantum mechanic results obtained here will be used in Chapter 5 to calculate the stability condition for flux tube formation.

Chapter 3

Molecular Dynamics Study of Strongly Coupled Plasma with Electric and Magnetic Charges

In this chapter, we deal with the many-body system containing dynamically both electric and magnetic charges. In particular we study the transport properties of such a classical system.

Molecular Dynamics (MD) simulations are proved to be powerful tools widely used for studying the conventional EM plasma, especially in the strongly coupled regime when the analytic approaches are difficult. It provides detailed microscopic real time information about correlation functions and transport properties. It has been recently been employed to simulate sQGP in [23][24][49][25]. The classical Coulomb plasma parameter is usually characterized by a key parameter Γ, i.e. the ratio of the potential energy (interaction) to the thermal kinetic energy; thus a weakly coupled plasma has $\Gamma << 1$. Plasmas with $\Gamma > 1$ are known as strongly coupled, and for $\Gamma < few10$ it is in the liquid regime, for $\Gamma > \Gamma_c \sim 100$ it is solid, with less precisely defined "glassy" regime in between.[1]

In the following, we will implement the first (as far as we know) molecular dynamics (MD) simulations for a strongly coupled plasma with *both* electric and magnetic charges. This study, as we already said in the Introduction, is motivated by the magnetic scenario for sQGP. In this chapter we concentrate on the MD setup and the transport properties measured directly from the simulation, while the application of our MD results to sQGP system will be

[1] To define an analog Γ for a relativistic quantum system is ambiguous due to effect such as saturation.

presented in the next chapter.[2]

3.1 Molecular dynamics without periodic boxes

Molecular dynamics (MD) provides a straightforward way to study the various dynamical properties of a classical many-body system. The system we are interested in is a plasma containing both electric and magnetic (and both positive and negative) charges. So in the normal convention used by plasma physics community, this is a four-component-plasma(FCP). We however would rather name it as 2E-2M-plasma to explicitly show its content. More widely speaking we may even include one more type of particles, namely dyons with both electric and magnetic charges for individual particles, making a 2E-2M-4D-plasma. In this paper we will report our results for 2E-2M-plasma with three different contents: *pure electric (which reduces to normal TCP) plasma, plasma with about one quarter of particles as magnetic charges, and plasma with about half of particles as magnetic charges, labelled throughout this paper as M00, M25, M50 respectively.* Comparison among them is expected to give indications about the role of magnetic charges, especially in the transport properties. The microscopic dynamics is classical EM, given by Newton's second law together with electric Coulomb force (between two E-charges), magnetic Coulomb force (between two M-charges) and $O(v)$ Lorentz force (between one E-charge and one M-charge).

The routine MD method (as used in GSZ[23][24] and most MD study of usual plasma) is to put desired number of particles in a cubic box and then include as many periodical image boxes (in all three directions) as allowed by computing capacity. The summation over images is very much time consuming especially for cases with Coulomb type long range forces. Also energy conservation is not very well preserved after long-time run because of the "kick" on particles leaving one truncation boundary and entering periodically on the opposite boundary which will gradually heat up the system.

Here it should be emphasized that we have used an alternative approach without any periodic boxes. What we have done is to simply give all particles certain initial conditions and then let them go. It turns out there are two different regimes which we deal with separately: 1) "plasma in cup" at medium/weak coupling regime, in which case we place a sharply rising large radial potential barrier at certain radial distance to hold the particles inside this "cup"; 2) "self-holding drop" at very strongly coupled regime, which means

[2]The works in the present chapter are based on [49].

the particles don't fall apart into small pieces but behave like a little raindrop and so there is no need for a "cup". In this way we are able to perform MD easily with thousand particles and can conserve energy for less than percent even after really long-time run. We will give more technical details about our simulations in the second subsection while present basic formulae, units and physical parameters in the first subsection .

3.1.1 Formulae,units and physical parameters

For our 2E-2M-plasma, each particle has either electric charge or magnetic charge. The E-charges are assigned as $e_i e$ with e_i randomly and equally given ± 1 ($e_i = 0$ for M-charges) and the M-charges are assigned as $g_i g$ with g_i randomly and equally given ± 1 ($g_i = 0$ for E-charges) too. For a pair of particles their mutual force involves three combinations of their charges: $e_{ij} = e_i \cdot e_j$, $g_{ij} = g_i \cdot g_j$, and an important new one $\kappa_{ij} = e_i \cdot g_j - g_i \cdot e_j$. In present study we use the same mass m for both types of charges.

The equation of motion for the ith component particle is given by:

$$m\frac{d^2\boldsymbol{r}_i}{dt^2} = \sum_{j\neq i}\left[\frac{C}{r_{ij}^{K+1}}\hat{r}_{ji} + \frac{e^2}{4\pi}\frac{e_{ij}}{r_{ij}^2}\hat{r}_{ji} + \frac{g^2}{4\pi}\frac{g_{ij}}{r_{ij}^2}\hat{r}_{ji} + \frac{ge}{4\pi}\frac{\kappa_{ij}}{r_{ij}^2}\frac{d\boldsymbol{r}_i}{c\,dt}\times\hat{r}_{ji}\right] \tag{3.1}$$

where $\boldsymbol{r}_{ji} = \boldsymbol{r}_i - \boldsymbol{r}_j$. The first term on RHS is the well-known necessary repulsive core without which all classical plasma will collapse sooner or later since no quantum effect arises at small distance to prevent positive charges falling onto negative partners. We choose $K = 9$ in our MD, which is the same as some previous work[23][24][55]. There is no particular meaning for $K = 9$ except that we want a large value of n which leads to relatively small correction ($\sim 1/K$) to potential energy between $+e$ and $-e$ at and beyond the equilibrium distance.

To set the units in our numerical study, we use the following scaling for length and time (the unit of mass is naturally set by particle mass m)

$$\begin{aligned} \tilde{\boldsymbol{r}} &= \boldsymbol{r}/r_0 \qquad with \qquad r_0 = (C/e^2)^{\frac{1}{K-1}} \\ \tilde{t} &= t/\tau \qquad with \qquad \tau = (mr_0^3/e^2)^{\frac{1}{2}} \end{aligned} \tag{3.2}$$

which leads to the dimensionless equation of motion

$$\frac{d^2\tilde{\boldsymbol{r}}_i}{d\tilde{t}^2} = \sum_{j\neq i}\Bigg[\quad \frac{1}{\tilde{r}_{ij}^{n+1}}\hat{r}_{ji} + \frac{e_{ij}}{\tilde{r}_{ij}^2}\hat{r}_{ji} + (\frac{g}{e})^2\frac{g_{ij}}{\tilde{r}_{ij}^2}\hat{r}_{ji} + (\frac{g}{e}\frac{r_0/\tau}{c})\frac{\kappa_{ij}}{\tilde{r}_{ij}^2}\frac{d\tilde{\boldsymbol{r}}_i}{d\tilde{t}}\times\hat{r}_{ji}\Bigg] \tag{3.3}$$

With these setting, we have for example: Length = # $\times r_0$, Time = # $\times\tau$, Frequency = # $\times\frac{1}{\tau}$, Velocity = # $\times\frac{r_0}{\tau}$, Energy = # $\times\frac{e^2}{r_0}$, etc. All numbers obtained from numerics are subjected to association with proper dimensional factors in our units.

Now we still have two dimensionless physical parameters which controls in the above the magnetic-related coupling strength:
1. $\tilde{g} = \frac{g}{e}$: this parameter characterizes the relative coupling strength of magnetic to electric sector. In principle there is no limitation for it from classical physics. Since we want to focus on the parametric regime which may be relevant to sQGP problem near T_c (where electric sector gets strongly coupled while magnetic sector gets weak), the parameter $\tilde{g}$ is expected to be small, so we will use $\tilde{g} = 0.1$ in the MD calculation. Naively suppose one has a quantum problem with same $\tilde{g} = g/e$, then by combination with the minimum Dirac condition $\frac{eg}{\hbar c} = \frac{e^2}{\hbar c}\tilde{g} = 1$, one gets $\alpha = \frac{e^2}{\hbar c} = 1/\tilde{g} \sim 10$ which is indeed very strongly coupled.
2. $\beta = \frac{r_0/\tau}{c} = \sqrt{\frac{e^2/r_0}{mc^2}}$: this parameter tells us how relativistic the particles' motion will typically be. The importance of this parameter lies in that it controls the strength of Lorentz force ($\beta\cdot\tilde{g}$) between E-M charges. An important observation here is that compared to the Lorentz coupling of a pure electric plasma (which is β^2 from electric current-current) our Lorentz force has only the first power of the small parameter β and is thus enhanced because of the existence of magnetic charges. Since we are doing non-relativistic molecular dynamics, a small value of β should be chosen. In the sQGP the typical speed is estimated to be about 1/3 of c, in present calculation we however will choose $\beta = 0.1$ which on one hand is not far from 1/3 and yet on the other hand limits the relativistic corrections to be not more than few percent.

One more physical parameter we should mention here is the so called plasma parameter Γ defined as the ratio of average potential kinetic energy (neglecting the sign)

$$\Gamma = \left|\frac{< U >}{< E_k >}\right| = \left|\frac{< U/N >}{3k_BT/2}\right| \tag{3.4}$$

This definition looks a little different from others[23][24][55] where usual MD study with periodic boxes defines $\Gamma = \frac{e^2/a}{k_B T}$ with $a = (3/4\pi n)^{1/3}$. They use this conveniently because in their approach the density is fixed as desired, while in our case there is no boxes any more and we use the direct ratio which is essentially meaning the same thing. The difference and relation between the two Γ values will be further discussed in section 4.1.1.

The plasma parameter Γ is important in that:
1. it distinguishes strongly coupled plasma $\Gamma >> 1$ and weakly coupled plasma $\Gamma << 1$;
2. it roughly distinguishes a gas phase $\Gamma < 1$, a liquid phase $\Gamma \sim 10$ and a solid (or solid-like) phase $\Gamma > 100$;
3. different types of plasma with the same value of Γ could be compared in order to reveal the dependence of macroscopic properties on plasma contents and microscopic dynamics, and so we will measure properties as a function of Γ.

A particular issue here is that in principle one can define two independent Γ values for the electric and magnetic components: we however choose to call them differently. As electric component is assumed to be near-dominant, with magnetic component imbedded into it: so we don't treat the latter as a separate plasma. We basically use electric Γ, plus a separate parameter $\tilde{g} = g/e$ giving the ratio of magnetic to electric couplings, and also another parameter, the relative concentration of monopoles (25%, 50% etc determining the densities). A combination of these can be formed into a magnetic Γ as Γ scales with coupling and density (under given temperature) like $g^2 \rho_M^{1/3}$.

3.1.2 Details of MD simulations

In our MD simulations, 1000 particles are initially placed on the sites of a $10\times10\times10$ cubic lattice with lattice spacing $a = 1.2r_0$ [3]. They are given electric charges ±1 in an alternating way in all 3 directions, meaning that the numbers of positive and negative electric charges exactly equal each other. Then for the M25 (M50) plasma, we randomly pick out 25% (50%) of the particles and replace their electric charges with magnetic charges which are assigned $\pm$ subsequently, thus making total magnetic charges be at most ±1. The charge neutrality of our system is preserved to $o(1/N) \sim 1/1000$. Then all the particles are randomly given initial velocity (for each of the three component) $v^i_{1,2,3}(t = 0) = V * (RANDOM\#)$ ($RANDOM\#$ is between [0,1]). In this way it is very likely that the system's total momentum is nonzero and moves

[3] This value is very close to $a = 1.18r_0$ which is calculated to be the equilibrium value of $NaCl$-like structure under our repulsive core.

as a whole, which is very inconvenient for simulation and measurements, so we subtract $1/N$-th part of the total momentum from each particle to make the center of mass stay at rest.[4] For each type of plasma, changing the value of V can eventually lead to different equilibrated system after certain time. Roughly the larger V is, the smaller (lower) the plasma parameter Γ (temperature T) will be. The total running time is $2000\Delta t$ with $\Delta t = 0.1\tau$ (which is actually our output time step). In general it takes $t_{therm} \sim 20 - 30\tau$ to equilibrate the system and we start measurements at $t = 50\tau$. The iteration step and accuracy in EoM subroutine is so chosen that the energy could be conserved to less than few percent at the end of run. As mentioned before, we have two different regimes which we will discuss the details separately in the following.

Plasma in cup

Numerically we found that for about $\Gamma < 25$, the little drop we created couldn't hold itself and after some running time it will break into a few much smaller pieces, which means the surface tension is not large enough to maintain the original "big" drop. To confine the particles in a finite volume and make them mix up sufficiently, we put a radial potential barrier at some cut-distance R_{cut} to make a container holding such plasma:

$$V = [B * (r - R_{cut})]^L * \theta(r - R_{cut}) \tag{3.5}$$

By choosing $B = 5$ and $L = 11$ we make the edge of our "cup" a really steep one, thus keeping as many particles inside the "cup" as possible at all time because only very energetic particles are able to climb up the edge a little and will soon be reflected back. In our simulations we have used $R_{cut} = 11r_0$. In real time of course the number of particles confined within the R_{cut} is always fluctuating, so are other macroscopic quantities like energy etc. So this system is like a grand-canonical ensemble. For this plasma in cup, all the measurements are made for particles inside the cup only (namely with $r \leq R_{cut}$).

By looking at the histogram of total number of particles at different time points in Fig.3.1, one see that the system has very good distribution with well-defined average $N \sim 950$ and $\sqrt{N} \sim 30$ fluctuation width[5]. Another important

[4]Selection of global "quantum" numbers like total charge or momentum leads to $o(1/N)$ corrections (which vanish only in thermodynamic limit) when we go to canonical observable: this is not a problem at all as compared to other corrections like surface effect $o(1/N^{1/3})$.

[5]This $\sqrt{N}$ estimate is supposed to be exact only for an ideal gas while our system is more like a non-ideal-gas/liquid, so one expects certain coefficient times $\sqrt{N}$, with its value depending on the EoS.

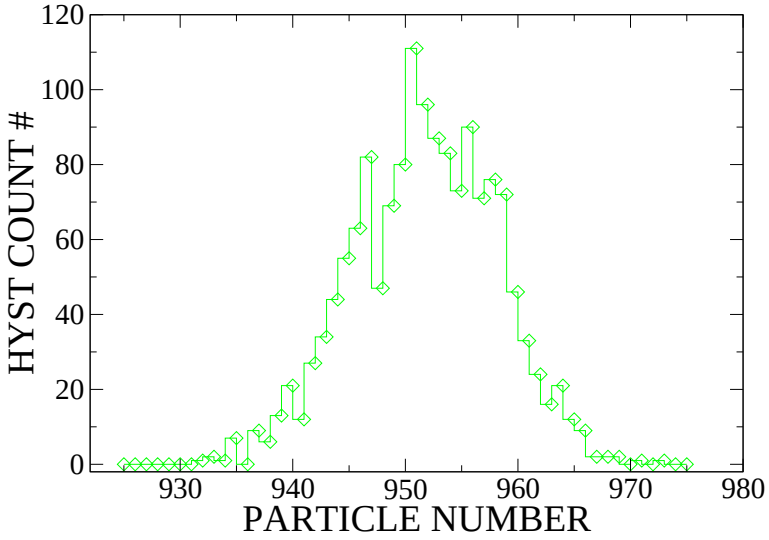

Figure 3.1: (color online) Histogram of total number of particles inside R_{cut} at 1500 different time points. This is an example for M25 plasma at $\Gamma = 0.99$.

check is to see if the system is really homogeneous. In Fig.3.2 we have plotted the radial particle density $n(r)$ versus radial volume $V(r) = r^3 4\pi/3$ with bin size $\Delta V = 100 \cdot 4\pi/3 = 419$. The time-averaged curve (solid) is rather flat, with standard deviation bound(orange dashed) close (yet not equal) to simple $\sqrt{N}$ deviation bound(violet dashed). Also densities at five particular time points (from early to very late time) are shown, basically fluctuating around average within the deviation. From this plot it is clear that the density distribution is homogeneous and stable enough, with fluctuations expected for a non-idea-gas/liquid behavior. One can also see that near our cutting edge ($R_{cut} = 11$) the particle density quickly drops down as we want. These observations are true in all of our runs, and the number density of our cupped plasma at different Γ is controlled all at $n \approx 0.17$ with negligible variation. These have shown that our simulations for cupped plasma is reliable.

It is also important to check the fluctuation in energy. In Fig.3.3 we show a typical histogram of fluctuation in kinetic and potential energy at all time points. Clearly both distributions make complete sense and so are other macroscopic variables which we skip because of limited space. The relative fluctuations of kinetic and potential energy are larger than that of the particle number (as expected) because of extra broadening due to conversion between kinetic and potential energy. Again these justify our "plasma-in-cup" approach.

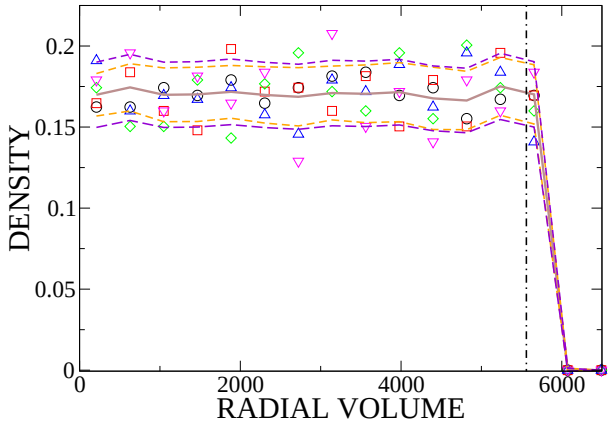

Figure 3.2: (color online) Radial particle density plotted versus radial volume $V(r) = r^3 4\pi/3$ with bin size $\Delta V = 100 \cdot 4\pi/3 = 419$. The central thick brown solid line is the average over all time points, with the up/down orange dashed lines showing standard deviation and the up/down violet dashed lines given by $\sqrt{N}$ deviation, and the five types of symbols are densities taken from five different time points. The vertical dash-dotted line indicates the cutting edge position R_{cut}. This is an example for M25 plasma at $\Gamma = 0.99$.

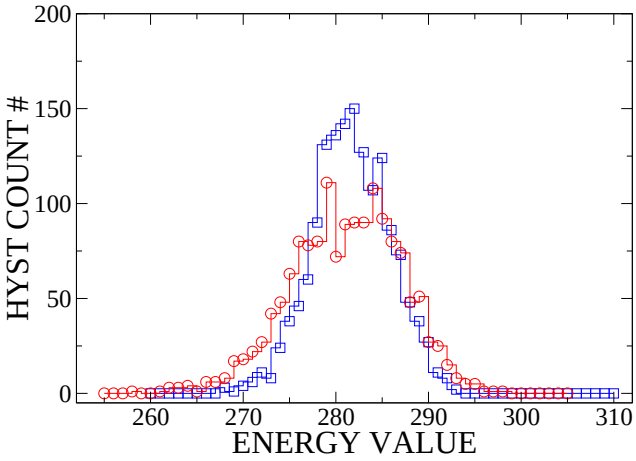

Figure 3.3: (color online) Histogram of total kinetic(blue square) and potential(red circle)energy inside R_{cut} at 1500 different time points. This is an example for M25 plasma at $\Gamma = 0.99$.

The results to be reported in Section IV. and V. are all obtained with this method, which cover the Γ value about $0.3 - 14$. We want to focus on this region because it is most relevant to the sQGP.

Self-holding drop

For about $\Gamma > 25$ we have found our little drop can, amazingly, hold itself despite the possible expansion and shrinking with considerable amplitude. By mapping the particles' coordinates at the end of run we found the particles more or less staying around their original positions. This very strongly coupled system behaves more like a crystal, especially for $\Gamma \to 100$. In this regime, we have found very good collective modes which are shown to manifest themselves in the dynamical correlation functions in a profound way. These results will be reported in section VI. It should be pointed out that the self-holding region is reached only for pure electric plasma (our M00 plasma). For our M25/M50 plasma, with present method the largest Γ that can be achieved (after "cooling" and equilibrating scheme) and maintained in a stable way is up to ~ 25. The "cooling" method, namely turning on a braking force proportional to particle velocity for some time and then turning it off, can bring the M25/M50 system down to some instant $\Gamma \sim 1000$ but then the system kinetic energy slowly but steadily keeps increasing with potential energy getting more negative, the overall effect of which eventually increases Γ back down to few tens. It seems indicating the mixture plasma refuses to become solidified even at classical level because of Lorentz type force (different from permanent liquid Helium which is due to quantum effect). We will leave this issue for future investigation.

3.2 Equation of state

Before showing the data, we once again emphasize that the goal is to compare three types of plasma (M00, M25, and M50) with different E-charges and M-charge concentration, and all the comparison will be made by plotting certain macroscopic properties as a function of plasma parameter Γ.

The first quantity we want to look at is the temperature[6] dependence on Γ which is sort of equation of state for plasma.[7] In Fig.3.4 the EoS for M00,

[6]By temperature T we actually mean $k_B T$ (with the dimension of energy in our units) throughout this paper.

[7]Remember in this classical statistical system the average kinetic energy per particle is

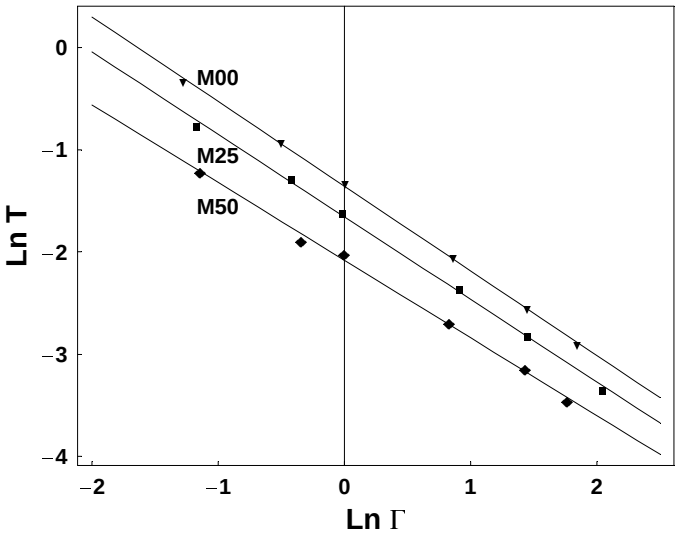

Figure 3.4: Temperature T calculated at different plasma parameter Γ in log-log plot for M00(triangle), M25(square), and M50(diamond) plasma respectively, with the three lines from linear fitting (see text).

M25, and M50 are compared in log-log plots. Data for all three show a linear relation with similar slopes but different intercepts. By simple linear fitting we get the following parameterized EoS for them:

$$\begin{aligned} M00 \quad &: \quad T = 0.257 \,/\, \Gamma^{0.827} \\ M25 \quad &: \quad T = 0.191 \,/\, \Gamma^{0.806} \\ M50 \quad &: \quad T = 0.125 \,/\, \Gamma^{0.759} \end{aligned} \tag{3.6}$$

So already from the EoS we've seen considerable difference among the three plasma. Since EoS is important for dynamical processes, we proceed to study correlation functions and transport coefficients in next section, expecting to see more differences.

given by $E_k = 3T/2$ and total energy per particle is $E = (1-\Gamma) * E_k$, so the temperature dependence on Γ also gives all information on energy. To determine E_k we simply sum up the kinetic energy ($\sum_i m\, v_i^2/2$) of each particle then divide it by the total number of particles.

3.3 Correlation functions and transport coefficients

Study of transport coefficients is very important in order to understand the experimental discoveries about sQGP, such as the very low viscosity and the diffusion of heavy quarks. In this section the transport coefficients of our three different plasma will be calculated and compared in order to see the influence of magnetic charges on the transport properties. To do that, we will first measure certain correlation functions and then relate them to the corresponding transport coefficients through the Kubo-type formulae, as is usually done in MD works.

3.3.1 Velocity autocorrelation and diffusion constant

The first correlation function we will study is the velocity autocorrelation which is defined as:

$$D(\tau) = \frac{1}{3N} < \sum_{i=1}^{N} \boldsymbol{v}_i(\tau) \cdot \boldsymbol{v}_i(0) > \tag{3.7}$$

Here τ is the correlation time, $\boldsymbol{v}_i$ denotes the velocity of the ith particles and the sum is over all particles. The average is over thermal ensemble which is done in numerical program by average over all time points[8] (with the number typically of order $\sim few$ 1000).

In Fig.3.5 we show typical curves for velocity autocorrelation function in M00, M25, and M50 plasma respectively. A fast damping behavior at small correlation time is observed, followed by small fluctuation from random noise at longer correlation time.

The corresponding transport coefficient, namely diffusion constant, is calculated by the following Kubo formula

$$D = \int_0^\infty D(\tau)\, d\tau \tag{3.8}$$

In Fig.3.6 we plot $LogD$ as a function of $Log\Gamma$ for M00,M25 and M50 plasma. Approximate linear relation is seen for all three, but with visible difference in slopes and intercepts. A linear fit gives the following approximate

[8]The time average essentially provides ensemble average.

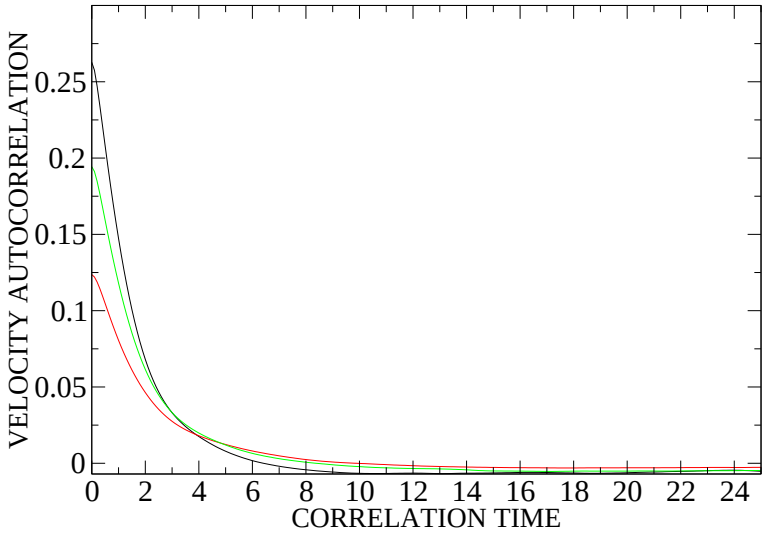

Figure 3.5: (color online) Velocity autocorrelation functions $D(\tau)$ for (from top down at zero time) M00(black curve), M25(green curve) and M50(red curve) plasma, taken at $\Gamma = 1.01, 0.99, 1.00$ respectively.

functions $D(\Gamma)$:

$$\begin{aligned} M00 \quad &: \quad D = 0.396 \,/\, \Gamma^{0.752} \\ M25 \quad &: \quad D = 0.342 \,/\, \Gamma^{0.707} \\ M50 \quad &: \quad D = 0.273 \,/\, \Gamma^{0.626} \end{aligned} \tag{3.9}$$

At small $\Gamma < 1$ there are considerable differences of the three lines. In the physically interesting region $\Gamma \sim 1 - 10$ the three plasma have visible but not too much difference in diffusion constants. The three lines will cross at about $\Gamma \sim 10$ and after that deviation from each other again grows quickly. The important feature common to all three types of plasma as well as to cQGP model in [23][24] is the power-law dropping of diffusion constant with increasing coupling strength. We see the diffusion constant can become few orders of magnitude smaller when one changes from weakly coupled gaseous regime into strongly coupled liquid regime. This qualitative scaling in coupling is also found from AdS/CFT calculation by Casalderrey-Solana and Teaney in [56].

Interestingly if one combines (3.9) and (3.6), the dependence of D on T is

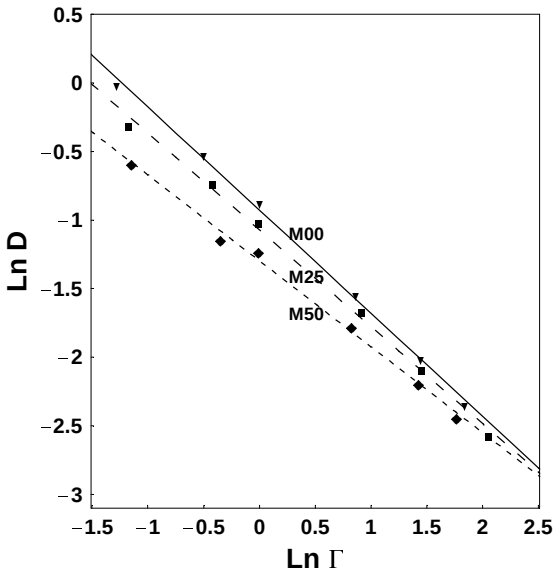

Figure 3.6: Diffusion constant D calculated at different plasma parameter Γ in log-log plot for M00(triangle), M25(square), and M50(diamond) plasma respectively, with the three lines from linear fitting (see text).

then obtained:

$$\begin{aligned} M00 &: D = 1.36\,T^{0.91} \\ M25 &: D = 1.46\,T^{0.88} \\ M50 &: D = 1.52\,T^{0.82} \end{aligned} \tag{3.10}$$

3.3.2 Stress tensor autocorrelation and shear viscosity

It is of particular interest to study the shear viscosity of our three plasma, as the low viscosity is one of the most important discoveries for sQGP from RHIC experiments. For this purpose, one can measure the autocorrelation of the off-diagonal elements of stress tensor, namely

$$\eta(\tau) = \frac{1}{3VT} < \sum_{l<k}^{1,2,3} \mathcal{T}_{lk}(\tau)\mathcal{T}_{lk}(0) > \tag{3.11}$$

with the stress tensor off-diagonal elements

$$\begin{aligned}\mathcal{T}_{lk} &= \sum_{i=1}^{N} m(\boldsymbol{v}_i)_l(\boldsymbol{v}_i)_k + \frac{1}{2}\sum_{i\neq j}(\boldsymbol{r}_{ij})_l(\boldsymbol{F}_{ij})_k \\ &= \sum_{i=1}^{N} m(\boldsymbol{v}_i)_l(\boldsymbol{v}_i)_k + \sum_{i=1}^{N} m(\boldsymbol{r}_i)_l(\boldsymbol{a}_i)_k \end{aligned} \tag{3.12}$$

In the above equations i, j refer to particles while l, k refer to components of three-vectors like separation, velocity and force. $\boldsymbol{r}_{ij}$ and $\boldsymbol{F}_{ij}$ are the separation and force from particle i to particle j respectively, while $\boldsymbol{r}_i, \boldsymbol{v}_i, \boldsymbol{a}_i$ are the position, velocity, acceleration of particle i. The equivalence of the two expressions in the second equation is discussed in great details in [57]. The V in the first equation is the system volume. In Fig.3.7 typical plots of $\eta(\tau)$ for three plasma are shown. Again the relaxation of real correlation is pretty quick and noises dominate the later time. With these correlation functions at hand the Kubo formula then leads to the following shear viscosity η:

$$\eta = \int_0^\infty \eta(\tau)d\tau \tag{3.13}$$

In general shear viscosity is a complicated property of many-body systems, the value of which depends on many factors in a nontrivial way. Roughly, a system with either very small Γ (like a gas) or very large Γ (like a solid) will have large viscosity while a system in between (like a liquid) will have low viscosity with a minimum usually in $\Gamma = 1 \sim 10$(see for example [23][58]). A qualitative explanation is that both the particles in a gas and the phonons in a solid can propagate very far (having a large mean-free-path) and transfer momenta between well-separated parts, thus producing a large viscosity, while in a liquid neither particles nor collective modes could go far between subsequent scattering, thus making momenta transfer very much localized and leading to a low viscosity.

Now turning to our plasma with magnetic charges, since we have a relatively weakly-coupled magnetic sector, one may wonder if the magnetic particles will contribute more to large-distance momenta transfer and hence increase the viscosity significantly. We however argue that in the opposite, the Lorentz force induced by the existence of magnetic charges will somehow confuse particles and collective modes, thus helping keep the viscosity to be low. Indeed, as shown in Fig.3.8, the viscosity goes down as increasing concentration of magnetic charges. At small $\Gamma < 1$ (in the gas phase) the three curves are getting close to each other, but when Γ increases into the liquid region ≥ 1 there is a

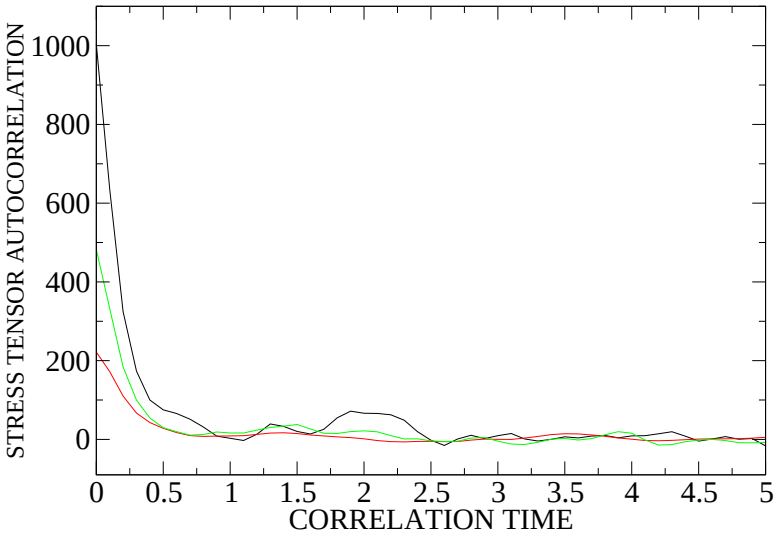

Figure 3.7: (color online) Stress tensor autocorrelation functions $\eta(\tau)$ for (from top down at zero time) M00(black curve), M25(green curve) and M50(red curve) plasma, taken at $\Gamma = 1.01, 0.99, 1.00$ respectively.

considerable decrease of viscosity in M25 and even more in M50 plasma. The M50 with E-charges and M-charges to be 50%-50%, has the values of viscosity about half of the pure electric M00 plasma at the same Γ. So, we conclude that the existence of magnetic charges may help us to understand the extremely low viscosity of sQGP. A rough parametrization of the data gives the following viscosity dependence on Γ in the plotted region:

$$\begin{aligned} M00 \quad &: \quad \eta = 0.002\,/\,\Gamma^{\,3.64} + 0.168\,/\,\Gamma^{\,0.353} \\ M25 \quad &: \quad \eta = 0.013\,/\,\Gamma^{\,1.36} + 0.105\,/\,\Gamma^{\,0.237} \\ M50 \quad &: \quad \eta = 0.096\,/\,\Gamma^{\,0.500} + 0.001\,\cdot\,\Gamma^{\,1.12} \end{aligned} \tag{3.14}$$

In all of them the first term is most dominant at very small Γ while the second term becomes important at relatively large Γ. We noticed that for M50 there is already positive power term of Γ, which is in accord with the expected qualitative feature. Similar terms will appear in two other plasma when we will be able to include in the fitting more points from large Γ. At larger Γ we expect growing viscosity, as other MD calculations (like GSZ) in the past reported. We do not report results for such values of Γ in the paper precisely because in this case collective modes (eg. the non-diagonal quadruple one) is

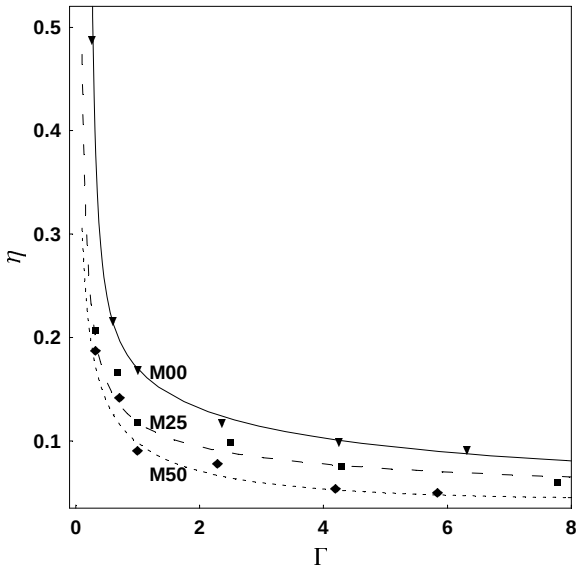

Figure 3.8: Shear viscosity η calculated at different plasma parameter Γ for M00(circle), M25(square), and M50(diamond) plasma respectively.

so persistent that during our observation time it does not decay well enough to get reliable integral of the appropriate correlation function in Kubo formula: this point will be demonstrated in details in the next section. Since however we are motivated by QGP physics in general, the transport coefficients of the Γ region shown in Fig.3.6,3.8 are most interesting.

3.3.3 Electric current autocorrelation and conductivity

The last transport property we study in this paper is the electric current autocorrelation and the electric conductivity. This analysis is only done for pure electric M00 plasma since the comparison among M00, M25 and M50 (which already have different E-charge concentrations) doesn't make much sense. The electric current autocorrelation is given by

$$\sigma(\tau) = \frac{1}{3VT} < (\sum_{i=1}^{N} e_i \boldsymbol{v}_i(\tau)) \cdot (\sum_{i=1}^{N} e_i \boldsymbol{v}_i(0)) > \tag{3.15}$$

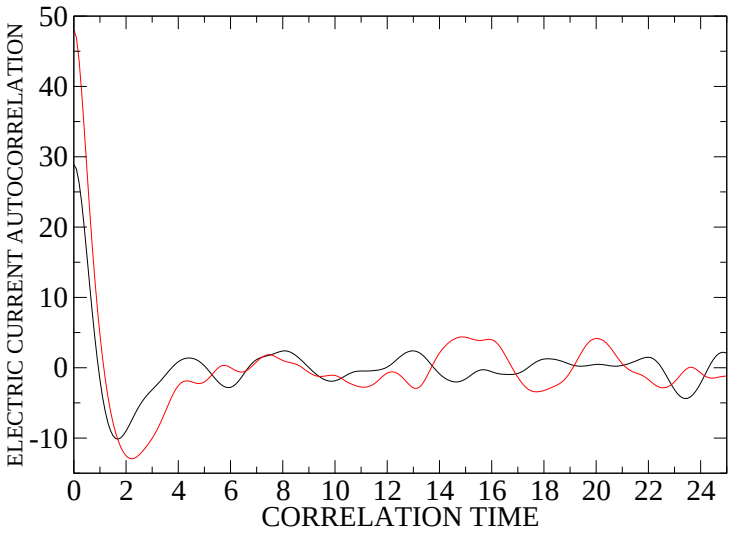

Figure 3.9: (color online) Electric current autocorrelation functions $\sigma(\tau)$ for pure electric M00 plasma taken at (from top down at zero time) $\Gamma = 6.33$(red curve) and $\Gamma = 14.53$(black curve).

with e_i the electric charge of the ith particle. And the electric conductivity is obtained from Kubo formula as

$$\sigma = \int_0^\infty \sigma(\tau) d\tau \tag{3.16}$$

In Fig.3.9 we show the typical $\sigma(\tau)$ as a function of τ for two values of Γ. For this correlation function we do notice that even for Γ not large, the late time correlation is not purely noise but still has small oscillation. This is not unreasonable since related collective modes like plasmon may develop even for a gas. After integration it turns out in the region $\Gamma \sim 0.3 - 15$ the conductivity is scattered between $\sigma = 0.101 - 0.141$ without clear tendency, which may indicate the electric current dissipation is not sensitive to Γ in this region. It is very interesting to see what will happen to the color-electric conductivity (giving information about color charge transport) in a Non-Abelian plasma.

3.4 Collective excitations at very strongly coupled regime

In this section we will report interesting results for collective excitations found at very strongly coupled regime (Γ greater than a few tens) of the pure electric (M00) plasma[9]. The signals of these excitations are extraordinarily clear when Γ goes to ~ 100 or larger. We came to notice these very good modes not in a straight forward way. Instead, these modes have revealed themselves dramatically in some unusual structures of the dynamical correlation functions and their fourier spectra, which we measured first. Only after thinking about possible source of these structures we turned to systematic and direct measurements for certain collective modes, which are found to coincide with correlation functions' structures in a distinct manner. As mentioned before, in this regime our plasma is like a "self-holding drop" which has very different collective motions from a plasma in periodic boxes: the latter has the familiar phonon modes while the former is really like a raindrop, having vibration modes like monopole modes, dipole modes, quadruple modes, etc corresponding to different components of density distribution's spherical harmonics. We will discuss these modes respectively in more details in the following.

3.4.1 Monopole modes

Let's start with the velocity autocorrelation function (3.7) which is supposed to almost vanish (except a little random noise) at large correlation time and give convergent integral to yield diffusion constant, as seen in previous section. However when measured in the very strongly coupled regime, this correlation function is found to have robust oscillating behavior even for very large time which of course couldn't be considered as noise, see Fig.3.10. By looking at the fourier spectrum of it, one immediately sees a large and narrow peak at $\omega_1^D = 0.35$ very clearly on top of a very broad shoulder structure, as shown in Fig.3.11. These behaviors are true for Γ down to about 50.

Now the question is why there will be such peaks in velocity autocorrelation. The answer lies in the monopole modes, which can be directly measured through simply the time dependence of average particle radial position, namely:

$$R(t) = \frac{1}{N}\sum_{i=1}^{N} |\boldsymbol{r}_i(t)| \tag{3.17}$$

[9]Though this section is not very much related to the main theme of the thesis, it shows the power of our MD approach and obtains results of their own interest.

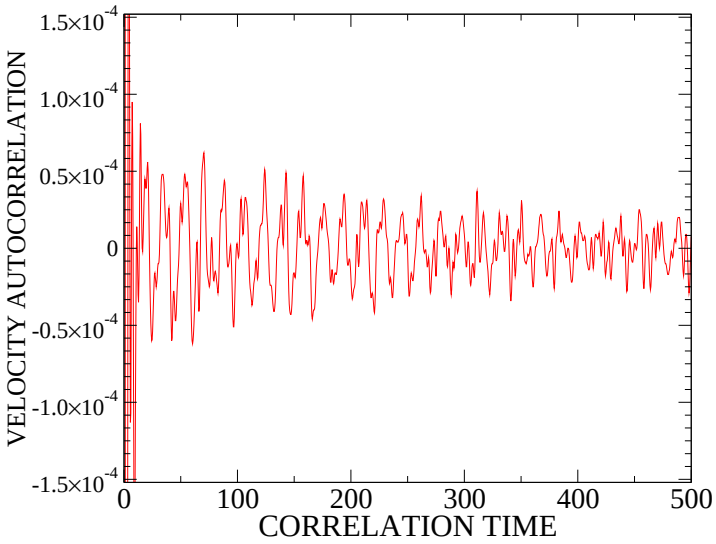

Figure 3.10: (color online) Velocity autocorrelation function taken at $\Gamma = 116.91$.

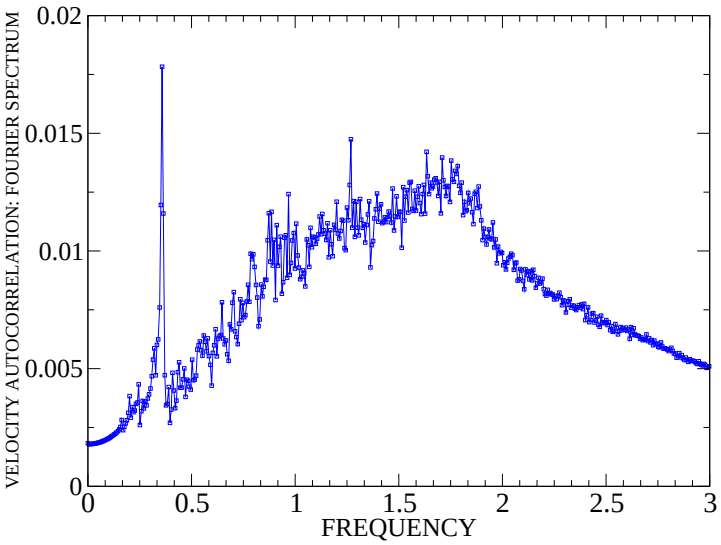

Figure 3.11: (color online) Fourier transformed spectrum of velocity autocorrelation function taken at $\Gamma = 116.91$.

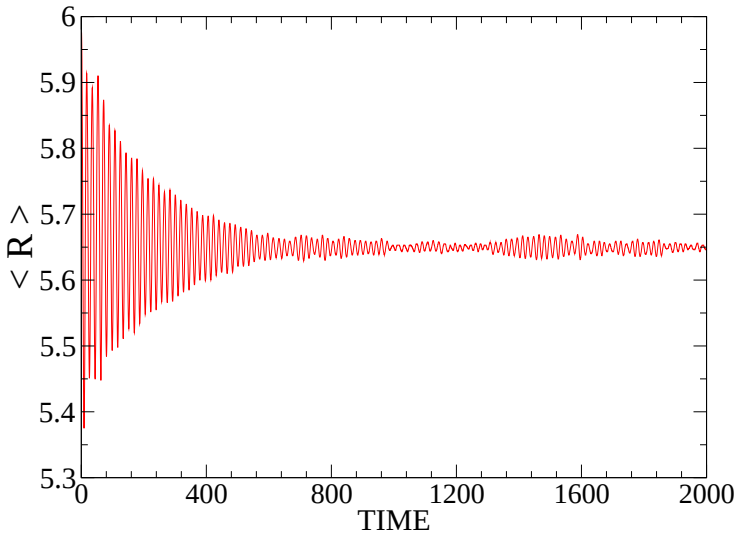

Figure 3.12: (color online) Average monopole moment $R(t)$ (see text) as a function of time, taken at $\Gamma = 116.91$.

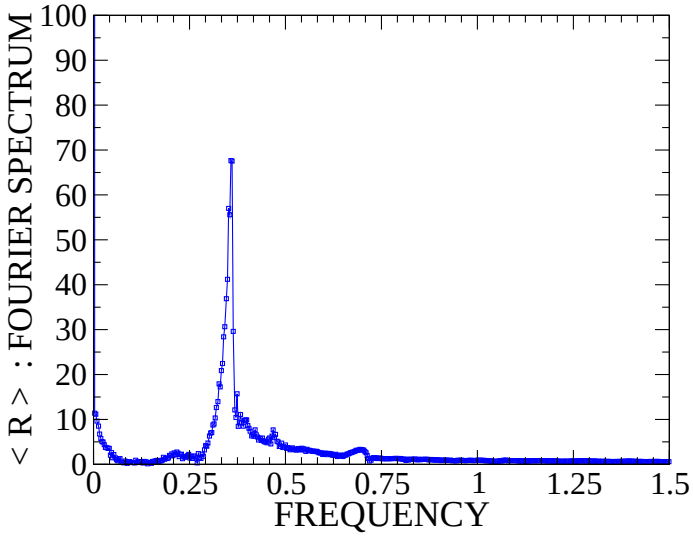

Figure 3.13: (color online) Fourier transformed spectrum of average monopole moment $R(t)$(see text), taken at $\Gamma = 116.91$.

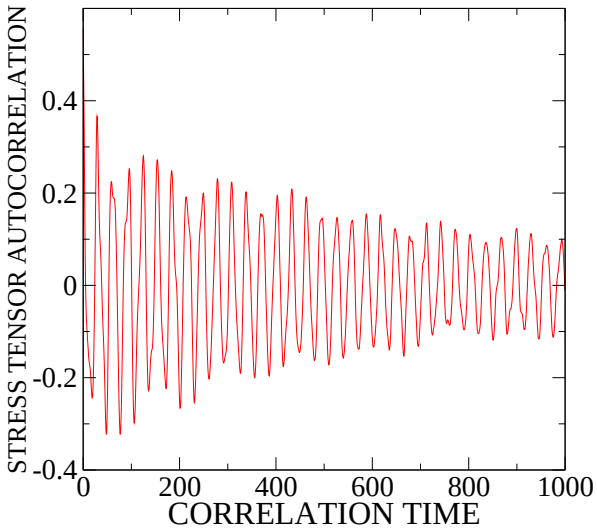

Figure 3.14: (color online) Stress tensor autocorrelation function taken at $\Gamma = 116.91$.

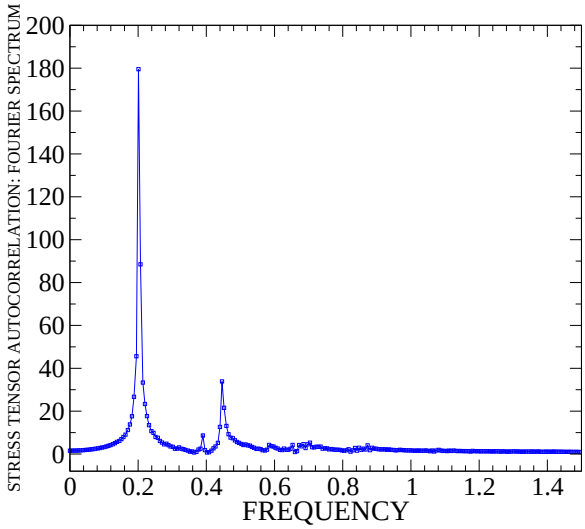

Figure 3.15: (color online) Fourier transformed spectrum of stress tensor autocorrelation function taken at $\Gamma = 116.91$.

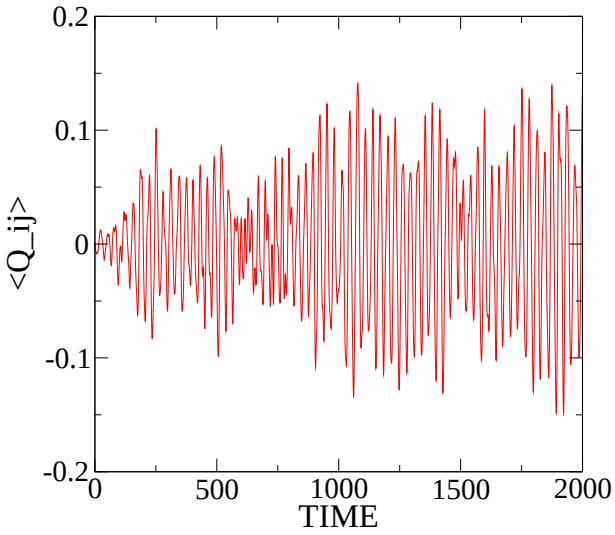

Figure 3.16: (color online) Average off-diagonal quadruple moment $Q_{23}(t)$ (see text) as a function of time, taken at $\Gamma = 116.91$.

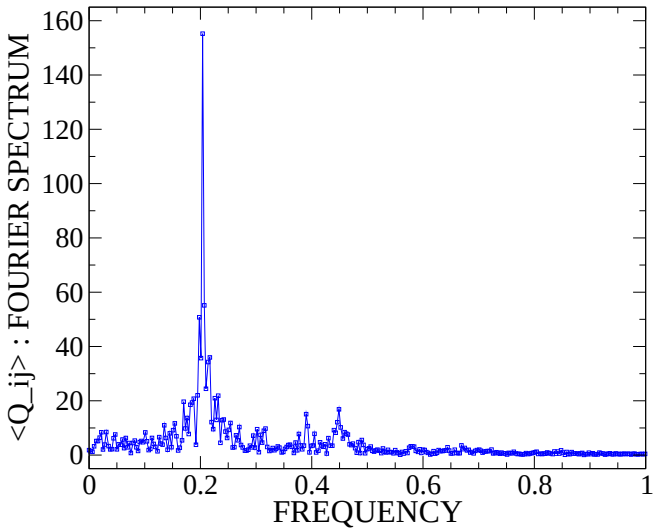

Figure 3.17: (color online) Fourier transformed spectrum of average off-diagonal quadruple moment $Q_{23}(t)$ (see text), taken at $\Gamma = 116.91$.

In Fig.3.12 one sees really nice oscillations lasting for near hundred revolutions. In a small movie showing the positions of particles at several subsequent time points the "drop" in monopole mode looks like a beating heat. This oscillation amplitude decreases slowly indicating a nonzero but small width of this monopole mode. Again the fourier spectrum gives important information such as the characteristic frequency and width of collective mode. In Fig.3.13 we can see one major narrow peak at $\omega_1^M = 0.35$ together with a few roughly visible but much smaller lumps at $\omega = 0.22, 0.46, 0.70$. $\omega = 0.70$ structure may be a secondary harmonics of the major peak, and seemingly the 0.22 and 0.46 may also be in the same series of harmonics with different ranks.

The important finding we want to point out is the coincidence of ω_1^M here with the peak ω_1^D from velocity autocorrelation function. This result tells us the monopole mode, in a form of radial vibration, has nontrivial influence on velocity autocorrelation and consequently on particle diffusion.

3.4.2 Quadruple modes

The study of stress tensor autocorrelation in the strongly coupled plasma gives us even more interesting correspondence between correlation functions and collective modes. In Fig.3.14 we plot the stress tensor autocorrelation (3.11) as a function of time, and in Fig.3.15 its fourier spectrum, in which three clear and narrow peaks can be seen at $\omega_1^\eta = 0.20$, $\omega_2^\eta = 0.40$, and $\omega_3^\eta = 0.45$. The 0.40 peak, which is the smallest one, may be a secondary harmonics of the remarkable 0.20 peak. At Γ as small as about 25, the 0.20 peak is still alive in this correlation function. Because of the existence of these, the correlation function has significant oscillations with large amplitude even for very large correlation time.

To find the source of these, we directly measured the off-diagonal quadruple modes by the following probe:

$$Q_{lk}(t) = \frac{1}{N}\sum_{i=1}^{N}(\boldsymbol{r}_i(t))_l(\boldsymbol{r}_i(t))_k \quad , l,k = 1,2,3, \quad l \neq k \tag{3.18}$$

We have three independent of them, say Q_{12}, Q_{23}, Q_{31}. In Fig.3.16 we show one of them as a function of time with similar results for the other two. From the figure we can see that at the very beginning there is almost no quadruple mode but its amplitude grows significantly in a time interval $0 - 200$ during which the monopole mode decays down (see Fig.3.12). Then after that they persist for long time. This indicates that these off-diagonal quadruple modes are very robust and somehow "cheap" to excite and the energy initially in the

monopole modes is preferably transferred into the quadruple modes.

Now when we plot the fourier spectrum of the off-diagonal quadruple modes in Fig.3.17, amazingly three very clear peaks appear at $\omega_1^Q = 0.20$, $\omega_2^Q = 0.40$, and $\omega_3^Q = 0.45$, which are exactly the same frequencies found in the stress tensor autocorrelation. The relative amplitudes among the three peaks are also similar in two cases. This is a profound correspondence which means the stress tensor correlation and the related transport property, namely viscosity, are especially dominated by the off-diagonal quadruple modes of the system. This type of connection may be universal and one may find certain collective excitations for each dynamical correlation function.

Before closing this subsection, let's also mention the diagonal quadruple modes which we also studied. This part of quadruples could be probed by the following quantity:

$$Q_{ll}(t) = \frac{1}{N}\sum_{i=1}^{N}\left[3((\boldsymbol{r}_i(t))_l)^2 - |\boldsymbol{r}_i(t)|^2\right] \quad , l = 1, 2, 3 \tag{3.19}$$

It has similar behavior as the off-diagonal modes (to save space we skip to show the plots) , with peaks in spectrum at $\omega_4^Q = 0.12$ and $\omega_5^Q = 0.25$ which presumably are different ranks in the same harmonic series. These peaks however are not seen in the stress tensor autocorrelation, which is understandable since the stress tensor autocorrelation we study is actually the correlation of stress tensor's off-diagonal parts which is related to shear viscosity. We think these peaks of diagonal quadruple modes must be seen in the diagonal parts of stress tensor correlation which is related to the bulk viscosity.

3.4.3 Plasmon modes

It is clear that our "drop" won't have dipole (or any odd-multiple) excitation according to symmetric setting. But there can be another type of dipole excitations, namely the electric dipole modes, or in a more common notion the plasmon modes. These can be probed by

$$(e\boldsymbol{R})_l(t) = \frac{1}{N}\sum_{i=1}^{N} e_i(\boldsymbol{r}_i(t))_l \quad , l = 1, 2, 3 \tag{3.20}$$

The corresponding correlation function should be the electric current autocorrelation (3.15). To clearly reveal these modes we shift our positive charges and negative charges with small displacement in opposite directions at the

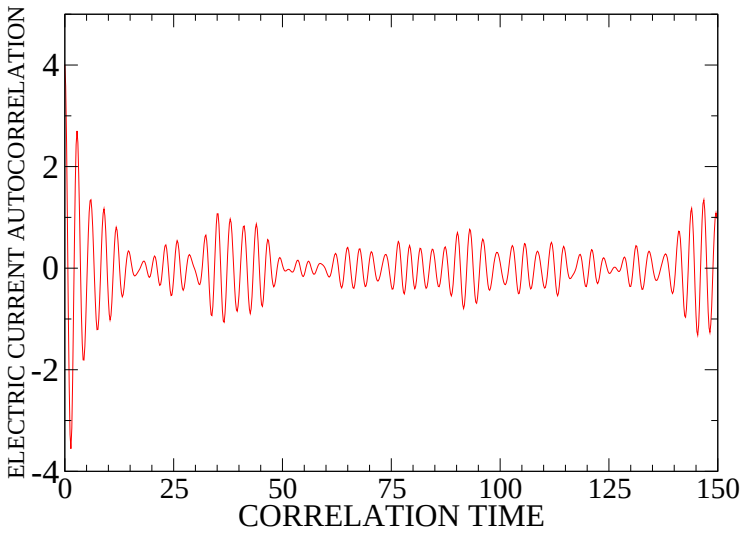

Figure 3.18: (color online) Electric current autocorrelation function taken at $\Gamma = 184.00$.

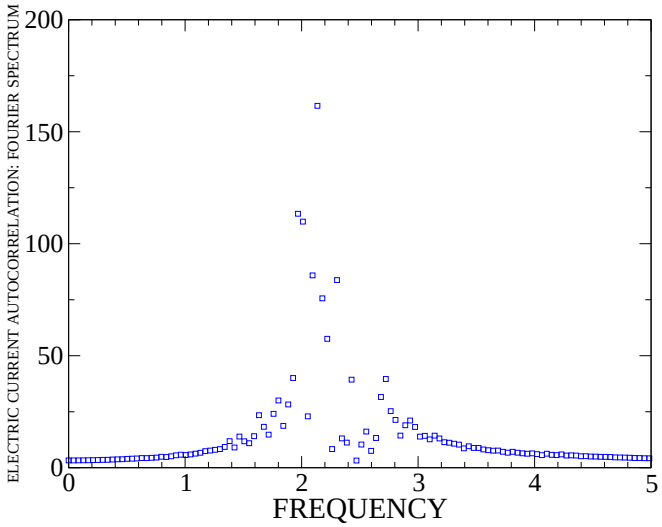

Figure 3.19: (color online) Fourier transformed spectrum of electric current autocorrelation function taken at $\Gamma = 184.00$.

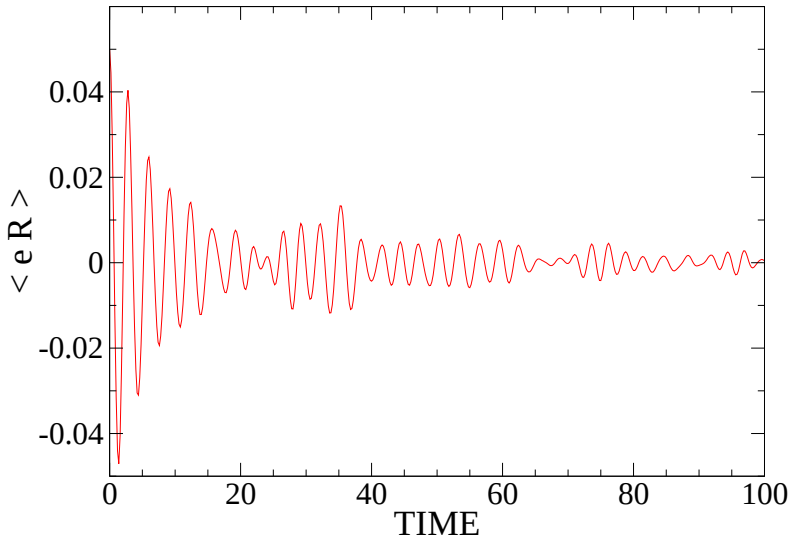

Figure 3.20: (color online) Average electric dipole moment $eR(t)$ (see text) as a function of time, taken at $\Gamma = 184.00$.

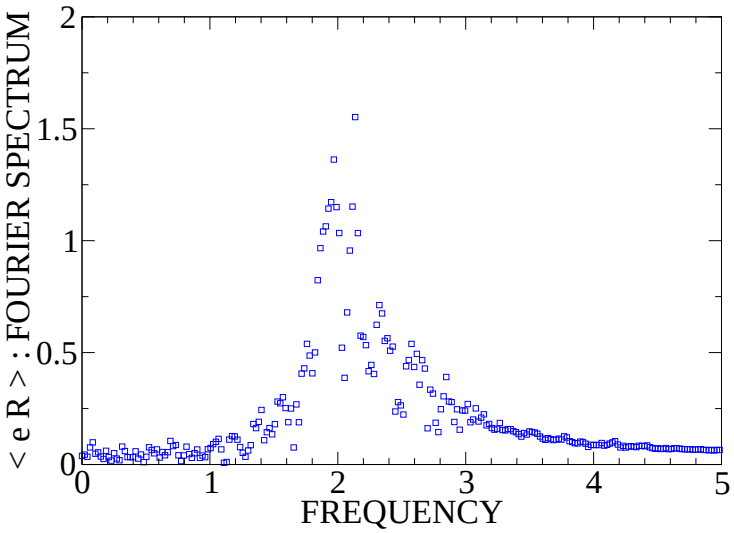

Figure 3.21: (color online) Fourier transformed spectrum of average electric dipole moment $eR(t)$ (see text), taken at $\Gamma = 184.00$.

initial time which introduces zero dipole but nonzero electric dipole. We then plot the electric current autocorrelation (Fig.3.18) and its fourier spectrum (Fig.3.19), and the direct electric dipole (Fig.3.20) and its fourier spectrum (Fig.3.21) as well.

Again one see similar behavior in both and find similar peak structure at $\omega^J = \omega^E = 2.0$ in both spectra. These peaks are large but broad and have some fluctuation, as compared with previous peaks, which is understandable as the plasmon modes usually have bigger width (larger dissipation) than sound modes. These modes seem to be present even if the system has only $\Gamma \sim 10$. If one calculate the plasmon frequency using the simple formula $\omega_p = \sqrt{\frac{4\pi ne^2}{m}}$ for our drop (with $n = 1/a^3$, $a = 1.18\lambda$) we then get $\omega_p = 2.7$. This is not far from the observed 2.0 and the discrepancy must be there because the size of our system is only about 10 times the microscopic scale and the positive and negative charges in the middle are not entirely screening each other as assumed when deriving the formula.

3.4.4 Size scaling of the collective modes

Since the monopole and quadruple modes should be sound modes, it is interesting to see how their frequencies scale with the system size. For a large enough system one expects the sound modes dispersion to be $\omega = c_s k - \frac{i}{2}\Gamma_s k^2$, namely the mode frequency itself scales linearly in k while the width scales quadratically. What we did is to change system size to be $10 \times 10 \times 10$, $8 \times 8 \times 8$, $6 \times 6 \times 6$, and $4 \times 4 \times 4$, and then look at the change of peaks in those monopole and quadruple modes (picking the major peaks ω_1^M, ω_1^Q and ω_5^Q). As demonstrated in Fig.3.22 where these frequencies are shown as function of $2\pi/L$ with L the system size, the linear scaling is very well observed. We obtain the following linear fitting for the three modes:

$$\begin{aligned} Monopole &: \omega_1^M = 0.610 \cdot k \\ Quadruple\, D &: \omega_5^Q = 0.404 \cdot k \\ Quadruple\, N-D &: \omega_1^Q = 0.329 \cdot k \end{aligned} \tag{3.21}$$

The two quadruple modes have similar slope (with the diagonal one a little larger) which means they have close propagation velocity, while the monopole modes have a slope or propagation velocity larger by a factor about $1.5 - 2$. This is reasonable, just like in usual solid the longitudinal sound waves have larger velocity than the transverse ones. The lines show remarkable consistency with the fact that sound modes with infinitely large wavelength should have zero frequency. For the width however we didn't unambiguously see a regular

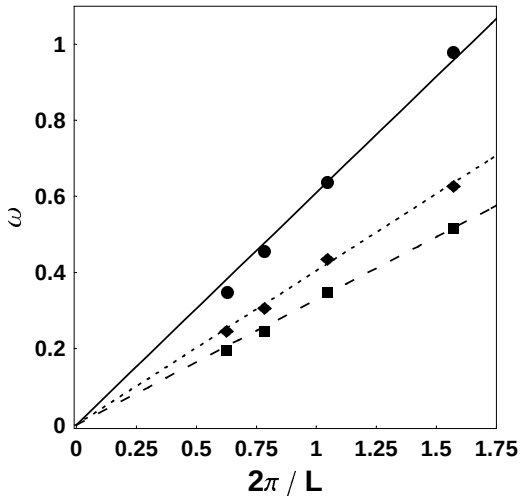

Figure 3.22: Peak frequency as a function of $2\pi/L$ (with L the system size) for monopole modes(circle), diagonal quadruple modes(diamond), and off-diagonal quadruple modes(square) respectively, with the three lines from linear fitting (see text).

dependence on L, which indicates our systems are not macroscopic enough since the width is more sensitive than frequency itself to the dissipation effect related to system size.

The last result to mention is about the dependence of plasmon modes on system size. Actually we found for all four sizes, the plasmon frequencies roughly stay around $\omega^E = 2.0$ without changing, only with the peak structure getting worse. Again this is expected since the usual plasmon dispersion displays a plateau at $\omega_p = \sqrt{\frac{4\pi ne^2}{m}}$ for k not large.

Chapter 4

Magnetic Component of sQGP Is a Good Liquid

In this chapter, we present the main results that have supported our magnetic scenario for sQGP. These come from several different aspects: 1) by comparing MD predictions of shear viscosity and diffusion constant for sQGP with the empirical data from RHIC experiments; 2) by exploring the "magnetic bottle" effect which is shown capable of leading to liquid-type transport properties; 3) by analyzing the monopole-anti-monopole equal-time spatial correlation functions obtained both from our MD results and from the dedicated lattice data; 4) by studying the magnetic running coupling and the multi-body plasma parameter of the magnetic sector. A coherent and natural integration of all these has led us to the conclusion that magnetic component of sQGP is a good liquid.[1]

4.1 MD predictions for sQGP

4.1.1 Mapping between MD systems and sQGP

With the MD-obtained empirical formulae for diffusion and viscosity, it is of great interest to see what they predict for the parameter region corresponding to the sQGP experimentally created at RHIC. To do this mapping, one has to identify the corresponding physical values of basic units (namely mass, length and time) in the destination system and then combine dimensionless numbers and relations from MD with proper dimensions. Also the plasma parameter Γ should be determined for the destination system such that we pick up the

[1]The works in the present chapter are based on [49][59].

MD-predicted values of interesting quantities (say, diffusion constant and shear viscosity) at exactly the same Γ value.

Following similar estimates as in [23], we summarize below the relevant quantities of sQGP around $1.5T_c$:
1. Quasiparticle (quarks and gluons) mass can be estimated as $m \approx 3.0T$;
2. The typical length scale is simply estimated from quantum localization to be $r_0 \approx 1/m \approx 1/(3.0T)$;
3. The electric coupling strength, after averaging over different EQPs(quarks and gluons) with their respective Casimir, is roughly $< \alpha_s C > \approx 1$;
4. The particle density is roughly given, under the light that lattice results have shown the sQGP pressure and entropy to reach about 0.8 of Stefan-Boltzmann limit, by $n \approx 0.8(0.122 \times 2 \times 8 + 0.091 \times 2 \times 2 \times N_c \times N_f)T^3 \approx 4.2T^3$;
5. This density estimation leads to the Wigner-Seitz radius $a_{WS} = (\frac{3}{4\pi n})^{1/3} \approx 1/(2.6T) \approx 1.1r_0$;
6. We then get the time scale as the inverse of plasmon frequency $\tau_p = 1/\omega_p = (\frac{m}{4\pi n \alpha_s C})^{1/2} \approx 1/(4.2T)$;[2]
7. The entropy density is estimated from Stefan-Boltzmann limit as $s \approx 0.8 \times \frac{4\pi^2}{90}[2 \times 8 + (7/8) \times 2 \times 2 \times N_c \times N_f]T^3 \approx 16T^3$.

Now let's discuss the value of Γ. As already mentioned, the Γ given in our MD is the actual ratio of potential to kinetc energy, which is measured during the simulation. The usually quoted one, defined as $\tilde{\Gamma} = \frac{e^2}{a_{WS}(k_B T)}$, could be considered as a pre-determined 'superficial Gamma'. Unfortunately it is not clear how to estimate the actual Gamma Γ of sQGP while the superficial Gamma $\tilde{\Gamma}$ is obtainable for sQGP, which is $\tilde{\Gamma} \approx 2.6 < \alpha_s C > \approx 2.6$. So we should try to figure out the superficial Gamma in our MD and map the results accordingly. The two are different though, they are monotonously related to each other, namely when one is large(small) so is the other. Since our MD has been done with $n\lambda^3 = 0.17$, the $(a_{WS})_{MD} \approx 1.12\lambda$ which means in our MD $\tilde{\Gamma} = 0.89/T$, which after combination with (3.6) will give us the conversion formula between the two Gamma's. Similar conversion relation could also be obtained for cQGP in [23] from their Fig.8 though in their case they use superficial Gamma as basic parameter and measure potential energy from simulation.

With all the above ingredients we are at place to do the mapping for interesting transport coefficients D and η between our MD systems and the sQGP. The mapping is a two-way business: one may map the experimentally suggested values back into corresponding MD numbers, as is done and shown in

[2]This τ_p has subtle difference in time scale used in our MD, namely the MD time unit τ is related to inverse of plasmon frequency by $\tau = \tau_p \times (4\pi n\lambda^3)^{1/2} \approx 1.46\tau_p$ which should be taken into account for mapping.

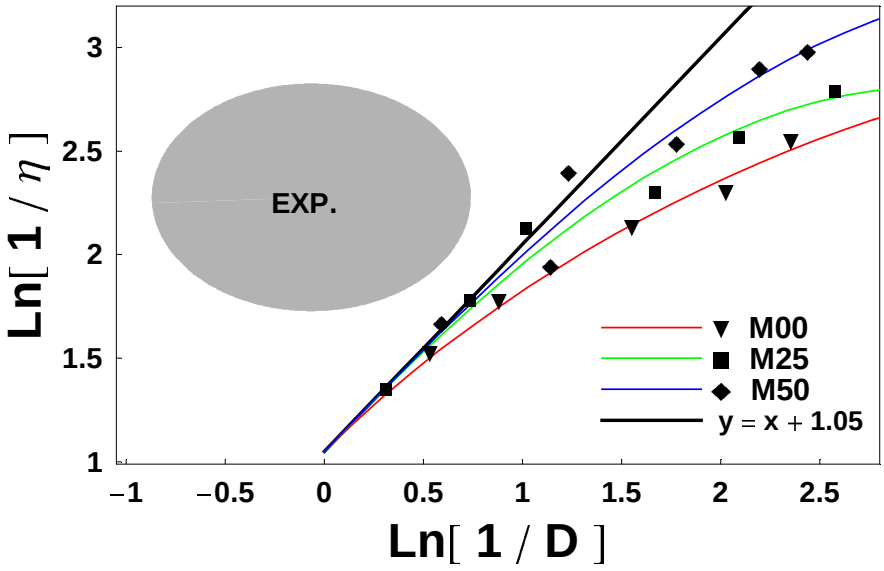

Figure 4.1: Plots of $Log[1/\eta]$ v.s. $Log[1/D]$ for three different plasmas. The shaded region is mapped back from experimental values, see text.

Fig.4.1; or one can use the MD-obtained relations to predict the corresponding relations of sQGP after conversion of units, as is shown in Fig.4.2 and discussed in the summary part. Here let's focus on MD systems in Fig.4.1 where a $Log[1/\eta]$ v.s. $Log[1/D]$ [3] is plotted: data points for all three plasmas fall on a universal unit-slope straight line on the left lower part, indicating a small Γ gas limit with diffusion and viscosity both proportional to mean free path; all three curves soon deviate from gas limit at larger Γ (strong coupling) and become flat in the liquid region; the shaded oval is obtained by mapping back the following experimental values: $\eta/s \approx 0.1-0.3$, $2\pi TD \approx 1-5$, which is clearly not close to gas region but near the liquid region, especially the one of the M50 curve. More about comparison will be given in the next subsection.

[3]The reasons to plot η and D in this way are: 1) from right lower corner to the upper left corner we go from weakly coupled (small Γ) to strongly coupled (large Γ) regime; 2) a weakly interacting gas will show a linear behavior on this plot which will be easy to distinguish, while deviation from such behavior will signal the emerging liquid regime.

4.1.2 A Transport Summary for sQGP

Now we would like to compare our MD predictions of shear viscosity and diffusion constant for sQGP with the results extracted from the RHIC experimental data. Experimentally the shear viscosity could be extracted by fitting viscous hydrodynamical calculation (with shear viscosity as a given input) to the measured v_2 spectra (see e.g. [16]), while information about diffusion could be extracted by fitting the hydro+Langevin (with diffusion as a given input) simulations with measured heavy quark R_{AA} and v_2 (see e.g. [60]). We want also to compare our results with the predictions from calculations using the AdS/CFT correspondence. AdS/CFT provides a unique way of doing non-perturbative calculations in a particular gauge theory, and the application of AdS/CFT for RHIC-motivated calculations has recently become very popular. All the results are summarized in Fig.4.2, as a log-log plot of properly normalized dimensionless (heavy quark) diffusion constant and viscosity.

The dashed curve in the left lower corner is for $\mathcal{N}$=4 SUSY YM theory in weak coupling, where viscosity is from [61] and diffusion constant from[62]. The curve has a slope of one on this plot, as in weak coupling both quantities are proportional to the same mean free path. As one can easily see, weak coupling results are quite far from empirical data from RHIC, shown by a gray oval in the right upper corner. Viscosity estimates follow from deviations of the elliptic flow at large p_t from hydro predictions [16], and diffusion constants are estimated from R_{AA} and v_2 of charm [60].

The curve for strong-coupling AdS/CFT results (viscosity according to [63] with $O(\lambda^{-3/2})$ correction, diffusion constant from [56]), shown by upper dashed line, is on the other hand going right through the empirical region. At infinite coupling this curve reaches $s/\eta = 4\pi$ which is conjectured to be the ever possible upper bound.

Our results – three solid lines on the right – correspond to our calculations with different electric/magnetic charges' ratios. They are very close to the empirical region, especially the version with equal mixture of the two types of charges.

Let us end with a warning, that the empirical data, the mapping from classical system to sQGP and the relation between QCD and the $\mathcal{N}$ =4 SUSY YM used in AdS/CFT will only become quantitative with time: this figure is just the first attempt to get together all three ingredients of the broad picture.

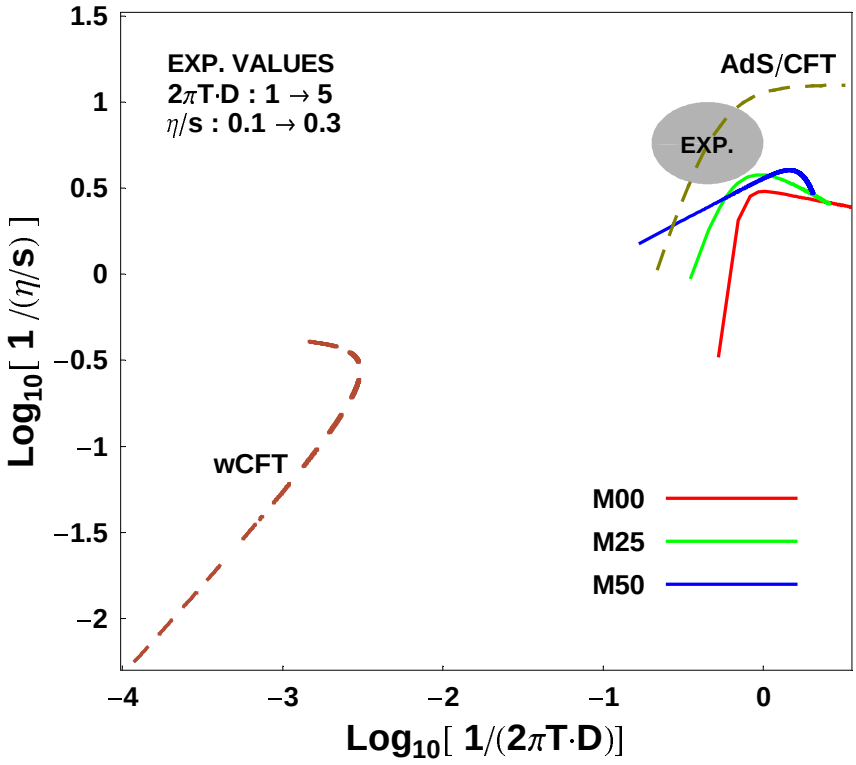

Figure 4.2: Plots of $Log[1/(\eta/s)]$ v.s. $Log[1/(2\pi TD)]$ including results from our MD simulations, the Ads/CFT calculations, the weakly coupled CFT calculations, as compared with experimental values, see text.

4.2 Microscopic Origin for the "Good Liquid"

The results in the previous section we showed that by maximally mixing electric/magnetic charges (i.e. our M50 plasma as compared with the M00 and M25) one achieves the best liquid behavior with lower viscosity and smaller diffusion, which indicate that the effective mean free path (if one wants to use such term) of the constituent particles is the shortest.

One may ask about the microscopic origin of such transport properties in our mixture plasma. As among the three plasmas the only difference comes from the E/M ratio, the Lorentz force between the two types of particles is most likely the microscopic origin. We suggest an explanation based on the "magnetic bottle" effect which was originally invented by G.Budker in 1950's and routinely used in confined plasma fusion experiments. The essence of this effect is that electrons will be bounced back from the surrounding strong magnetic field by Lorentz force when they try to exit the confining zone. In our study of single monopole motion in Chapter 2, we already saw the dual effect happening. In particular we demonstrated by the dipole example that the monopole is "forced" by the Lorentz force to collide head-on with the standing charges.

Coming to the mixture plasma with electric/magnetic charges, we found that each charge can be trapped for long time bouncing between the surrounding *charges of the other kind*. As as the fields are always becoming stronger and stronger close to the charges, the Lorentz force leads to curling of the trajectory with decreasing radius, forcing charges and monopoles collide more often than in the plasma made of only one type of particles, thus explaining the transport properties of the "good liquid".

Below we use a "Gedanken experiment" to further elucidate such effect as the microscopic origin for the "good liquid".

4.2.1 Monopole Motion in the Field of a "Grain of Salt"

We consider an idealized situation: a monopole is put at the center of a "grain of salt" which has eight static electric charges (with alternating signs) sitting at the corners, and then the monopole gets a random "kick" and blasts off with random direction and magnitude of initial velocity, see Fig.4.3 upper panel. We can repeat this "Gedanken experiment" as many times as we want, and what we are interested to learn will be: 1) what would the trajectory (as determined by classical equation of motion) be looking like; 2) how long it will typically take for the monopole to escape to the outside of the cube.

Naively, one may suspect in most cases the monopole will simply head toward one of the surfaces and escape the cube with its trajectory being slightly

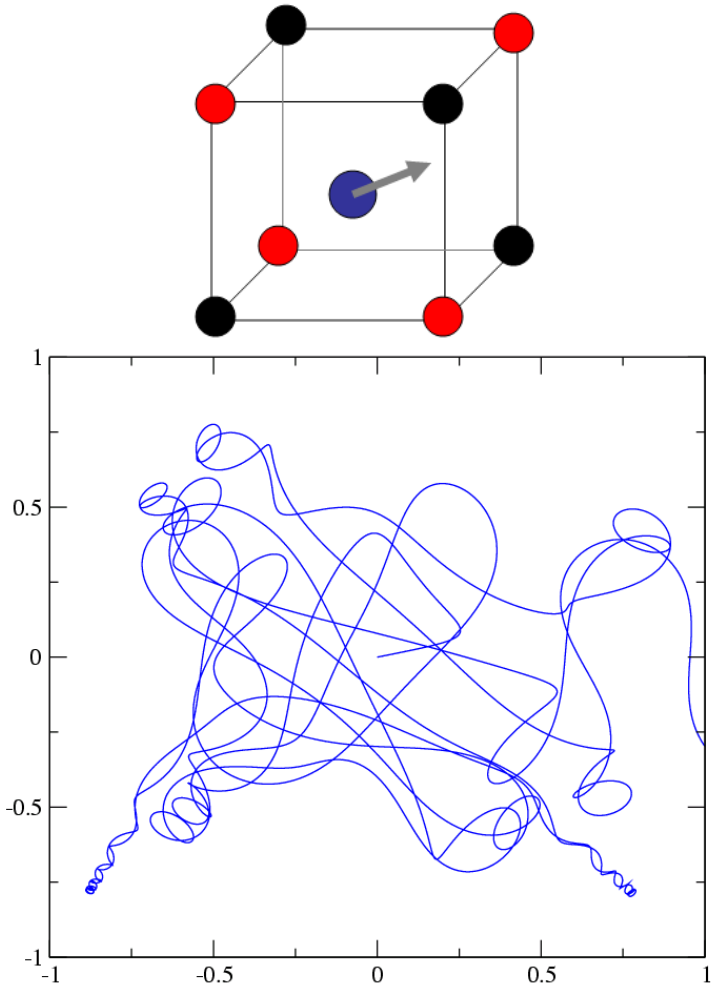

Figure 4.3: (upper) The Gedanken experiment setup: a monopole blasts off with randomly given initial velocity from the center of a cube with eight electric charges (with alternating signs) sitting at the corners, like a "grain of salt"; (lower) An example of the monopole trajectory (projected on 2D coordinates x-y), which starts from the center and exits the cube near one of the right-side face center, with several visible Poincare-cone like structures near the corners.

bent due to possible collision with the nearest electric charge. It turns out most of the trajectories are highly complicated: a typical example is shown in Fig.4.3 lower panel. The trajectory shows rather nontrivial features. First of all, the monopole experiences far more than one collisions before it finally finds the "door" out, as is clear from the multiply-folded trajectories; second, the collisions are very strong, this could be seen from the facts that the monopoles are often completely bounced back instead of only being mildly refracted, and many parts of the trajectories are highly curled within small space; finally it is impossible to escape our eyes that there are several visible Poincare-cone like structures near the corners (where the electric charges are), and those are precisely where the strong collisions happen. From these observations, we may conclude that the monopole is, instead of encountering the electric charges at corners by chance, rather being forced to rotate on the Poincare-cone, blast all the way to the charge and then be bounced back, only to be forced toward another corner for the next strong collision. If we replace the monopole with an electric charge and do the same experiment, no such nontrivial phenomenon happens. The Lorentz force here provides a unique way of enhancing the collision rates and trapping the monopole for long time (not permanent though): thus we may call it a Lorentz trapping effect.

One may ask how sensitive the above phenomenon is to the direction and magnitude of the initial velocity of the monopole. The direction actually does not matter at all, while the magnitude of the velocity does matter: basically the smaller the velocity is, the longer and more complicated the trajectory will be. We will quantitatively address this issue in the next subsection. In the rest of this subsection we answer another related question: is such Lorentz trapping effect also present in the quantum mechanical context? The answer is positive, see below.

The Quantum Effective Potential

Similarly to the dipole problem we studied in Section 2.2.2., we can write down the quantum mechanical Hamiltonian (2.10) for the monopole in the external electric field of the eight charges sitting at $(\pm a, \pm a, \pm a)$. The vector potential $\boldsymbol{A}$ can be obtained by considering the eight charges as four pairs of electric dipoles and superposing up their respective $\boldsymbol{A}_{dipole}$ with the latter given by (2.13) after proper shift of the dipole center coordinates. Then from the Schroedinger equation one can read off the quantum effective potential. The main part of it is $V_{eff}(x, y, z) \sim g^2 \boldsymbol{A}^2 / 2Mc^2$. In Fig.4.4 we show the effective potential on the x-y plane at three values of z, i.e. $V_e ff(x, y, z =$

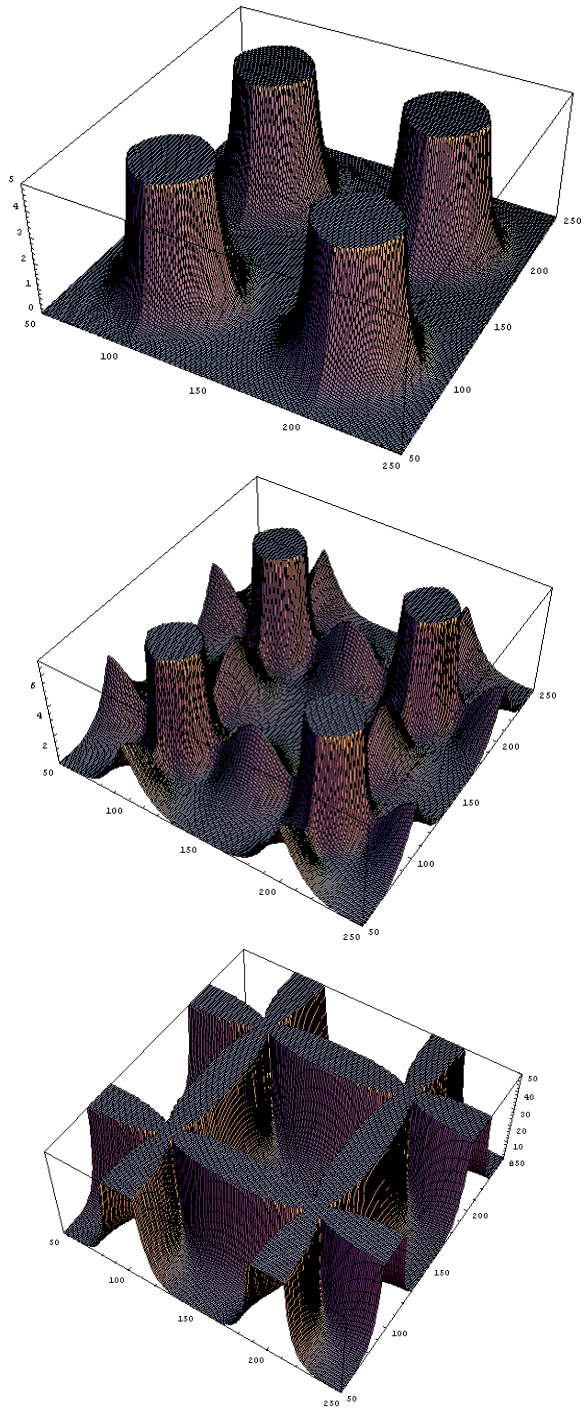

Figure 4.4: The quantum effective potential for a monopole inside the cube of electric charges on the x-y plain at $z = 0, a/2, a$ from top down, see text.

0),$V_eff(x, y, z = a/2)$ and $V_eff(x, y, z = a)$. [4] Geometrically these are three planes (parallel to the x-y surface) across the center, halfway from the center to the surface, and right on the surface. For $z = 0$, the potential grows to be quite high when approaching the four corners (the four edges of the 3D cube), with only the zones near the four surface centers having flat valley; going upward to $z = a/2$ the potential becomes stronger and stronger with all four sides becoming high barriers; finally when going to $z = a$, the potential really makes a quantum "cage" for the monopole such that it has vanishing probability to penetrate the four "thick walls" surrounding it. The only thin tunnels for the monopole to escape with ease are those near-face-center zones where the potential is flat. So we see that in the quantum context, the Lorentz-type coupling produces effective potential that is capable of trapping the monopole while not really binding it permanently, which is a quantum version of the Lorentz trapping effect we uncovered classically in the preceding part.

4.2.2 Lorentz Trapping Effect Makes the Good Liquid

In the present subsection, we will quantify the Lorentz trapping effect and show how it may ultimately affect the transport properties of a mixture plasma with both electric and magnetic charges.

Coming to back to our classical "Gedanken" experiment, for each repeated trial, we register the total trajectory length $L_{Esc.}$ before it escapes the cube, or equivalently the total trapping time $\tau_{Esc.} \equiv L_{Esc.}/v_0$ before its escaping. As we already mentioned, the effect is sensitive to the monopole's initial velocity magnitude v_0. So we choose several different values of v_0, and for each v_0 we repeat the experiment with random initial directions for 10^5 times and obtain a histogram for various $L_{Esc.}/a$: the results are shown in Fig.4.5 for $v_0 = 0.1, 0.3, 0.5$ respectively.[5] The plots show that $L_{Esc.}$ becomes much flatter, i.e. with more probability to be trapped with longer time, with smaller v_0. The explanation is simple: monopole with smaller velocity will be more easily curled (under fixed electric field strength) with smaller Larmor circle, thus more often be forced to collide with the charges. As a comparison we also did the same experiment for an electric charge released at the center with those values of v_0, yet it turns out the electric charges almost always exit immediately and never get bounced back, see the three indistinguishable curves on top of each other close to the left axis. So this study demonstrates that Lorentz force, the unique mutual interaction between electric and magnetic charges only in

[4]Note that the potential has cyclic symmetry of x, y, z as well as various mirror symmetries so the three selected planes already tell a lot info about the potential

[5]The unit system is set in similar way as in the MD simulation.

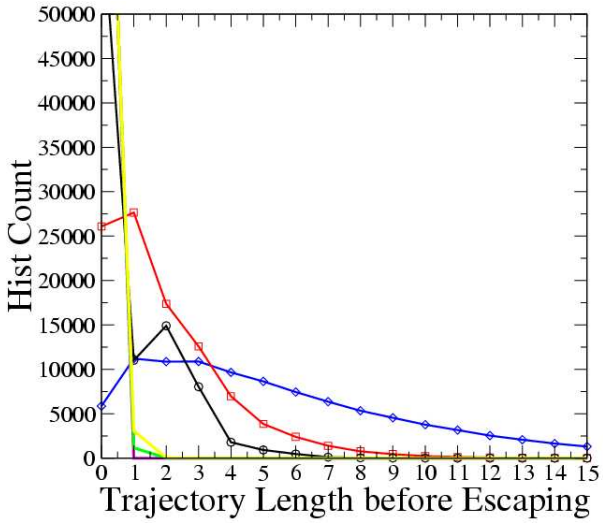

Figure 4.5: Histogram for total trajectory length (in unit of a) before escaping, the curves across circle(black), box(read) and diamond(blue) data points are for $v_0 = 0.5, 0.3, 0.1$ respectively, while the other three curves (almost indistinguishable) are results for electric charges with the same values of v_0.

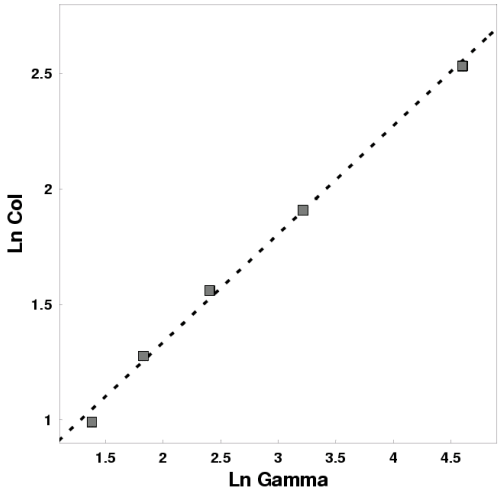

Figure 4.6: The collision number C as a function of plasma parameter Γ on a log-log plot, see text.

a mixture plasma, does provide a quite efficient mechanism that very much enhances collision rates and traps particles locally for time scale much longer than normal time scale for microscopic motion, i.e. $\tau_{Esc.} >> a/v_0$.

We can define an average effective collision number for the monopole with each given v_0 by averaging out the histogram for $L_{Esc.}$: $C \equiv < L_{Esc.}(v_0)/(2a) >$. Further more the kinetic energy of the monopole is $KE \propto v_0^2$. If we "pretend" the monopole is taken as a representative of a plasma with parameter $\Gamma = PE/KE$, then $v_0 \propto 1/\Gamma^{1/2}$. In this way we schematically obtain a plot showing how the so-defined C changes with Γ, see Fig.4.6. It shows a linear relation in the Log-Log plot, which can be nicely fitted by $C \propto \Gamma^{0.47}$. For such a monopole, its mean free path $L_{MFP} \propto 1/C \propto 1/\Gamma^{0.47}$. One may image that there is a whole crystal with periodically repeating electric cube and the monopole is jumping from the original cube to the neighboring cubes and eventually diffuses to far away distance. In a hand-waving manner we may argue that the diffusion constant for such a monopole would be $D \propto L_{MFP} \propto 1/\Gamma^{0.47}$ which (probably by chance) is close to the power law both obtained from our MD and from the AdS/CFT calculation.

Finally we extend the above argument into a dynamical mixture plasma: in such a plasma, each electric charges are surrounded by neighboring monopoles and vice versa, so by the Lorentz trapping effect they could be spatially interlocked for certain time that is much longer than microscopic motion time scale, but eventually on the even longer time scale they could diffuse away from the original places. This microscopic picture explains, as we believe, why the maximally mixed M50 plasma is such a good liquid.

4.3 Monopole-Anti-Monopole Equal-Time Spatial Correlation Functions

In this section, we study another important property that can also distinguish Coulomb systems in gaseous, liquid or solid regimes, namely the particle-particle equal-time spatial correlation functions. It is defined as a function of the distance r between two species of particles:

$$G_{ab}(r) \equiv \frac{< \sum_{i=1,N_a} \sum_{j=1,N_b} \delta(|\boldsymbol{r}_i^a - \boldsymbol{r}_j^b| - r) >}{N_a N_b 4\pi r^2/V} \tag{4.1}$$

where a, b denotes the two species of particles with total numbers N_a, N_b in a volume V.

It is well known that what makes a liquid so difficult to study as compared

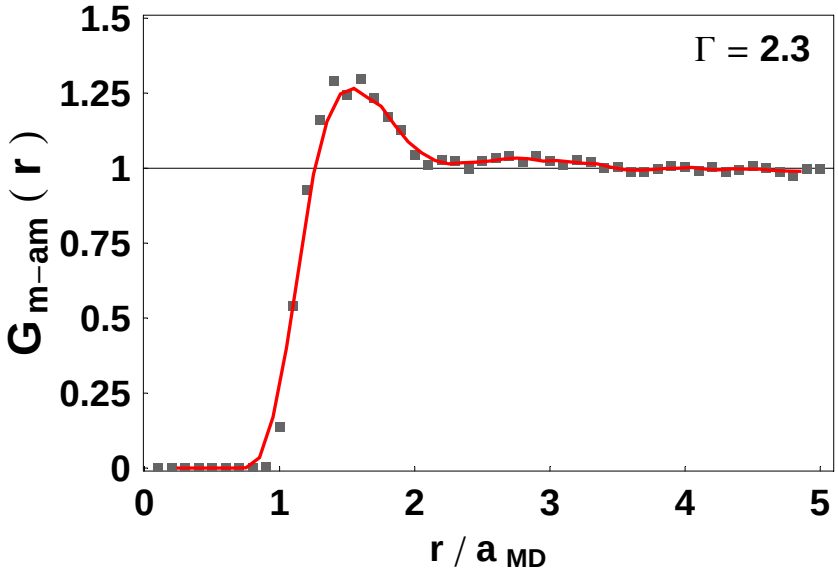

Figure 4.7: Monopole-anti-monopole equal-time spatial correlation function from MD simulations. The gray boxes are data points and the red curve is statistically smoothened.

with a gas or solid is that it can *not* be statistically described by any single particle (or quasi-particle, say phonon or other collective excitations in solid) distribution. This failure of Boltzmann-type description for liquid is precisely encoded in its very strong two-particle correlation functions.

Since we are particularly interested in the magnetic component of sQGP, a very instructive diagnosis for that purpose would be the $G_{M\bar{M}}$, the monopole-anti-monopole equal-time spatial correlation function, which will tell how strongly the monopoles are correlated. Below we present results for $G_{M\bar{M}}$ from our MD simulations and from recent accurate lattice data as well.

MD Results

The MD result is shown in Fig.4.7, for the 50%-50% electric-magnetic symmetric plasma with $\Gamma = 2.3$. We choose this example because it has the closest properties to the sQGP (as probed by RHIC) according to the transport summary presented in the first section. The plot features a considerable nearest-neighbor peak, reaching around 1.25, with hints to small secondary correlations: a typical *liquid* behavior. The same correlation function for a weakly coupled gas would have a very small peak only barely above 1, while

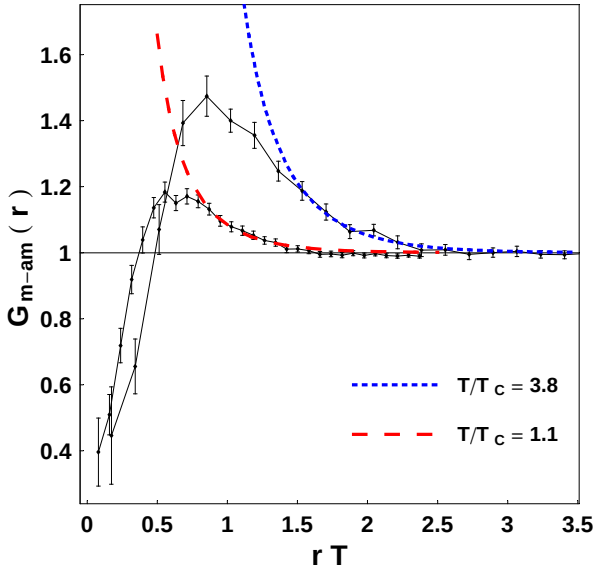

Figure 4.8: Monopole-anti-monopole equal-time spatial correlation function: the points are lattice data from [Nucl. Phys. B799:241-254, 2008], the dashed lines are our fits.

a solid will have visible multiple peaks/valleys. The reader shall recall that we do *not* consider here the usual Coulomb plasma due to presence of equal number of electric particles in our mixture – with which monopoles interacts with a strong Lorentz force, leading to very complicated motion – so the result is far from trivial.

Lattice Data

Lattice studies of monopoles have a long history which we would not even attempt to summarize here. We will also not discuss here either the properties of these monopoles (masses) or their interaction with other main players in sQGP – gluonic quasiparticles and the Polyakov loop or "Higgs field" A_0. We will focus entirely on one aspect of these data, related with monopole-anti-monopole equal-time spatial correlation function (4.1) just discussed. Those have been derived on lattice recently by D'Alessandro and D'Elia[64], for SU(2) pure gauge theory. Fig.4.8 shows two sets of their data corresponding to the smallest and highest temperatures, $T = 1.1T_c$ and $T = 3.8T_c$. Both shapes are very similar to the one in our MD studies shown above, in their shapes and in the magnitude of the peaks. These data, together with our MD results, provide firm and direct evidences that the magnetic component of sQGP is

indeed a liquid.

Another qualitative feature apparent from this plot is that the correlation gets *stronger* at the *higher* T, confirming our expectation that the magnetic component of sQGP gets stronger coupled at high T, *oppositely* to the electric component. This important point will be discussed in the next section.

4.4 The Coupling of the Magnetic Component

In this section, we focus on one of the main subjects of our magnetic scenario – the monopole mutual interactions. Before coming to that, we'd like to very briefly repeat some of the relevant theoretical issues already discussed in the Introduction. The most important basis for pursuing a magnetic description comes from the famous Dirac condition, demanding basically that when one of the two couplings – electric and magnetic – may be small, the other must necessarily be large. At the level of quantum field theory the Dirac condition elevates into a requirement that the electric/magnetic couplings must run in the *opposite directions*.

Specifically for the QGP system, we know what happens to the electric component: at *high* T it can be described perturbatively, with e.g. small quark and gluon effective masses $M/T \sim \sqrt{\alpha_{electric}} << 1$; as T goes down and one approaches the deconfinement transition $T \to T_c$, the electrically charged particles – quarks and gluons – are getting heavier and more strongly coupled, as shown by lattice data as well as RHIC results. To summarize, from *high* to *low* T the electric coupling runs from small to large values while the electric particles change from being light and abundant to being heavy and statistically irrelevant.

For the magnetic component, we also know that at *high* T we know the monopoles in this case are heavy composites which play a minor role, although they are strongly interacting and form an interesting sub-sector in which perturbative analysis is impossible. However at this point one may ask what happens with monopoles: as $T \to T_c$ the same logic suggests that they must become lighter and more important. At some point their masses (and roles) get comparable to that of the electric objects, after which the tables are turned and their fortune reversed.

Here are the two questions we already proposed in the Introduction part: (i) Is there evidence that the magnetic coupling does run in the opposite direction to that of the electric coupling? (ii) How small does the magnetic coupling become at $T \to T_c$, and is a perturbative description of magnetic plasma possible? As the reader will see, we will answer "yes" to the first and

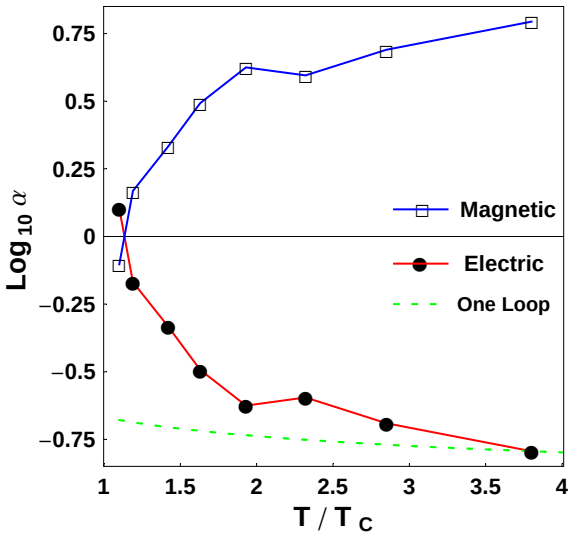

Figure 4.9: Open squares show the temperature dependence (in T_c units) of the magnetic coupling constant α_M from the fit to lattice data. Closed circles are their inverse, the corresponding electric coupling from the Dirac condition, together with an asymptotic freedom (dashed) curve (see text).

"no" to the second question.

The Monopole-Anti-Monopole Coupling

To get a more quantitative measure of the monopole-anti-monopole mutual interaction, we have fitted their equal-time spatial correlation function (shown in Fig.4.8) by the Debye formula in the region where deviation from 1 is small

$$G_{M\bar{M}}(r) \sim exp\left[\frac{\alpha_M e^{-r/R_d}}{rT}\right] \tag{4.2}$$

in which α_M is the magnetic coupling, and the R_d is magnetic screening radius. See the dashed curves in Fig.4.8. Some details about the fitting at each temperature: we exclude the last few points that are very close to but lower than 1 as the fitting formula approaches 1 only from above; the rule to determine how many points from large r toward the peaks to be included is to make $\chi^2/d.o.f$ as close to 1 as possible; the $\chi^2/d.o.f$'s for the eight T's are $1.16, 1.96, 1.17, 0.46, 0.82, 0.16, 1.16, 1.23$ respectively.

The resulting monopole-anti-monopole coupling from the fitting for all available temperatures is shown in Fig.4.9: as expected it is getting weaker at

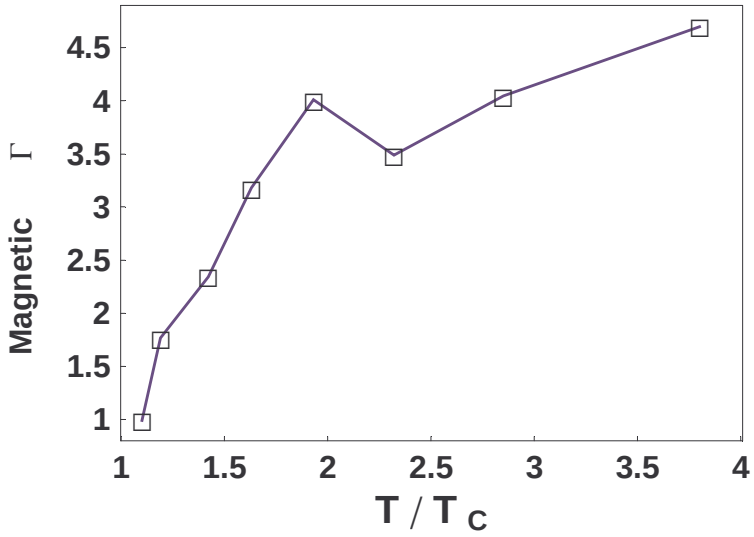

Figure 4.10: Effective magnetic plasma parameter Γ_M at various temperatures.

low T and stronger at high T. Inverting these values (because of the Dirac condition (**??**)) one gets the respective electric couplings, which we compare to the dashed green curve corresponding to the pure gauge SU(2) one-loop asymptotic freedom expression $\alpha_E \approx \frac{2\pi}{(22/3)Ln[C*(T/T_c)]}$ with the coefficient $C = 54$ determined from the last point at $T = 3.8T_c$. The one-loop running becomes much slower as T decreases, which is normal and shall be cured by higher order loops and more importantly by non-perturbative corrections such as instanton, see [65] for more discussions.

The Plasma Parameter for the Magnetic Component

In the many-body setting, two-body interaction alone is not sufficient to determine how strongly the whole system is coupled, e.g. in the gas, liquid or solid regime. For that purpose one should examine the the key classical Coulomb plasma parameter Γ defined by

$$\Gamma \equiv \frac{\alpha_C \,/\, (\frac{3}{4\pi n})^{1/3}}{T} \tag{4.3}$$

with α_C the Coulomb coupling between charges, $Q = E$ or M, and n the density of the corresponding charges. Again tt roughly means the ratio of the potential energy (interaction) to the thermal kinetic energy; thus a weakly coupled plasma has $\Gamma << 1$. Plasmas with $\Gamma > 1$ are known as strongly cou-

pled, and for $\Gamma < few10$ it is in the liquid regime, for $\Gamma > \Gamma_c \sim 100$ it is solid, with less precisely defined "glassy" regime in between. The electric parameter in sQGP is believed to be $\Gamma_E \sim 3$ at $T = (1-2)T_c$ [23], so it corresponds to a liquid. The value of the magnetic component's plasma parameter Γ_M is the subject here.

In Fig.4.10 we combine the data on the magnetic coupling and the monopole density from the same lattice work [64] to get the dimensionless magnetic plasma parameter (4.3) in the studied temperature range $T \approx 1 - 4T_c$. We use a formula $n(T)/T^3 = 0.557/[Ln(2.69 * T/T_c)]^2$ from [64] which was found to nicely fit the monopole density data. As one can see, magnetic component of QGP never gets to be a weakly coupled gas, as $\Gamma_M > 1$ at all T even close to T_c. On the other hand, even at the highest T the value of Γ_M does not reach large values > 10 at which liquids are known to become glass-like and viscosity starts growing. So the magnetic component not only is a liquid, but also a good liquid in $1 - 4T_c$!

Chapter 5

Electric $\bar{Q}Q$ Potentials at $T \approx T_C$ and the Magnetic Component of sQGP

In this Chapter, we show one important application of the proposed magnetic scenario for sQGP: to explain the nontrival T-dependence and the unusual linear rising of the static $\bar{Q}Q$ potentials found on the lattice, especially at $T \approx T_c$. The key idea is that the very dense magnetic liquid at $T \approx T_c$ from the vaporizing monopole condensate in the dual superconductor vacuum can actually create a postconfinement regime, and in particular is capable of holding electric flux tube between static $\bar{Q}Q$ pair, thus leading to linear potential. In the first section we extend our discussion on this key idea, then in the next two sections we develop a finite-separation flux bag model and explain the potential based on the magnetic component of sQGP. In the last section we study a separate, idealized question related to the mechanical stability of an infinitely long electric flux tube in a magnetic plasma, deriving a condition for flux tube formation. [1]

5.1 A Discussion on the Potential Problem

5.1.1 Overview

The interaction potential between heavy quark and anti-quark is a traditional observable, by means of which quark confinement in Non-Abelian gauge theories was established. It was originally inferred from heavy meson spectrum

[1] The works in the present chapter are based on [47][66].

and Regge trajectories, and then studied in great detail numerically, through Wilson/Polyakov lines using lattice gauge theories, for review see e.g. [67][68]. Its vacuum (T=0) form is well known is usually represented as a sum of a Coulomb part $V \sim 1/r$, dominant at small distances, and a linear part $V = \sigma r$ dominant at large r. The latter, related with existence of electric flux tubes, is a manifestation of quark confinement. The string tension in the vacuum ($T = 0$) has been consistently determined by different methods to be about

$$\sigma_{vac} \approx (426 MeV)^2 \approx 0.92\, GeV/fm \tag{5.1}$$

With current RHIC and future LHC experimental programs exploring excited hadronic matter and quark-gluon plasma (QGP) at increasing T, lattice studies of the static $\bar{Q}Q$ potential have been extended to finite T, see e.g. results of the Bielefeld-BNL group[69][70][71][72][73] [74][75][76]. At the critical temperature $T = T_c$ disappearance of the linear term in the corresponding free energy $F(T, r)$ – the string tension σ_F – is the signal of deconfinement.

The internal/potential energy and entropy associated with the static $\bar{Q}Q$ pair are defined via

$$V(T, r) = F(T, r) - TdF/dT = F(T, r) + TS(T, r) \tag{5.2}$$

Remarkable features of these results (see e.g. Fig.1-4 in [76] and also Fig.5.1(a)) include:
(i) nonzero tension σ_V (the coefficient of the linear part of $V(T, r)$ as function of r at given T) till about $T = 1.3T_c$, with the peak values at T_c about 5 times (!) the vacuum tension σ_{vac}, with similar behavior in entropy while cancelling in the free energy;
(ii) Finite values of the potentials at large distances reach very large magnitude, $V(T, \infty) \sim 4\, GeV$ at T_c. The corresponding entropy $S(T_c, \infty) \approx 20$ implies huge number of states involved, $\sim exp(20)$.

The consequence of these features for survival of heavy quark mesons at finite T are hotly debated. Quasiparticle bound states in the deconfined plasma were in particular discussed in [21][22]. Baryonic states seem to be needed to understand baryonic susceptibilities[77][46]. These potentials are of course also important in many-body aspects of QGP: in particular, they enter the so-called plasma parameter Γ, defined as average potential energy over the average kinetic energy. Its value in sQGP has been estimated to be above one (about 3) leading to the important conclusion that QGP at RHIC is a liquid (see for example [23][49]), in qualitative agreement with the transport properties observed at RHIC. These findings, together with many other theoretic and experimental results, led to the paradigm shift to view QGP in 1-2T_c region

as a strongly coupled many body system, now referred to as sQGP[11][13].

The origin of large energy/entropy associated with the static $\bar{Q}Q$ pair near T_c remains mysterious, despite early attempts to explain it[78][79][**?**]. In this paper we will provide our explanation in the framework of the *magnetic scenario of sQGP* [49] featuring the "struggle" for dominance between the electric and magnetic sector, fuelled by the opposite running of electric and magnetic coupling constants[59], basically confirmed by several subsequent lattice works, see [80][81][82][64]. A novel plasma made of a mixture of electric and magnetic quasiparticles has been shown [49] to explain small viscosity and diffusion constant – "the perfect liquid" behavior observed at RHIC. Brief summaries of the most recent developments in the magnetic scenario can be found in [14][83].

More specifically, in this paper we focus on the "tensions" (coefficients of the linear term in distance) in the free and potential energies. Like in our previous work [47], we relate them with electric flux tubes. We further relate those tensions with both the magnetic supercurrent (induced by condensed monopoles) and the usual current (induced by "normal" monopole liquid). This will allow us to extract very important information about the finite-T QCD medium, such as "normal" monopole density, and compare it with lattice observations.

We also provide new analytic solution for "elliptic bags" which allows to get the potentials correctly interpolating between Coulomb and linear behavior. We however leave discussion of "screening" behavior at large distances to further studies.

This Chapter is structured as follows. In Section 5.2 we will develop an analytic "flux bag" model of two static charges by solving the Laplace equation for electric field. The model will then be used in section 5.3 to determine the free and potential energies and relate the extracted σ_F and σ_V with the condensate energy density and the thermal monopole density respectively.

5.1.2 Free v.s. Potential Energy and Slow v.s. Fast Probes

Let's start by examining the physical difference between the free energy and the potential energy. We already introduced effective string tensions $\sigma_F(T)$ and $\sigma_V(T)$ as the slopes of linear parts in $F(T,r)$ and $V(T,r)$ respectively, and emphasized their quite different T-dependencies shown in Fig.5.1(a). While σ_F vanishes at $T > T_c$, σ_V survives to at least $1.3T_c$. While σ_F monotonously decreases with T, σ_V peaks at T_c to a maximal value of 5 times the vacuum string tension σ_{vac}. What is the difference in the meaning of F and V, and

why do they have such T-dependence?

It was emphasized in [21] that free and potential energies correspond to slow and fast motion of the charges, respectively. Let us explain this idea in more detail.

To understand why it is so one should consider "level crossing" phenomena, occurring while the separation of charges changes. Suppose a pair of static charges (held by external "hands") are moving in thermal medium, so that their separation $L(t)$ is changing with a certain speed $v = \dot{L}$. The energies of multiple states of the media, defined at fixed L, are crossing each other, and at each level crossing there is a certain probability to jump from one level to another. In thermodynamical context this process leads to entropy/heat generation, but the issue exist in pure quantum mechanical context at zero T as well. Perhaps the oldest is the so called Landau-Zener problem [84] of electron dynamics, following vibrational motion of two nucleus in a diatomic molecule. Specific electron quantum states $\psi_n(L)$ are defined at fixed L with the energies $E_n(L)$. The issue is the probability of the transition during crossings of two levels, e.g. with $E_1(L) \approx \sigma_1 L + C_1$ and $E_2(L) \approx \sigma_2 L + C_2$. When the two nuclei approach the crossing adiabatically slowly $v = \dot{L} \to 0$, the electrons always proceed from one state to another selecting the *lowest* state at any L. More quantitatively, Landau-Zener showed that the probability to remain in the original state is exponentially small at small v

$$P_{remain} = exp\Big[- \frac{2\pi |H_{12}|^2}{v|\sigma_1 - \sigma_2|} \Big] \tag{5.3}$$

where H_{12} is the non-diagonal transition matrix element of the Hamiltonian.

In our problem the adiabatic limit corresponds to the free energy $F(T, L)$ measured on the lattice, with static quarks. The "potential energy" $V(T, L)$ is different from it by subtracting the entropy term: it means that no entropy is generated. This corresponds to motion in which possible transitions from the original pure state into multiple other states via level crossing do *not* occur: thus we identify it with the fast (large v) limit.

The positivity of the entropy implies that $V > F$ always. Thus a state created by a fast probe, with energy V, can relax in time into the equilibrium configuration with the free energy F.

Which potential should then be used, e.g. in charmonium (or other bound states) problem? From the discussions above, it is clear that this depends on the relation between pertinent time scales involved, as the names "slow/fast probe" themselves indicate: the "probe time" $\tau_{sep.}$ and the medium relaxation time $\tau_{rel.}$. Suppose we separate the charges to L in a time $\tau_{sep.}$, and approximately identify the Landau-Zener parameters as: $|H_{12}| \approx 1/\tau_{rel.}$ ($\tau_{rel.}$

the medium relaxation time), $v_{12} \approx L/\tau_{sep.}$, and $|\sigma_1 - \sigma_2| \approx |\sigma_F - \sigma_V|$. This leads to the criterion distinguishing the slow v.s. fast separation, i.e. $\tau_{sep.} >> \tau^2_{rel.}|\sigma_F - \sigma_V|L/2\pi$ v.s. $\tau_{sep.} << \tau^2_{rel.}|\sigma_F - \sigma_V|L/2\pi$. As an estimation if we takes $\tau_{rel.} \approx 1fm$, $|\sigma_F - \sigma_V| \approx 1 - 5GeV/fm$, and $L \approx 1fm$, then the critical separation time is $\tau^2_{rel.}|\sigma_F - \sigma_V|L/2\pi \approx 0.8 - 4.0fm$.

5.1.3 Stable and Metastable Flux Tubes

We now turn to the possible origin of the two potentials. The starting point is a "dual superconductor" picture of confinement introduced by t'Hooft-Mandelstam. In it some "magnetically charged" condensate expels the electric flux between $\bar{Q}Q$ into a flux tube. The vacuum string tension is thus identified with energy per unit length of the corresponding Abrikosov-Nielsen-Olesen (ANO) solution, for review and further references see e.g. [54][67][68][85][86]. The disappearance of σ_F at T_c is naturally identified with "melting" of the condensate: similar phenomena is known for the usual superconductor.

Now, where the tension σ_V comes from? The answer proposed in [49] relates it to "normal" monopole liquid, which also expels the electric flux. Specific condition for the persistence of the flux tubes in the plasma (deconfined) phase was further developed in [47], for infinitely long flux tubes. It has been found in that paper that "normal" monopoles are much less effective for this task, thus quite high density of them is required, to form the magnetic current strong enough to contain the electric flux. However there we have considered conditions of only mechanical stability of the flux tube, leaving the mechanism of its dynamical formation and decay for further works.

Now we propose a dynamical explanation of why large energy, growing approximately linearly with length, appears in a magnetic plasma when the two charges are separating with some finite speed v, see sketch of the setting in Fig.5.1(b). The answer lies in the Maxwell equations, which is convenient to cast in form of the *dual* Faraday's law, which relate the circulation of the magnetic field $\int \boldsymbol{B}\boldsymbol{d}\boldsymbol{l}$ over some contour with the change of electric flux through it. As electric charge moves through the loop, rotating magnetic field in monopole plasma leads to solenoidal magnetic current (a "magnetic coil"). In the confined phase $T < T_c$ this current, after relaxation, becomes the persistent supercurrent, remaining forever without losses: thus the free energy F has a linear term for $T < T_c$. In a deconfined plasma phase $T > T_c$ this is impossible, thus $\sigma_F = 0$: the solenoidal "magnetic coil" created in the fast process has only normal current, with losses, which eventually disappear. Yet it is still generated: thus $\sigma_V - \sigma_F$ is nonzero.

This means that monopoles can induce new mechanism of jet energy loss, as they are accelerated solenoidally by B field due to a fast moving electric jet,

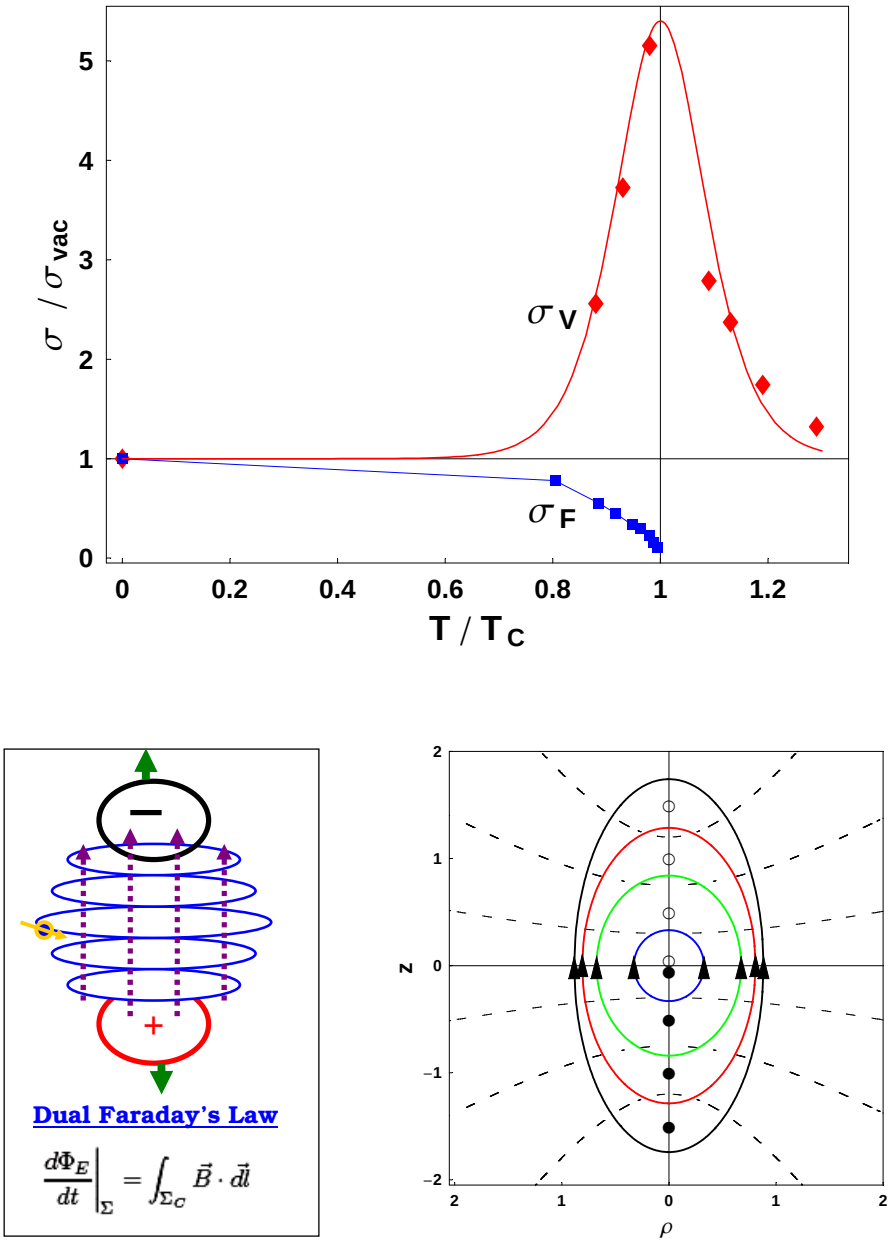

Figure 5.1: (a)(upper) Effective string tensions in the free energy $\sigma_F(T)$ and the potential energy $\sigma_V(T)$. (b)(lower left) Schematic demonstration of magnetic solenoidal by Dural Faraday's law, see text. (c)(lower right) The ellipsoidal shapes we use for solving the electric field equations, see Section.II for detailed explanations.

active mostly at $T \approx T_c$. While these monopoles are subsequently colliding with the bulk thermal matter, their energy becomes certain amount of heat TS, which with time is transferred away by heat conductivity. This possibly is the beginning of "conical flow" process suggested in [87].

Here it is important to emphasize different roles of the super-component and a normal-component: the former does not distinguish the slow/fast processes (as their $\tau_{rel.} \to 0$) thus not contribute to the splitting, while the latter have finite relaxation time and do feel the different processes, thus fully responsible for the splitting. In short, the σ_F tells us about the condensate only, while the difference $\sigma_V - \sigma_F$ tells us about the normal component. Bearing this in mind and looking at the non-trivial T-dependence of σ_F and σ_V in Fig.5.1(a), one has a picture of an **evolving magnetic medium**: with increasing T the monopole ensembles changes from a dense monopole condensate to equally dense *normal* component of thermally excited monopoles at $T \sim T_c$, which emerges out of the condensate and becomes dominant in $0.8 - 1.3T_c$, after which they start yielding to the regular electric quasiparticles (quarks) at large T.

5.2 Electric Field in the Ellipsoidal Bag

In this section we will solve the equation for electric field induced by two static charges separated by $L = 2a$ along $\hat{\mathbf{z}}$ axis ($\pm Q_e$ sitting at $\mp a\hat{z}$), with the special "tangent boundary condition" (T.B.C.) on the boundary surface Σ_B , i.e.

$$\nabla^2\Phi(\boldsymbol{r}) = Q_e[\delta^3(\boldsymbol{r} - a\hat{\mathbf{z}}) - \delta^3(\boldsymbol{r} + a\hat{\mathbf{z}})] \quad , \quad \nabla\Phi \cdot \hat{\mathbf{n}}_{\Sigma_B}|_{\Sigma_B} = 0 \tag{5.4}$$

The physical picture is an old idea known as the Bag Model used for hadrons [88] in the vacuum, now generalized to magnetic medium at finite temperature.

A simplification we use is that the boundary Σ_B is approximated by a rotational ellipsoid with the two charges at its focal points. This boundary shape can be specified by a single parameter ξ_B, the ellipticity. Such boundary Σ_B is very conveniently parameterized in terms of the parabolic coordinates system (ξ, η, ϕ), which we use: see the appended part at the end of this section for necessary formulae related to it. In Fig.5.1(c) we showed a few ellipsoidal shapes with parameters (from inside to outside) (L, ξ_B) to be $(0.1, 6.62)$,$(1, 1.68)$,$(2, 1.29)$,$(3, 1.16)$ respectively, the dashed lines indicate constant-η curves (for $L = 3$ case) with (from top to bottom) $\eta = 0.8, 0.5, 0.2, -0.2, -0.5, -0.8$, the solid/empty circles indicate the positions of

positive/negative charges, and the arrows indicate the tangent electric fields on the boundary.

We follow standard method in electrostatics, see for example [52]. First, we rewrite (5.4) in (ξ, η, ϕ) coordinates assuming $\Phi = \Phi(\xi, \eta)$ independent of angle ϕ

$$\begin{aligned} \frac{\partial}{\partial\xi}\Big[(\xi^2-1)\frac{\partial\Phi}{\partial\xi}\Big] + \frac{\partial}{\partial\eta}\Big[(1-\eta^2)\frac{\partial\Phi}{\partial\eta}\Big] &= \frac{Q_e\delta(\xi-1)}{\pi L}\Big[\delta(\eta-1)-\delta(\eta+1)\Big] \\ &= \sum_{\nu=1,3,5,\ldots} \frac{Q_e\delta(\xi-1)}{\pi L}(2\nu+1)P_\nu[\eta] \end{aligned} \tag{5.5}$$

The second step is by expanding the η-dependence in terms of Legendre functions $P_\nu[\eta]$ in the interval $\eta \in [-1, 1]$, in which the P_ν functions are orthogonal and complete. Similarly, we do the expansion $\Phi_{\xi,\eta} = \sum_{\nu=1,3,5,\ldots} \frac{Q_e f_\nu[\xi]}{\pi L}(2\nu + 1)P_\nu[\eta]$, thus simplifying the equation to be the equations for $f_\nu[\xi]$ in a domain $\xi \in (1, \infty)$:

$$\frac{d}{d\xi}\Big[(1-\xi^2)\frac{df_\nu}{d\xi}\Big] + \nu(\nu+1)f_\nu = -\delta(\xi-1) \tag{5.6}$$

with the boundary condition $f'[\xi = \xi_B] = 0$. The solutions are given in terms of the Legendre functions of the first and second kinds:

$$f_\nu[\xi] = -k_\nu^B P_\nu[\xi] - Q_\nu[\xi] \quad , \quad k_\nu^B = -\frac{Q'_\nu[\xi_B]}{P'_\nu[\xi_B]} = -\frac{\xi_B Q_\nu[\xi_B] - Q_{\nu-1}[\xi_B]}{\xi_B P_\nu[\xi_B] - P_{\nu-1}[\xi_B]} \tag{5.7}$$

So the full electrostatic potential is

$$\begin{aligned} \Phi\big(\boldsymbol{r}\,\big|L,\xi_B\big) &= -\frac{Q_e}{4\pi L}\sum_{\nu=1,3,5,\ldots}(8\nu+4)P_\nu[\eta]\big(k_\nu^B P_\nu[\xi] + Q_\nu[\xi]\big) \\ &= \frac{Q_e}{4\pi L}\frac{2}{\xi+\eta} + \frac{(-Q_e)}{4\pi L}\frac{2}{\xi-\eta} - \frac{Q_e}{4\pi L}\sum_{\nu=1,3,5,\ldots}(8\nu+4)k_\nu^B P_\nu[\xi]P_\nu[\eta] \end{aligned} \tag{5.8}$$

We've used the Neumann expansion of Legendre functions (see e.g. [89]) to write down the second equality: in there the first two terms are nothing but the usual Coulomb potentials by the $\pm Q_e$ charges, while the last summation term reflects the nontrivial boundary contribution. At very large ν the summed term goes asymptotically like $\nu\xi^\nu/\xi_B^{2\nu+2}$ so it is guaranteed to converge as $1 < \xi \leq \xi_B$. The electric field $\boldsymbol{E} = -\bigtriangledown\Phi$ is calculated using (5.14) for which we skip displaying the lengthy results.

The volume occupied by the electric field (i.e. the ellipsoid within ξ_B) is

given by

$$V_E(L,\xi_B)=\int_1^{\xi_B}d\xi\int_{-1}^{1}d\eta\int_0^{2\pi}d\phi\,H_\xi H_\eta H_\phi=\frac{\pi L^3}{6}\xi_B(\xi_B^2-1) \tag{5.9}$$

And the total electric field energy in this volume is given by

$$\begin{aligned}
\mathcal{E}_{total}(L,\xi_B)&=\int_1^{\xi_B}d\xi\int_{-1}^{1}d\eta\int_0^{2\pi}d\phi\,H_\xi H_\eta H_\phi\,\frac{\rho_e\times\Phi(\xi,\eta)}{2}=\mathcal{E}_{self}+\mathcal{E}_E\\
\mathcal{E}_{self}&=\frac{Q_e^2}{4\pi L}\frac{1}{(\xi+\eta)\to 0}+\frac{Q_e^2}{4\pi L}\frac{1}{(\xi-\eta)\to 0}\\
\mathcal{E}_E&=-\frac{Q_e^2}{4\pi L}+\frac{Q_e^2}{4\pi L}\sum_{\nu=1,3,5,\ldots}(8\nu+4)k_\nu^B\equiv\frac{Q_e^2}{4\pi L}\bar{\mathcal{E}}_E(\xi_B)
\end{aligned} \tag{5.10}$$

The $\mathcal{E}_{self}$ is the familiar self-interaction of the two charges which we discard. The "real" interactional energy $\mathcal{E}_E$ consists (again) a Coulomb piece and a boundary modification.

We conclude this section by one remark: so far the two key variables L and ξ_B remain free parameters: they will be related in the next section

The Parabolic Coordinates

In this appended part we briefly list the parabolic coordinates formulae needed for the calculation in Sec.2.

The coordinates we use are (ξ,η,ϕ) with two focal points at $\pm a\hat{\mathbf{z}}$, which are related to cylindrical coordinates (ρ,ϕ,z) by

$$\rho=a\sqrt{(\xi^2-1)(1-\eta^2)}\quad,\quad\phi=\phi\quad,\quad z=a\xi\eta \tag{5.11}$$

The variables are valued as $\xi\in(1,\infty)$, $\eta\in[-1,1]$, $\phi\in[0,2\pi)$. Writing $ds^2=H_\xi^2d\xi^2+H_\eta^2d\eta^2+H_\phi^2d\phi^2$, we have

$$H_\xi=a\frac{\sqrt{\xi^2-\eta^2}}{\sqrt{\xi^2-1}}\quad,\quad H_\eta=a\frac{\sqrt{\xi^2-\eta^2}}{\sqrt{1-\eta^2}}\quad,\quad H_\phi=a\sqrt{(\xi^2-1)(1-\eta^2)} \tag{5.12}$$

The Laplacian is given by

$$\bigtriangledown^2=\frac{1}{a^2(\xi^2-\eta^2)}\left\{\frac{\partial}{\partial\xi}\left[(\xi^2-1)\frac{\partial}{\partial\xi}\right]+\frac{\partial}{\partial\eta}\left[(1-\eta^2)\frac{\partial}{\partial\eta}\right]+\left[\frac{1}{\xi^2-1}+\frac{1}{1-\eta^2}\right]\frac{\partial^2}{\partial\phi^2}\right\} \tag{5.13}$$

Finally the gradient is given by

$$\nabla = \hat{\xi}\frac{\partial}{H_\xi \partial \xi} + \hat{\eta}\frac{\partial}{H_\eta \partial \eta} + \hat{\phi}\frac{\partial}{H_\phi \partial \phi} \tag{5.14}$$

For more details one could consult books such as [**?**].

5.3 The Free and Potential Energy of Two Charges

With the solutions of electric field from preceding section, we now examine the balance between the electric field energy and the surrounding magnetic medium in two settings: slow and fast separation of the two charges to a finite distance L with the outcome being respectively the free and potential energy associated with them.

5.3.1 Free Energy from Slow Separation

As we discussed in the introduction, when the two charges are separated in an adiabatically slow way, the *super* component of the magnetic medium i.e. the monopole condensate will be expelled (in an idealized picture) entirely out of the volume V_E occupied by electric field. Suppose the condensate has a negative energy density $-\mathcal{E}_C$ (thus a positive pressure), then the overall change in energy brought about by separating the charges will be

$$\Delta E \quad = \mathcal{E}_E(L, \xi_B) + \mathcal{E}_C(T) V_E(L, \xi_B) \tag{5.15}$$

Now for given charge separation L and bulk temperature T, we determine the physical size of flux bag ξ_B^{phy} by minimizing the above ΔE, i.e. the physical boundary $\xi_B^{phy}(L, T)$ satisfies:

$$\left.\frac{\partial \Delta E}{\partial \xi_B}\right|_{\xi_B = \xi_B^{phy}} = 0 \tag{5.16}$$

Combining the above with Eq.(5.9,5.10) we then obtain

$$\left[\frac{1}{3\xi_B^2 - 1}\frac{d\bar{\mathcal{E}}_E}{d\xi_B}\right]\Bigg|_{\xi_B = \xi_B^{phy}} = -\left(\frac{L}{l_C}\right)^4 \tag{5.17}$$

Here we introduced a length scale $l_C \equiv (6\,\alpha_E/\pi\mathcal{E}_C)^{1/4}$ with $\alpha_E \equiv Q_e^2/4\pi$. This equation could be solved easily by numerics. For each L with the above determined ξ_B^{phy}, we obtain via (5.15) the free energy associated with the static dipole as a function of separation L, as shown in Fig.5.2(a). It turns out to be Coulomb at short distance(see the magenta dashed curve) plus linear at large distance(see the blue dashed line). The occurrence of a linear part is due to the physical effect that for large L the medium pressure (with which the electric field has to balance) limits the transverse size of flux bag (where the field gets weak as L increases) to saturate rather than grow forever: thus the bag shape approaches a cylinder. Mathematically, as $L \to \infty$ one finds $\xi_B^{phy} \to 1$ but $L \cdot \sqrt{(\xi_B^{phy})^2 - 1} \to finite$. In Fig.5.1(c) the four bag shapes are at growing L with ξ_B determined as in the above, which clearly shows the shape becomes more and more cylindrical at large L.

By fitting the dimensionless slop of the linear part in Fig.5.2(a) we obtain the free energy string tension σ_F to be

$$\sqrt{\sigma_F} = 2.32 \times \alpha_E^{1/4} \times \mathcal{E}_C^{1/4} \tag{5.18}$$

Inversely, since we know $\sigma_F(T)$ from lattice as shown in Fig.5.1, from the above formula we can obtain the T-dependence of $\mathcal{E}_C$: see Fig.5.2(b). The two curves are for α_E being 0.5(upper) and 1(lower) respectively. In both cases, $\mathcal{E}_C$ decreases and in particular drops very quickly when approaching T_c. The interpretation is natural: toward T_c the monopole condensate becomes less and less due to increasing thermal excitations and eventually dies out at deconfinement transition.

A connection can be made between our result (5.18) and the dual superconductor model (also known as Abelian Higgs model) of vacuum confinement [54]. In that model, a quadratic Higgs potential leads to a Higgs condensate (the prototype of postulated monopole condensate) ϕ_0 (with dimension of mass). By solving ANO flux tube a string tension is obtained in the form $\sqrt{\sigma} = c_1\phi_0$ with the coefficient determined by gauge and Higgs coupling constants λ, g. On the other hand the Higgs potential tells that the condensate has a negative energy density $-\mathcal{E}_C = -\lambda\phi_0^4/2$, thus one has $\sqrt{\sigma} = c_2\mathcal{E}^{1/4}$ with the coefficient to be determined numerically with given λ, g, see discussions e.g. in [90]. While their model works only at $T = 0$, our model for σ_F extends to T_c.

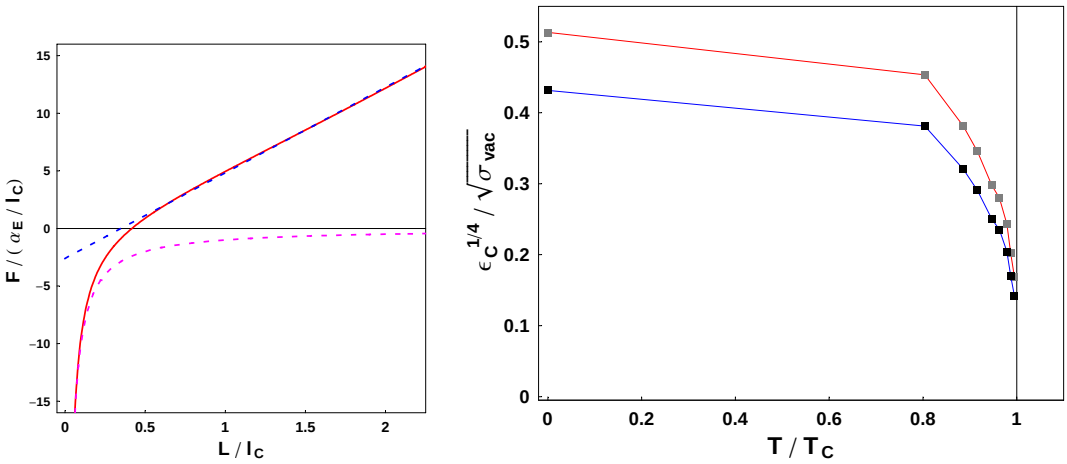

Figure 5.2: (a)(left) free energy F (in unit of α_E/l_C) versus separation L/l_C; (b)(Right) monopole condensate energy density $\mathcal{E}^{1/4}$ in unit of $\sqrt{\sigma_{vac}}$, the two curves are for α_E being 0.5(upper) and 1(lower) respectively.

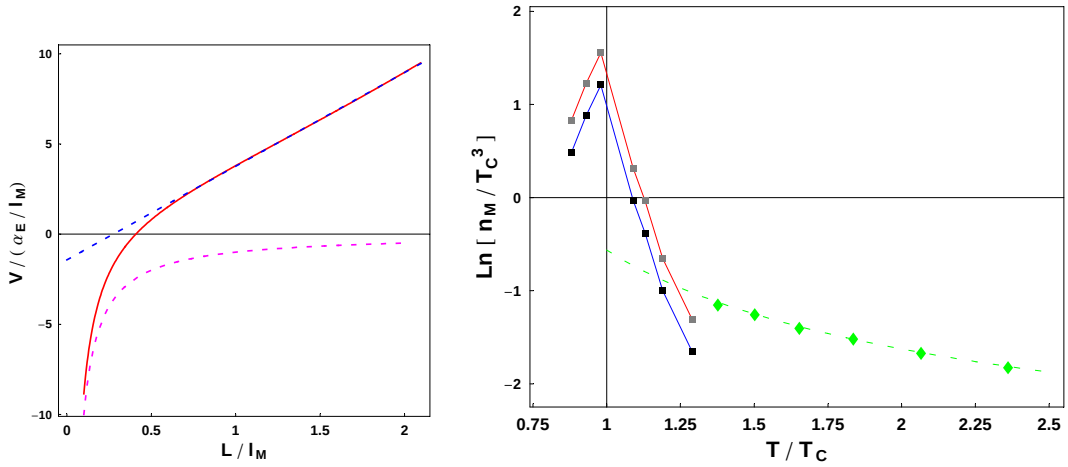

Figure 5.3: (a)(left) potential energy V (in unit of α_E/l_M) versus separation L/l_M; (b)(Right) thermal monopole density n_M/T^3, the two curves across boxes are for α_E being 0.5(upper) and 1(lower) respectively, and green curve across diamonds shows lattice data for $T > 1.3T_c$.

5.3.2 Potential Energy from Fast Separation

Now we study the case of separating the two charges to a finite distance L within a time much smaller than the relaxation time of the *normal* component, the thermal monopoles. In particular we focus on the region about $0.8-1.3T_c$, as this is the place where thermal monopoles are substantial and dominant.

During such fast process, each monopole originally in the volume to be occupied by the electric filed (i.e. the ellipsoidal bag) will get a "kick" due to the dual Faraday effect but have no time to release this energy into the surrounding medium. Consider the charges move from $z = C$ to $z = C + \delta z$ in δt, then the electric flux penetrating the plane $z = C$ changes from 0 to Q_e, thus generating a magnetic dynamical voltage $Q_e/\delta t$. For a monopole at ρ from $\hat{z}$ axis, the force is $Q_m(Q_e/\delta t)/(2\pi\rho)$, thus it gets the "kick" and obtains a momentum $\delta p = Q_m Q_e/(2\pi\rho)$, forming strong *non-thermal* normal currents. For a bag (L, ξ_B) formed after separation, the total kinetic energy passed to the monopoles is obtained by integration over the bag volume (with $D \equiv Q_m Q_e/4\pi = 1$):

$$\Delta K_M = \int_1^{\xi_B} d\xi \int_{-1}^{1} d\eta \int_0^{2\pi} d\phi \, H_\xi H_\eta H_\phi \frac{4n_M\, D}{L\sqrt{(\xi^2-1)(1-\eta^2)}} = \frac{\pi^2 D n_M}{2} L^2 \xi_B (\xi_B^2-1)^{1/2} \tag{5.19}$$

We emphasize in the above only the monopole density $n_M(T)$ enters as a property of the medium depending on T, while other properties shall not be "felt" in such fast process.

Now the total energy change should be $\Delta E = \mathcal{E}_E(L, \xi_B) + \mathcal{E}_C V_E + \Delta K_M(L, \xi_B)$ with the new term causing the splitting between free/potential energy. Since the condensate term $\mathcal{E}_C V_E$ is small close to T_c (as we showed in previous subsection) and vanishes above T_c, we neglect it here for simplicity, i.e. $\Delta E \approx \mathcal{E}_E(L, \xi_B) + \Delta K_M(L, \xi_B)$. To obtain the physical value ξ_B^{phy} we need to minimize ΔE according to ξ_B, which leads to

$$\left.\frac{\partial \Delta E}{\partial \xi_B}\right|_{\xi_B = \xi_B^{phy}} = 0 \tag{5.20}$$

This can be written as

$$\left.\left[\frac{\sqrt{\xi_B^2-1}}{2\xi_B^2-1}\frac{d\bar{\mathcal{E}}_E}{d\xi_B}\right]\right|_{\xi_B = \xi_B^{phy}} = -\left(\frac{L}{l_M}\right)^3 \tag{5.21}$$

Here we introduced a different length scale $l_M \equiv (2\,\alpha_E/\pi^2 D n_M)^{1/3}$. Not surprisingly we find the potential energy, shown in Fig.5.3(a), to be a Coulomb at

short distance(see the magenta dashed curve) plus linear at large distance(see the blue dashed line).

But now the string tension is given by a different formula:

$$\sqrt{\sigma_V} = 3.88 \times \alpha_E^{1/6} \times n_M^{1/3} \tag{5.22}$$

Since we know σ_V from lattice data in the $0.8 - 1.3T_c$ region, by the above formula we can convert them into data of thermal monopole density $n_M(T)$ in the same region: see the two curves across boxes for α_E being 0.5(upper) and 1(lower) respectively in Fig.5.3(b). The green diamonds and the dashed curve in Fig.5.3(b) represent recent lattice data for monopole density above $1.3T_c$ from [64]. Thus our estimates for the monopole density agree well with what was seen directly, by identifying monopoles on the lattice.

A few comments are in order: (i) for $0.8 - 1T_c$ the density quickly grows toward T_c while results in previous subsection show ceasing of condensate in that region, which are all well consistent with the notion that close to T_c monopole condensate is substantially excited into thermal monopoles; (ii) around $1.3T_c$ we see our results connect well to the higher T lattice data; (iii) cooling down to T_c we find the monopole density blows up indicating they become light and dominant in the plasma and presumably reach condensation point at T_c; (iv) the strongly increasing density also suggests rapid increase of magnetic screening toward T_c, which is agreement with lattice results [38].

A hard question is to understand why the density n_M/T^3 increases roughly by *one order of magnitude* from $1.3T_c$ to T_c, definitely going beyond simple gas model with tunable mass $M(T)$. It is clear that near T_c the monopoles must become very light and a large number of monopole-anti-monopole pairs will pop out with little energy cost. On the other hand one wonders what is the mechanism to stop the pair creation at some point. A possible explanation is that the monopoles have finite size cores thus as soon as they are dense enough to touch the neighbors' cores the pair creation has to be stopped as the energy cost now will be enormous. In short, the very dense monopole plasma near T_c seems to be a densely packed ensemble of "hard spheres". From the monopole-monopole and monopole-anti-monopole equal-time correlators published in [64] we had evidence for a core size about $R_{core} \sim 0.25fm$: in their unit it amounts to a density $Ln[n/T_c^3] \approx Ln[1/(4\pi R_{core}^3/3)/T_c^3] \approx 1.5$ in the densely-packed limit. Furthermore if one takes the 't Hooft-Polyakov monopole's size formula $R_{core} = 1/ev$ (with e the electric coupling and v the Higgs vev), then a densely-packed density $n \sim (ev)^3$: the rapid growth by a factor ~ 10 as T goes from $1.3T_c \to T_c$ will indicate growth in e by a factor 2 which is reasonable.

5.3.3 Summary

A general outcome of our results is further confirmation of the "magnetic scenario"[49][80] for sQGP, according to which in the temperature region $1.3T_c \to T_c$ the monopole plasma is extremely densely-packed liquid.

We showed how the nontrivial T-dependence of the static $\bar{Q}Q$ free energy $F(r,T)$ and potential energy $V(r,T)$ could be related to the "elliptical bags" becoming flux tubes. We identified them with slow/fast processes respectively (i.e. the process of separating $\bar{Q}Q$ to a finite separation L). The supercurrent due to condensed monopoles which has no dissipation remains even for slow process, while that due to "normal" monopoles are produced in fast process and are dissipated after some finite relaxation time. The letter are responsible for the difference between the free/potential energy tells important information about the thermal monopoles at $T \approx T_c$. At $T \approx T_c$ from below the monopole condensate dies out, as signaled by vanishing σ_F, while the contribution of "normal" monopoles with density n_M explains $\sigma_V - \sigma_F$, including its large peak around T_c. An analytic flux bag model was developed as a good tool to describe the linear potentials by which we were able to relate σ_F to the condensate energy density $\mathcal{E}_C$ in (5.18) and relate σ_V to the thermal monopole density n_M in (5.22). The obtained $n_M(T)$ agrees well with the recent lattice observations of monopole at higher T.

5.4 Electric Flux Tube in a Magnetic Plasma

In this section we study a separate, idealized question: can an infinitely long flux tube be formed in a magnetic plasma? Though this is not directly related to the potential problem, it was motivated by the linear part of potential even above T_c which indicates the existence of flux tube in the plasma phase. Two different approaches will be taken: one is a macroscopic electrodynamics calculation which found solutions to a modified-London equation that might be valid in a magnetic plasma; the other is a microscopic, quantum mechanical calculation, in which we statistically sum the induced magnetic current from each single monopole's quantum scattering on the flux tube and derive a self-consistent condition by using the dual Maxwell's equation.

5.4.1 Electric Flux Tube: Macroscopic approach

Borrowing wisdom from electrodynamics of a superconductor and being motivated by the "modified London" relation (2.6) we discussed above, we find in

this section solutions to macroscopic electrodynamics equations of London's type.

Our generalized (dual) version of the second London equation reads:

$$\bigtriangledown \times \boldsymbol{J}_M = \frac{c}{\lambda^{2-\kappa} r^{\kappa}} \boldsymbol{E} \tag{5.23}$$

Any constant coefficient could be absorbed in a re-definition of λ. When combined with one of the (dual) Maxwell's equations $\bigtriangledown \times \boldsymbol{E} = -\frac{1}{c}\boldsymbol{J}_M$, it yields the equation for the electric field

$$\bigtriangledown^2 \boldsymbol{E} = \frac{1}{\lambda^{2-\kappa} r^{\kappa}} \boldsymbol{E} \tag{5.24}$$

Macroscopic parameter κ characterizes how the electric field gets modified by the magnetic medium. $\kappa = 0$ is the London limit (appropriate for the medium being a dual superconductor in extremely type-I regime), while $\kappa = 1$ corresponds to the classical monopole gas (as discussed in preceding section). Intermediate values of κ are suggested as an interpolation between the two limits, say to describe a medium having both Bose condensed and non-condensed components.

Our setup corresponds to cylindrical flux tube, with $\boldsymbol{E} = E(r)\hat{z}$ in coordinates (r, ϕ, z). The total electric flux is $\Phi_E = \int_0^\infty E(r) 2\pi r dr$.

The solution for any $\kappa < 2$ is given by[2]

$$\begin{aligned} E(r) &= f_\kappa \, \frac{\Phi_E}{\pi\lambda^2} \, K_0\left[\frac{2}{2-\kappa}\left(\frac{r}{\lambda}\right)^{(2-\kappa)/2}\right] \\ f_\kappa &= 1/\left[(2-\kappa)^{\frac{2+\kappa}{2-\kappa}} \, \Gamma[2/(2-\kappa)]^2\right] \end{aligned} \tag{5.25}$$

with $K_0[x], \Gamma[x]$ being the Bessel and Euler Gamma functions. If a function $F_0[r/\lambda]$ is a solution to London eq.(5.24) with $\kappa = 0$, then the function $F_\kappa[r] \propto F_0\left[\frac{2}{2-\kappa}(r/\lambda)^{(2-\kappa)/2}\right]$ is a solution to the modified eq.(5.24) with any κ. The normalization constant follows from the total flux value.

At large distance, $r \to \infty$, the electric field

$$E \sim exp\big[-(r/\lambda)^{(1-\kappa/2)}/(1-\kappa/2)\big] \Big/ (r/\lambda)^{(2-\kappa)/4} \tag{5.26}$$

vanishes quicker than exponential, leaving most of the flux within $r \sim \, few \, \lambda$. The smaller is κ, the thinner is the flux tube.

For this flux tube solutions the "string tension" – the energy per unit length

[2]For $\kappa \geq 2$ the boundary condition couldn't be satisfied.

along $\hat{z}$ is

$$\begin{aligned}\sigma_\kappa &= \int_0^\infty \frac{E(r)^2}{2} 2\pi r dr = \frac{\Phi_E^2}{\pi\lambda^2}\mathcal{T}_\kappa \qquad (5.27)\\ \mathcal{T}_\kappa &= \sqrt{\pi}\Big/\Big[2^{(6-\kappa)/(2-\kappa)}\cdot(2-\kappa)^{(2+\kappa)/(2-\kappa)}\cdot \\ &\qquad \Gamma[(6-\kappa)/(4-2\kappa)]\cdot\Gamma[2/(2-\kappa)]^2\Big]\end{aligned}$$

$\mathcal{T}_\kappa$ is a rapidly decreasing function of κ, and in particular $\mathcal{T}_{\kappa=0}/\mathcal{T}_{\kappa=1} = 3$ which means that (for fixed λ) a quantum condensate expels the electric flux into a flux tube with the tension three times larger than a classical monopole gas does.

Let's summarize the physical picture as well as limitations of the established solution. Any magnetic medium generically expels the electric field, as monopoles are back-scattered off it, so there is possibility for flux tube formation. But different media do this job with distinct efficiencies, leading to flux tube (if there is any) with different tensions. The electric flux tube solutions are rather simple: they describe the problem in terms of two macroscopic properties of magnetic medium, namely κ and λ. There is however an important limitation. The macroscopic approach is suitable only if *the electric field strength (or the electric flux here) is large*, as the detailed analysis in the introductory examples has shown: we repeat that strong field makes small Larmor radius of monopoles, thus the flux tube is a "macroscopic" object and scattering of monopoles happens basically on the surface. If it is not so, the validity of eqn.(5.23,5.24) upon which the solution is based is no longer justified. The intermediate case between diffusive weak field and macroscopically strong flux tube requires a microscopic approach, to be discussed in the following sections.

5.4.2 The Microscopic Approach

Starting here we will pursue a fully quantum mechanical microscopic approach. Let us first describe our strategy and approximations made in this section. The main one is that mutual interaction among monopoles will be neglected, as it has been argued that magnetic sector of sQGP at just above T_c is very weakly coupled, see [49] for more details. What's more, if one assumes the monopoles are of 't Hooft-Polyakov, the Coulomb interaction between monopoles may be largely cancelled (and exactly cancelled in the BPS limit for static monopoles)

by scalar/Higgs exchange. But the Lorentz force from electric field[3] cannot be cancelled and this is the only interaction of monopoles relevant to our approach. The single monopole scattering on a flux tube will be treated quantum mechanically. Both non-relativistic and relativistic cases will be analyzed: there are evidences that monopoles in sQGP are semi-relativistic, e.g. with $M \sim 2T$. The monopoles we consider have no spin: although the classical 't Hooft-Polyakov solutions may not appear exactly spherically symmetric, any change induced by their rotation can be compensated by a gauge transformation. (In other words, the only thing violating spherical symmetry is the Dirac string which is unphysical by itself, see e.g. discussions in [53].)

In the following sections we will go through the three steps below: i) first assume existing flux tube of certain size R, ii) then figure out in great details how individual monopole from medium will be scattered off it and generate some magnetic current, and iii) finally use the dual Maxwell's equation relating the electric field and magnetic current to obtain a self-consistent equation determining the value of R (and thus string tension σ) as a function of medium parameters T, n, M. Below we extend the description of strategy a bit more step by step. The first two steps are already done in Section.2.3.2., we now discuss the final step.

The dual Maxwell equation, $\bigtriangledown \times \boldsymbol{E} = -\frac{1}{c}\boldsymbol{J}_M$, in cylindrical setup being

$$\frac{d\,E(r)}{dr} = \frac{1}{c} J_M^{\phi} \tag{5.28}$$

can be integrated in r

$$E(r=0) - E(r=R) = -\frac{1}{c}\int_0^R J_M^{\phi} dr \tag{5.29}$$

The flux tube may presumably be approximated by a constant E inside certain radius $r < R_-$ and zero outside $r > R_+$, with smooth interpolation in between. As an approximation in step(i) we have used step-like electric field, neglecting the difference between $R_\pm$. The advantage is that monopole motion in such field can be calculated (step (ii)). This shouldn't be a serious issue as we expect $R_+ - R_- << R$. Thus we take $E(r=0)$ as the constant field strength $E_I = \Phi_E/(\pi R^2)$ within tube and send $E(r=R)$ to zero, obtaining the equation

[3]Although the monopoles in sQGP are built out of non-Abelian fields A_μ^a, each type of monopoles only interacts with electric field projected into their corresponding U(1) (see e.g.[53][54]), so the Maxwellian field description still holds.

to be used in later section:

$$E_I = \Phi_E/(\pi R^2) = -\frac{1}{c}\int_0^R J_M^\phi dr \tag{5.30}$$

Now we will self-consistently determine the size R of the electric flux tube carrying flux $\Phi_E = d \times (2\pi\hbar c)/g$ in an ensemble of monopoles with temperature T and density n, by using the *integrated*[4] magnetic current obtained in Section2.3.2.

At this stage the issue is to average the integrated total current $\mathcal{I}(kR)$ over proper thermal distribution $n(k|T)$ (through which the medium property comes into play) satisfying $n = \int_0^\infty dk\, n(k|T)$. We have

$$\frac{1}{c}\int_0^R J_M^\phi dr = \frac{g\hbar}{Mc}\int_0^\infty dk\, n(k|T)\, \mathcal{I}(kR) \tag{5.31}$$

Note in relativistic case we have to replace the mass M by $\epsilon(k)/c^2$ and move it inside the integration over k. Below we deal with non-relativistic gas, relativistic gas, and optimally correlated ensemble separately.

Non-Relativistic Gas

In non-relativistic(NR) gas with Mc^2/k_BT large, the kinetics are simplified, yet in principle one still needs to take into account the quantum statistics, namely using the Bose-Einstein(BE) distributions. Only in the non-degenerate limit (with monopole gas being not dense) one recovers the Boltzmann limit. So we use the BE distribution $1/(z^{-1}e^\epsilon - 1)$ normalized to density n by

$$n = s \times \left(\frac{Mk_BT}{2\pi\hbar^2}\right)^{3/2} \times Li_{\frac{3}{2}}[z] \tag{5.32}$$

In the above s is the degeneracy due to internal degrees of freedom, fugacity $z = e^{\mu/k_BT}$ is related to chemical potential and valued as $0 \le z < 1$ in NR case, and $Li_{3/2}[z]$ is the polylogarithm function. We then have the $n(k|T)$ given by (after integrating out the $\hat{z}$ momentum)

$$n(k|T)dk = s \times \left(\frac{Mk_BT}{2\pi\hbar^2}\right)^{3/2} \times Li_{\frac{1}{2}}\left[z\, e^{-y^2}\right]\; 2y\, dy \tag{5.33}$$

[4]Since we are not interested in details of the flux tube shape, we refrain from doing more complicated local matching of the current and the $\bigtriangledown \times \boldsymbol{E}$, as local form of Maxwell equation demands.

with the variable $y = \hbar k/(2Mk_BT)$.

Now by combining eq.(5.30)(5.31)(5.33) we obtain the self-consistent equation for flux tube size R:

$$E_I = \frac{\Phi_E}{\pi R^2} = \frac{g\hbar n}{Mc} \times \frac{\hbar^2}{R^2 M k_B T} \times \mathcal{U}\left[q = \frac{R}{\sqrt{\hbar^2/\pi M k_B T}}\right] \tag{5.34}$$

with the last term $\mathcal{U}$ from integration over $x = kR$

$$\mathcal{U}[q] = \quad -\int_0^\infty dx\ x\ \frac{Li_{\frac{1}{2}}[z\, e^{-\pi x^2/2q^2}]}{Li_{\frac{3}{2}}[z]}\ \mathcal{I}(x) \tag{5.35}$$

The self-consistent equation can be further rewritten in an elegant way:

$$\frac{2d}{\pi} \times \left(\frac{\lambda_L}{\lambda_{dB}}\right)^2 = \mathcal{U}\left[q = \frac{R}{\lambda_{dB}}\right] \tag{5.36}$$

with $\lambda_L = (Mc^2/g^2 n)^{1/2}$ and $\lambda_{dB} = (\hbar^2/\pi M k_B T)^{1/2}$. So for given parameters one uniquely determines the flux tube size R from the above equation.

The NR Boltzmann limit, satisfying scale hierarchy $1/n^{1/3} >> \hbar/\sqrt{Mk_BT} >> \hbar/(Mc)$, can be achieved by simply replace $\frac{Li_{\frac{1}{2}}[z\, e^{-\pi x^2/2q^2}]}{Li_{\frac{3}{2}}[z]}$ in the integration of $\mathcal{U}[q]$ by $e^{-\pi x^2/2q^2}$. Mathematically this follows from taking the $z \to 0$ limit (with only linear terms left) of both polylogarithm functions.

The results from solving eq.(5.36) are plotted in Fig.5.4. Numerically we didn't see much difference between $z \to 0$(blue curve) and $z \to 1$(red curve) limits. As $\lambda_L/\lambda_{dB} \propto (T/n)^{1/2}$, the right end of the horizontal axis corresponds to high-density/low-temperature regime while the left end represents low-density/high-temperature regime.

The distinguished feature is the existence of critical point for λ_L/λ_{dB} beyond which there will be no self-consistent solution: this occurs at roughly the same value for both displayed curves and we obtain the following condition for the existence of flux tube

$$\frac{\lambda_L}{\lambda_{dB}} = \left(\frac{\pi M^2 c^2 k_B T}{\hbar^2 g^2 n}\right)^{1/2} \leq 0.13 \tag{5.37}$$

Physically the above result is very appealing: it demonstrates the mechanism of how a flux tube which exists in the medium at low T is eventually

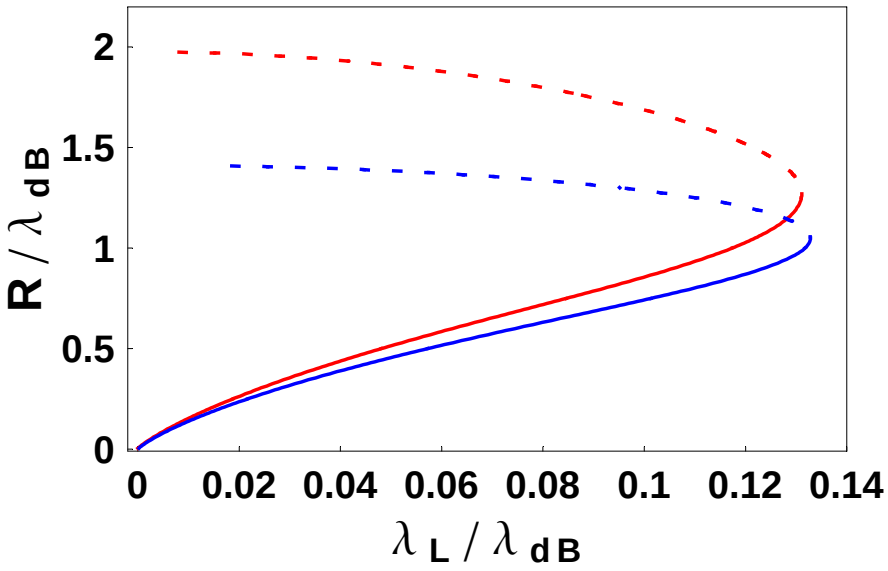

Figure 5.4: R/λ_{dB} versus λ_L/λ_{dB} from solution of eq.(5.36). The blue curve is for Boltzmann limit ($z \to 0$) while the red for $z = 0.999$, see text.

gone as the medium is heated up; on the other hand, for a medium with given T it sets up a lower bound of monopole density that is required to support the existence of flux tube.

Another feature is that for each given λ_L/λ_{dB} smaller than the critical value, there are actually two solutions, one with small R/λ_{dB} (typically smaller than 1, see solid curves) and the other with large R/λ_{dB} (typically greater than 1, see dashed curves). This is understandable according to the complicated wiggle structure of $\mathcal{I}(kR)$. The solution with smaller radius is the stable one: it is much thinner and thus has stronger electric field ($E \sim \Phi_E/r^2$), which reflects monopoles more sharply near the boundary. The other solution with larger R/λ_{dB} is unstable and should be discarded.

Relativistic Gas

In relativistic gas the important scale is set by temperature, so let's introduce the following dimensionless variables:

$$w = \frac{R}{\hbar c/k_B T} \quad , \quad u = \frac{Mc^2}{k_B T} \tag{5.38}$$

The fugacity z, now in range $0 < z < e^u$, is related to density by

$$\begin{aligned} n &= s \times \left(\frac{k_B T}{\hbar c}\right)^3 \int_0^\infty \frac{t^2\, dt/(2\pi^2)}{z^{-1} e^{\sqrt{u^2+t^2}} - 1} \\ &= s \times \left(\frac{k_B T}{\hbar c}\right)^3 \times \mathcal{C} \end{aligned} \tag{5.39}$$

with the number s the degeneracy due to internal degrees of freedom. $\mathcal{C}$ serves as normalization constant to momentum distribution (after scaling momenta by $k_B T/c$).

The distribution over k is given by

$$n(k|T) dk dK_z = s \times \frac{k\, dk\, dK_z/(4\pi^2)}{z^{-1} e^{\epsilon(k,K_z)/k_B T} - 1} \tag{5.40}$$

with $\epsilon(k, K_z) = \sqrt{M^2c^4 + \hbar^2 k^2 c^2 + \hbar^2 K_z^2 c^2}$. Similarly combining the above with eq.(5.30)(5.31) one obtains the relativistic version of the self-consistent equation

$$E_I = \frac{\Phi_E}{\pi R^2} = \frac{g\, n}{4\pi^2\, (k_B T/\hbar c)} \times \mathcal{U}[w] \tag{5.41}$$

with $\mathcal{U}[w]$ given by the following integral

$$\begin{aligned} \mathcal{U}[w] = \quad & -\frac{1}{\mathcal{C}} \int_0^\infty dx\, x\, \mathcal{I}(w\, x) \\ & \times \int_{-\infty}^\infty dy\, \frac{1/\sqrt{u^2+x^2+y^2}}{z^{-1} e^{\sqrt{u^2+x^2+y^2}} - 1} \end{aligned} \tag{5.42}$$

We can further rewrite the self-consistent equation as

$$8\pi^2 d \times \left(\frac{\tilde{\lambda}_L}{\tilde{\lambda}_{dB}}\right)^2 = w^2\, \mathcal{U}[w|u, z] \tag{5.43}$$

with the newly introduced relativistic parameters $\tilde{\lambda}_L = (k_B T/g^2 n)^{1/2}$ and $\tilde{\lambda}_{dB} = \hbar c/k_B T$.

For given sets of parameters M, n, T (or equivalently u, z, T) one can easily find the flux tube size R from the above equations by direct numerics. The situation is quite similar to the non-relativistic gas which we skip further discussion.

Optimally Correlated Ensemble

Finally let's discuss ensemble beyond an ideal gas. Clearly with significant interparticle correlations the ensemble may even not be easily describable by any distribution, however a typical momentum $\bar{k}_T$ can still be invoked. A special situation which we call optimally correlated ensemble is that monopoles from such ensemble are largely carrying momenta within very narrow region around $\bar{k}_T$. On the contrary if the ensemble particles' momenta are very diffusive in momentum space, it can hardly support flux tube.

In the optimally correlated ensemble, we approximate eq.(5.31) as (assuming NR formulae)

$$\frac{1}{c}\int_0^R J_M^\phi dr = \frac{gn\hbar}{Mc}\mathcal{I}(\bar{k}_T R) \tag{5.44}$$

and the self-consistent equation is then given by

$$E_I = \frac{\Phi_E}{\pi R^2} = \frac{gn\hbar}{Mc} \times [-\mathcal{I}(\bar{k}_T R)] \tag{5.45}$$

We limit the value of $\bar{k}_T R$ within $0 - 1.42$ beyond which there won't be flux tube solution, as discussed in Section.IV C.

The above can be re-organized into

$$2d \times (\bar{k}_T \cdot \lambda_L)^2 = (\bar{k}_T R)^2 \times [-\mathcal{I}(\bar{k}_T R)] \tag{5.46}$$

The best situation occurs (roughly) around the negative peak in $\mathcal{I}(kR)$ given by (2.39). From this we set a bound similar to eq.(5.37)

$$\bar{k}_T \cdot \lambda_L = \left(\frac{Mc^2\bar{k}_T^2}{g^2 n}\right)^{1/2} \leq 0.20 \tag{5.47}$$

5.4.3 Disappearance of Flux Tubes in sQGP

Results from previous subsection is general in nature and applicable to a variety of plasma physics problems. The present subsection, on the other hand, is dedicated to possible application of our results to the physics of sQGP. From now on we switch to natural units and systematically put $\hbar, c, k_B = 1$.

The existence of string/flux tubes in the QCD confined phase $T < T_c$ is rather thoroughly investigated on lattice, via measurements of static heavy quark potentials. Static free energy potentials $F(T, r)$ as a function of r are only studied for $N_c = 3$ but for number of quark flavors $N_f = 0, 2$ as well as physical QCD, see [76]. Those can be used to extract the entropy and potential energy separately: the peaks of these quantities (see e.g. Fig.2 of [76]) happen

to be exactly at $T = T_c$ and then decrease toward larger T. The presence of the quasi-linear part of the energy and entropy at intermediate r leads to a conclusion that flux tubes still exist at $T > T_c$. Fig.5.5 from [76] shows how both the internal energy and entropy look like at $T = 1.3T_c$. Unlike in the free energy (open squares in the upper plot, in which cancellation takes place), the internal energy (closed circles) still show at intermediate $r = (.3 - .7)\, fm$ a part linearly dependent on r, while at $T > 1.3T_c$ it very quickly disappears.

Why are flux tubes disappearing at large T? It can in principle be due to two different changes in QGP happening as T grows above T_c, to be called (i) electric screening and (ii) magnetic penetration. The simplest mechanism (i) is that as T grows beyond T_c, the density of electrically charged quasiparticles – gluons and quarks – is growing and eventually it becomes large enough to screen heavy quarks. The reason for this density growth is the decrease in effective masses of electric excitations, which are lattice observables by themselves[5]. At very large $T >> T_c$, in weak (electric) coupling domain, the screening of the potential is expected to be described by the Debye theory. However Debye theory does not describe entropy and internal energy associated with static quarks at $T = (1 - 1.3)T_c$, even at large distances, as can be seen e.g. from calculations of Antonov et al [78].

Another effect (ii), discussed for the first time in this work, is the penetration of magnetically charged quasiparticles (MQPs) inside the flux tubes, which destroys them. Indeed, the key parameter $\bar{k}R$ increases with T and reaches the critical value eq.(5.47) for whether flux tube can exist or not. This imposes the following condition

$$\frac{g^2}{4\pi}(\frac{n}{T^3}) \geq 2.0 \left(\frac{\bar{k}_T}{T}\right)^2 \frac{M}{T} \tag{5.48}$$

Changing T from T_c upward the monopoles gets heavier and their dimensionless magnetic density n/T^3 keeps decreasing: eventually this will violate the flux tube condition. We thus identify the equality in (5.48) with the temperature $T \approx 1.3T_c$ at which local dissolution of the flux tubes takes place.

Furthermore, at $T \approx 1.3T_c$ we expect $g^2/4\pi \approx 1$ [49]. An independent consideration fixes conditions for monopole Bose condensation which demands that around T_c the monopole mass over temperature $M/T \approx 1 \sim 1.2$.

Combining these estimates with our critical condition for tube dissolution

[5]See a related discussion of various color-electric objects' effective masses in [46]. There we showed the masses are still rather large and their densities rather small at 1-1.5T_c, limiting the screening.

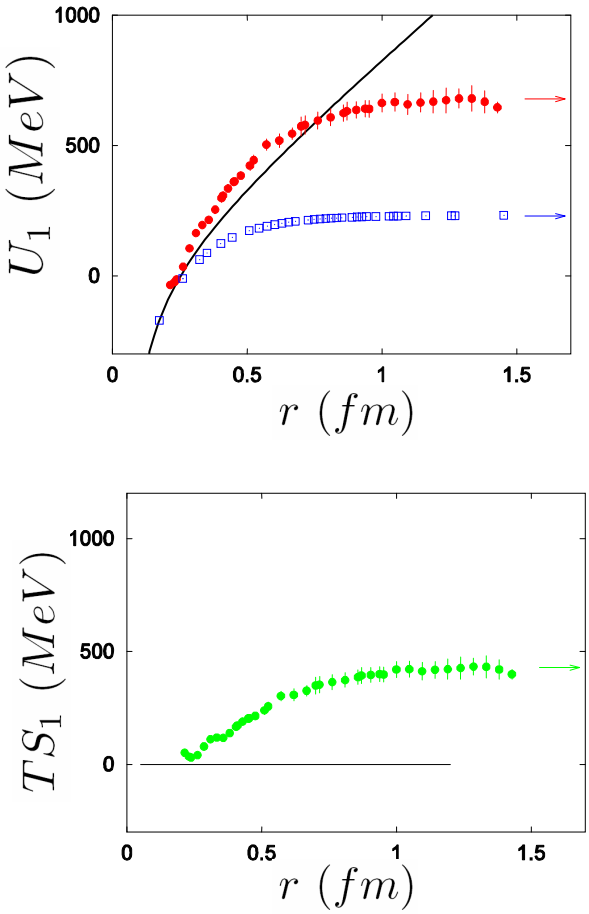

Figure 5.5: (a) The singlet internal energy, $U_1(r,T)$ (filled circles), calculated from renormalized singlet free energy, $F_1(r,T)$ (open squares), at fixed $T \simeq 1.3T_c$ in 2-flavor lattice QCD compared to $V(r,T=0)$ (line) . (b) The corresponding color singlet quark anti-quark entropy, $TS_1(r,T \simeq 1.3T_c)$, as function of distance calculated from renormalized free energies.

we obtain the density of magnetic quasiparticles at $1.3T_c$ to be

$$n_{MQPs} \approx \left(\frac{n}{T^3}\right)\Big|_{T=1.3T_c} \approx \quad 2 \sim 3 \tag{5.49}$$

which is within $n_{MQPs} = (4.4 - 6.6) fm^{-3}$ in absolute units.

Can the density of magnetic objects really be of that magnitude (which superficially looks rather high)? This estimated density includes in principle contributions from all types of magnetically charged objects in sQGP, i.e. not only pure adjoint monopoles but also self-dual dyons and also dyons containing quarks[6].

Let us compare the numbers with whatever is mentioned in literature. We don't know any studies of fermionic objects mentioned above.

Ilgenfritz et al [43] determined their dyon estimate by the caloron density, which is reliably calculated from the topological susceptibility. After multiplying by 3/2 their result for SU(2) we obtain density of self-dual dyons to be $n_{dyons} \sim 3 fm^{-3}$. Chernodub and Zakharov [80] mentioned the monopole density which is directly estimated from lattice configurations by following gauge-fixed monopoles along their trajectories. Their estimate is about $n_{mono} \approx 3.5 fm^{-3}$. The sum of the two is consistent with the upper end of our estimate of what is needed for formation/dissolution of the flux tube.

Independent comparison can also be made with the vacuum ($T = 0$) monopole density. Bali [34] has measured London penetration length by fitting lattice result with Abelian Higgs model. From that one can infer the monopole density to be as large as $10 fm^{-3}$. Bornyakov et al [91] gave the vacuum monopole density to be about $7.5 fm^{-3}$. All these results are well above our estimates for the density at $T = 1.3T_c$ "dissolution point".

We believe all these numbers are consistent and suggest a coherent picture, of very dense monopole condensate in vacuum, tightly confining electric flux into very narrow tubes. When heated slightly above T_c the monopole condensate changes into a non-condensed ensemble of monopoles, which is roughly twice less dense. Yet it is still capable of supporting flux tubes survived from vacuum, and only around $T = 1.3T_c$ the density of monopoles drops so low that there won't be flux tube any more. At higher T the electric sector becomes more and more dominant till eventually small number of heavy monopoles become embedded in the perturbative electric plasma.

[6]We recall that monopoles have fermionic zero modes and states made of fermions travelling on top of a monopole have to be included as well. In supersymmetric theories those form spin-1/2 and even 1 magnetic objects, which are needed by supersymmetry to produced appropriate supermultiplets including the usual scalar monopoles.

5.4.4 Summary and Discussions

In this Section we have studied mechanical stability of the electric flux tube in a monopole plasma. Already classical analysis hints on the existence of a critical angular momentum dividing the scattered magnetic currents which support/dissolve the flux tube. This finding is quantitatively confirmed by quantum mechanic calculation, in which we use the exact scattering solutions to Schrodinger/Klein-Gordon equation in non-relativisitic/relativistic situations. These solutions allowed us to calculate the magnetic current produced, which is then averaged over the monopole ensemble and used in self-consistent determination of the flux tube size. The exact critical condition has been established, and applied to electric flux tube dissolution in sQGP system which interests us most. This leads to an estimate of total density of magnetic quasiparticles $n_{MQPs} \approx 4.4 \sim 6.6 fm^{-3}$ at $T \approx 1.3 T_c$, where lattice potentials indicate flux tube dissolution. These numbers are consistent with other studies using alternative ways to estimate magnetic density.

As mentioned in the introduction, this work is partly methodical in nature, ignoring electric quasiparticles which would lead to screening and termination of flux tubes. The next step we plan to do is obviously inclusion of both components and calculation of the static potentials. Hopefully, when one would consider an appropriate mixture of electric and magnetic quasiparticles, the lattice data on static potentials between electric and magnetic[7] charges would be explained.

In principle, one should go beyond that and calculate field distributions around static charges as well. Lattice studies can be extended to measure directly electric/magnetic fields at $T \sim T_c$: in fact the field profiles have been measured for flux tubes in vacuum before (see e.g. [34]).

Let us end with the following intriguing question. We focused above on electric flux in magnetic media, ignoring electric quasiparticles and possible dual phenomenon – a magnetic flux tube in an electric plasma. (We only mentioned their existence at low T high density regime, in a color superconductor.) Now, may somewhere along the electric-magnetic equilibrium line there be conditions supporting stable flux tubes of *both* types at the same time? It is known that confinement of both is impossible, but in a uncondensed plasma regime it may still be the case. A natural place to look for a QGP with intertwined electric and magnetic flux tubes is at T less or of the order of T_c, close to the place where three major phases – hadronic, color superconductor and QGP – meet. Although it is quite challenging task to get into this region using lattice gauge methods, the task is not hopeless.

[7] Those are given by the expectation value of the so called 't Hooft loop: we have not discussed them in this work.

Part II

The Electric Component of sQGP

Chapter 6

Bound States in sQGP

In the present and next Chapters, we will conduct a more careful examination of the more usually discussed degrees of freedom in $1-2T_c$, i.e. the quarks and gluons which we consider as the *electric* component of sQGP. These studies complement our investigation of the magnetic component in Part.I. to give a full picture of sQGP.

As we already demonstrated in the Introduction, in order to explain all the unusual features of QGP in $1-2T_c$ as exposed by RHIC discoveries and lattice results, a radically new picture of QGP at such temperatures has been developed, i.e. the *strongly coupled* QGP, or sQGP. It has been in particular pointed out in [19] that the interaction is strong enough to preserve the meson-like bound states up to about $T=2T_c\sim 300\,MeV$, (the temperature range corresponding to QGP created at RHIC), although in a strongly modified form. It was then pointed out in [21] that also multiple binary *colored* bound states should exist in the same T domain. Since QGP is a deconfined phase, there is nothing wrong with that, and the forces between say singlet $\bar{q}q$ and octet qg quasiparticle pairs are about the same[1]. Some of those states (charmonium) were observed on the lattice [32][33] at T up to about $2.5T_c$, while existence of most of these states, especially colored, still has to be checked.

In this chapter we report the first step toward the understanding of the *multibody* bound states [2].

[1] For potential-like forces the Casimir scaling gives 9/8 ratio, for string-like ones the ratio is just 1.

[2] The works in the present chapter are based on [22].

A Discussion Regarding the Binary Potential Used for Bound State Calculations

Apparently the binary potential is crucial for questions such as whether there would be bound states and how far they stay unmelted into the high T phase. For definiteness, we will use similar parameterized lattice-based interactions as in [21]. Below we discuss some of the details about the potential.

In the QCD vacuum, the potential for two color charges is traditionally written as a sum of a Coulomb and linear potential, dominating small and large distances, respectively. At $T > T_c$, by definition of the deconfined phase, the effective string tension vanishes and the potentials go to a constant at $r \to \infty$. But that does not mean that string-like field configurations of color field disappear right at T_c: as explained by Polyakov long ago [31], the string tension which vanishes at $T = T_c$ should be understood as the free energy, $F = V - TS$, while the string energy V and its entropy (related to the number of configurations) S are finite but cancelling each other. This picture of the deconfinement suggests by itself that the "mixed phase", at $T = T_c$, contains a lot of very long strings. It is natural to think then, that strong (although finite-range) interaction between the charges at $T > T_c$ is also related with strings.

Application of lattice-based binary potentials (actually free energy) derived for static quarks can be justified for near-zero binding states, in which motion is parametrically slow. This allows one to ignore magnetic and spin-related effects.

Still, in any application of such potentials to multi-body problems one has to decide the following fundamental question: what part of this interaction is (i) of a "potential-type" or (ii) of a "string-type". In the former case the potential energy of a many-body state is the sum over *all* pairs of particles, while in the latter only some pre-defined partners, "connected by a string" are allowed to interact. The issue is well known and was discussed in literature for baryons for decades. In Fig.6.1(upper) we show how two pictures look like, with strings in (a) ending at a string junction and in (b) connecting each pair of quarks directly.

The discussion above motivates us to consider interaction to be string-like in this sense. An additional reason for that is the especially simple multi-particle states appear, namely the *polymeric chains* made of repeated gluons with $\bar{q}$ and q at the ends, see Fig.6.1(c). (Recall that gluons have 2 color indices and can be viewed as 2 different color charges connected to two strings.)

Fortunately, in the case of colorless 3-quark states (baryons) it turns out that the string-based picture (a) and potential one (b) (with the Casimir factor 1/2 compared with meson potential) give very close results. This is also

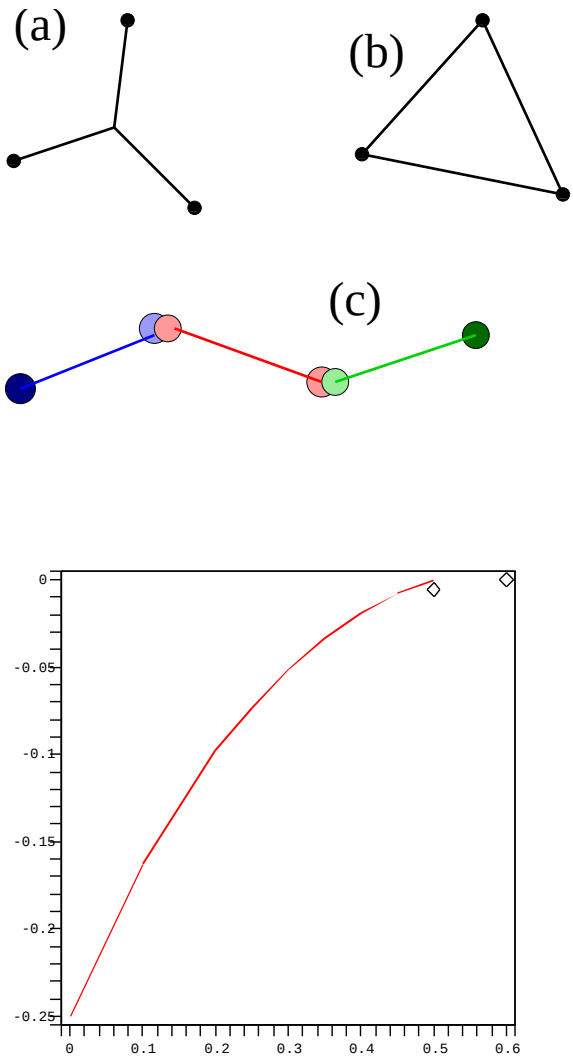

Figure 6.1: (upper) The interaction in baryons for "string-like" interaction (a) versus the "potential-like" interaction (b). The double circles with different colors (online) in (c) represent gluons, and it is an example of 4-chain $\bar{q}ggq$. (lower) Dependence of the binding energy on the Debye screening mass for the simple exponential trial functions. The units are explained in the text. Two diamond points indicate positions of the exact solutions.

the case in vacuum, as pointed out long ago in [92]. Also, this is supported by recent lattice study of free energy of static three quark systems[93] which found that the connected part of qqq-singlet free energies above T_c are decomposable into three qq-triplet (diquark) free energies for all distances. We will not discuss more complicated possible structures, like "polymerized" baryons with extra gluons or a network of chains, connected by color junctions.

6.1 The Coordinates and the Variational Procedure

We will denote particle coordinates by $\boldsymbol{x}_i, i = 1, n$ where the vector means a 3-d space and the index is for the particle number. Since the center of mass coordinate does not appear in the potential energy, the corresponding momentum is conserved and can be put to zero. It is a standard procedure to use some redefined coordinates which reduce the n-body problem to the (n-1) one: those coordinates would be denoted by $\boldsymbol{r}_i, i = 1, n$. Other notations we will use are

$$\boldsymbol{\partial}_i = \frac{\boldsymbol{\partial}}{\partial x_i}, \boldsymbol{D}_i = \frac{\boldsymbol{\partial}}{\partial r_i}, \tag{6.1}$$

related by $\boldsymbol{\partial}_i = \boldsymbol{D}_j M_{ji}$ where M is the coordinate matrix $r = Mx$ (namely $\boldsymbol{r}_j = M_{ji}\boldsymbol{x}_i$).

For reference and further comparison, let us give explicit form of the kinetic energy for (3-body) Jacobi coordinates

$$\boldsymbol{r}_1 = \boldsymbol{x}_1 - \boldsymbol{x}_2; \boldsymbol{r}_2 = (-1/2)\boldsymbol{x}_1 + (-1/2)\boldsymbol{x}_2 + \boldsymbol{x}_3; \\ \boldsymbol{r}_3 = (1/3)(\boldsymbol{x}_1 + \boldsymbol{x}_2 + \boldsymbol{x}_3) \tag{6.2}$$

$$\frac{1}{2M}(\boldsymbol{\partial}_i)^2|_{3Jacobi} = \frac{1}{2M}(2\boldsymbol{D}_1^2 + (3/2)\boldsymbol{D}_2^2 + (1/3)\boldsymbol{D}_3^2) \tag{6.3}$$

Note that it is a diagonal form avoiding coordinate mixing.

However for the polymer problem we found that more useful coordinates are "chain coordinates" defined by the following set of n coordinates

$$\boldsymbol{r}_1 = \boldsymbol{x}_2 - \boldsymbol{x}_1; ...\boldsymbol{r}_{n-1} = \boldsymbol{x}_n - \boldsymbol{x}_{n-1}; \boldsymbol{r}_n = \frac{1}{n}(\boldsymbol{x}_1 + ... + \boldsymbol{x}_n)$$

The corresponding kinetic energies for N-chains is

$$\frac{1}{2M}(\boldsymbol{\partial}_i)^2|_{N-chain} = \frac{1}{2M}(2\boldsymbol{D}_1^2 + 2\boldsymbol{D}_2^2 + \cdots + 2\boldsymbol{D}_{N-1}^2 + (1/N)\boldsymbol{D}_N^2 - 2\sum_{i=1}^{N-2}\boldsymbol{D}_i\boldsymbol{D}_{i+1}) \tag{6.4}$$

Although it is not diagonal, it is very simple instead, with the same "reduced mass" in each diagonal term[3] . Furthermore, in "string-like" approach the potential energy is very simple, just a sum over all "bonds" along the chain

$$E_{pot} = V(r_1) + ... + V(r_{n-1}) \tag{6.5}$$

Note that we dropped vector notation here: it means that only the lengths of these coordinates matter. Furthermore, all angular variables would not be important for the ground s-wave states to be discussed. If so, the wave function factorizes

$$\Psi(\boldsymbol{r}_1...\boldsymbol{r}_n) = \prod_{i=1}^{n-1}\psi(r_i) \tag{6.6}$$

and as a result the average value of the non-diagonal terms in the kinetic energy would vanish

$$< \boldsymbol{D}_i\boldsymbol{D}_j > |_{i\neq j} = 0 \tag{6.7}$$

Finally, as the diagonal terms have the same reduced mass as a 2-body problem, the problem obviously splits into (n-1) Schroedinger equations. This completes the proof that there is the same binding energy *per bond* (not per particle) as for mesonic states.. The binding *per particle* of course grows, doubling the binding in binary states as the length of the chain grows[4].

6.2 Mesons and Polymers in a Variational Approach

Since the 2-body problem and (as shown above) polymer chains can be easily solved numerically for any potential, and for relevant lattice-based potential it was already done in [21], the reader may be surprised why we discuss it here. We however found it instructive to start with a simple example, for which all

[3]This of course requires that all involved quasiparticles, the quark and the gluon ones, have the same mass, which is however approximately fulfilled by available lattice data.

[4]We again remind the reader that it only happened because in string-like approach one can ignore all the interactions between non-next-neighbors along the chains.

calculations and integrals are simple and can be done analytically

Let the potential be just a screened Coulomb (or Yukawa) potential

$$V = -\frac{\alpha\, e^{-M_D\, r}}{r} \tag{6.8}$$

and the trial function be as simple as possible, namely an exponential function

$$\psi = e^{-Ar} \tag{6.9}$$

The average energy is

$$\begin{aligned} < H > &= < (-1/2/M) * D^2 - (1/r/M) * D + V(r) > \\ &= 1/2\, \frac{A^2}{M} - \frac{4 * \alpha * A^3}{(M_D + 2A)^2} \end{aligned} \tag{6.10}$$

and it can be easily minimized in respect to parameter A. The results (for $\alpha = 1, M = 1/2$) as a function of M_D are plotted in Fig.6.1(lower).

Note that the simple exponential trial function we use is exact for a Coulomb problem ($M_D = 0$ case), but of course is not so for a screened potential. Although the energy may seem to be quite close to exact ones, obtained from numerical solution of the Schroedinger equation, true wave function is not particularly well reproduced by it as M_D grows. In particular, the curve in Fig.6.1(lower) crosses zero at its endpoint in a wrong manner: in fact the curve must have a horizontal tangent at the endpoint. Moreover, the critical value for the level disappearance predicted by exponential trial function

$$\frac{\alpha M}{M_D}|_{zerobinding} = 1 \tag{6.11}$$

is not at all accurate, as a comparison to exact behavior (indicated by two points in the right upper corner of Fig.6.1)(lower) changes the r.h.s. of (6.11) to a smaller value, 5/6.

One may ask whether it is possible to test the quality of the trial wave function without a knowledge of the exact result (as would be the case in multi-dimensional problems to be addressed in subsequent section). A well known observable for that is the so called "energy dispersion" variable, defined by

$$d =< H^2 > - < H >^2 \tag{6.12}$$

If the trial wave function is an eigenvector, d=0, otherwise it characterizes the quality of the approximation. In Fig.6.2(upper) we show how it depends on M_D. As expected, it is zero for pure Coulomb problem ($M_D = 0$) but strongly

grows with M_D, indicating loss of quality of the approximation. Nevertheless, we emphasize that while this energy dispersion is quite sensitive to how close the trial function is to true solution, the energy itself is much less sensitive to the details of the wave function shape.

Now we turn to a realistic variational approach for the two-body bonds in mesons and polymers, using a parameterized temperature-dependent potential extracted from lattice data [**?**]

$$V(T,r) = \; - \; (\frac{4}{3r} + \frac{8T}{3}) \frac{e^{-2Tr}}{log(1+3T)} \frac{4T}{r(1+3T)} \frac{e^{-2Tr}}{(log(1+3T))^2} \quad (6.13)$$

Note that we have scaled all dimensional quantities with proper powers of T_c, namely T gives T/T_c, r means rT_c, and so on. We will keep these units throughout present paper. Plots of the potential at different temperatures are shown in Fig.6.2(lower). At very short distance this potential goes as a Coulomb (as expected from short-range one-gluon exchange interaction) while at very large distance it is a screened Coulomb potential which damps so fast as if it is almost vanishing. The log term is simplified compared to the original form in [21] where it was $log(1/r + 3T)$, the parameterization consistent with the asymptotic freedom at small r.

Note that this is basically for color singlet $\bar{q} - q$ (and for color octet $g - g$ approximately), so we need to add appropriate overall coefficients for other channels like diquark.

According to the features of the above potential, we employ a trial wave function as following (with $\boldsymbol{r}$ the 2-body relative coordinate)

$$\phi(r) = exp{-Ar} - \frac{C^2 r^2}{(C^2 r^2 + 1)}(B - A)r - \frac{1}{2} log(C^2 r^2 + 1) \quad (6.14)$$

It has the asymptotic forms to be

$$r \to 0 \; : \; \phi \to e^{-A\,r} r \to \infty \; : \; \phi \to \frac{e^{-B\,r}}{C\,r} \quad (6.15)$$

Here the parameter C controls the interpolation between the short distance Coulomb behavior and the long distance free particle solution. All the three parameters have the same unit for which we use T_c.

With the (temperature-dependent) potential and trial function at hand, we then find the binding energy at different temperature by minimizing energy (kinetic plus potential energy) according to the three variational parameters A, B, C. A non-relativistic form for kinetic part is used, since the color-charged quasiparticles, both quarks and gluons, are found by lattice simulations to be

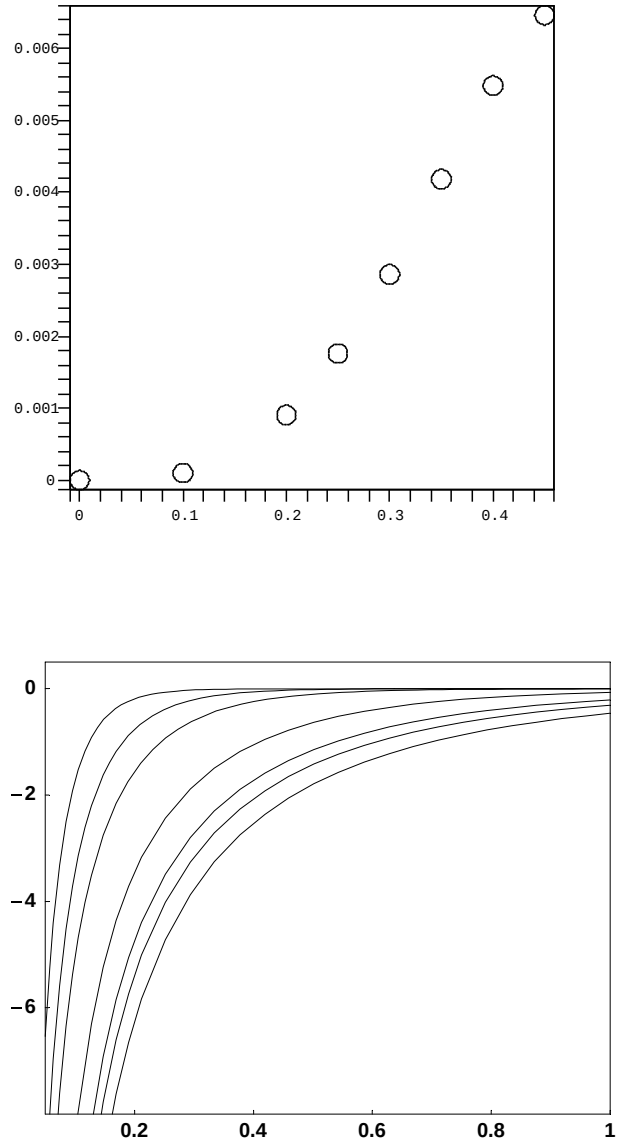

Figure 6.2: (upper) Dependence of the "energy dispersion" variable d on the Debye screening mass M_D, for the simple exponential trial functions. (lower) The static potentials $V(T, r)$ (in unit T_c) as a function of the distance r (in unit $1/T_c$). The values of temperature used are $T = 1, 1.2, 1.4, 2, 4, 6, 10\, T_c$ for curves from right to left.

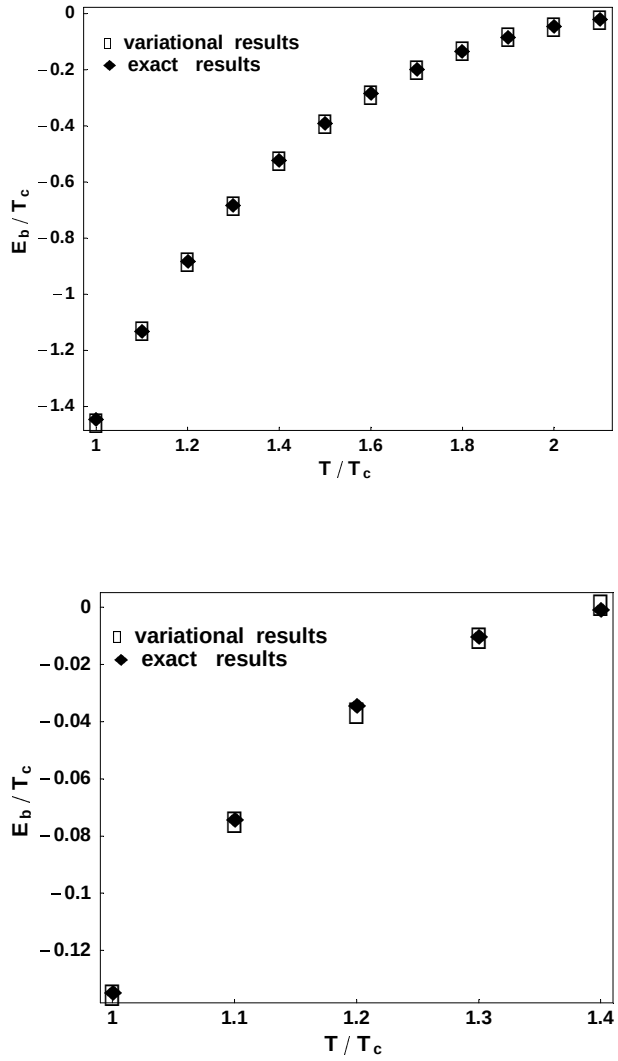

Figure 6.3: Dependence of the meson (upper) and diquark (lower) binding energy on the temperature. The units are in T_c.

rather heavy at temperatures not so high from T_c, for which we use the same constant value $m^* = 800MeV$ in our calculation for simplicity. We employed the well-known Metropolis Monte Carlo[94] to evaluate the energy. The results are shown in Fig.6.3(upper). We also plot the exact energies obtained by numerically solving the Schroedinger equations for comparison. As can be seen, the variational results coincide perfectly with the exact results. The energy dispersions are of order 0.01 (not vanishingly small), but as we emphasized before and shown here, the energy itself could still be very accurately evaluated. For the optimal values of wave function parameters, A decreases from 3.125 to 2.25 and B from 3.125 to 0.5 with increasing temperature, and C keeps between 0.5-1 to which the energies are less sensitive.

The binding energy E_b is greater than temperature for 1-1.1 T_c and comparable with temperature up to 1.6 $T_c(|E_b|/T$ about 0.26, and $e^{0.26} = 1.3)$. Naively following a $e^{-E_b/T}$ (at T_c as high as 4.3) factor argument we may say the formation of meson-like bonds in this T-region is quite favored. Now recalling the proof in previous section, a polymer chain with N elements will have a binding energy $(N-1)E_b$ (E_b per bond), and further more, the long chains have much more statistical degeneracies (according to vast options arranging intermediate gluons' quantum numbers), so we expect abundance of polymer chains at temperatures just above T_c. And this, as we will suggest, may dramatically contribute to jet quenching as well as transport properties.

6.3 Baryons at $T > Tc$

After consideration of meson-like structures, it is of course natural and interesting to address the question of possible baryonic bound states above T_c. While lattice calculation found mesonic bound states above T_c[32][33], there is no available information about baryon up till now. Also it is very important to see the role of baryons in the deconfined phase of QCD. For example, baryons carry conserved quantum numbers like B, S which may be combined to give useful experimental/lattice signal[95] and contribute more to study of thermodynamics at non-zero chemical potential[77][46]. So in this section we conduct a variational approach for baryons in similar way as was used in the past to study baryons in vacuum[92].

We consider baryons(anti-baryons) as closed 3-chains of quarks(anti-quarks), which contains 3 pairs of diquarks(anti-diquarks). Thus to study baryons, we first start with diquarks at $T \geq T_c$. Diquarks in the deconfined phase of QCD are of their own importance also. For the diquark channel, the mutual interaction coupling should be one half the quark-anti-quark channel, thus we

adjust the potential (6.13) by a coefficient $C/C_{\bar{q}q} = 1/2$ to use it for diquark bound states. We use the same trial function (6.14) as in meson case, and then minimize energy according to A, B, C. In Fig.6.3(lower) we plot the diquark binding energy as a function of temperature. The exact numeric results are also presented to compare and justify our variational approach. Diquark states are much more shallowly bound than meson and thus more easily melted.

For baryons, we construct the trial wave function on the basis of the three diquark pairs. Since we're only interested in the ground state, it is reasonable to use a totally symmetric s-wave spatial configuration. The color wave function should still be the singlet (then antisymmetric among the 3 quarks) to guarantee the attractive interaction, but for spin and flavor part, the only constraint is to be symmetric and there are a lot of ways to arrange it (increasing statistical degeneracies). Particularly, we want emphasize that very different from constructing baryon in vacuum, now s quark is more or less the same as u, d quarks, since its current mass, of the order of T_c is much less than quasiparticle mass and the current mass splitting is now unimportant. So we write down the following

$$\psi(\boldsymbol{x}_1, \boldsymbol{x}_2, \boldsymbol{x}_3) = \phi(r_{12})\phi(r_{23})\phi(r_{31}) \tag{6.16}$$

Here $\phi(r)$ is from (6.14) which has been used for meson and diquark states, and $\boldsymbol{r}_{ij} = \boldsymbol{x}_i - \boldsymbol{x}_j$. Again we minimize energy according to the variational parameters A, B, C. Note now for this 3-body object, we have two kinetic energy terms according to the first two in (6.3) (one term with reduced mass factor 1/2 and the other 2/3), while for potential energy we need count for each pair of quarks, namely three potential energy terms. Hence we expect that baryons are more compact and deeply bound than diquarks both because of heavier reduced mass and due to more potential energy, as can be seen in Fig.6.4(upper). The binding energy is slightly greater than temperature at T_c and comparable up to 1.3 T_c, which means the baryons (and anti-baryons) should play some role for temperatures not too high above T_c. As far as we know, this point is noticed and demonstrated for the first time.

Having studied baryons, we go a step further and include the simplest closed 3-chain structure above T_c, namely ggg, a color-singlet channel in which the three gluons mutually interact in similar way as three quarks in a baryon. In a string picture, there is a string between each pair, so the potential should be the same as in a meson (twice that for diquarks). Again we use the 3-body trial wave-function (6.16) and minimize energy according to A, B, C. The results are shown in Fig.6.4(lower). It is bound up to rather high temperature of about 2.6 T_c. The binding energy at T_c is as high as 7.64 T_c, and the size shrinks to only about 0.3 fm. Since we only use static potentials, without any

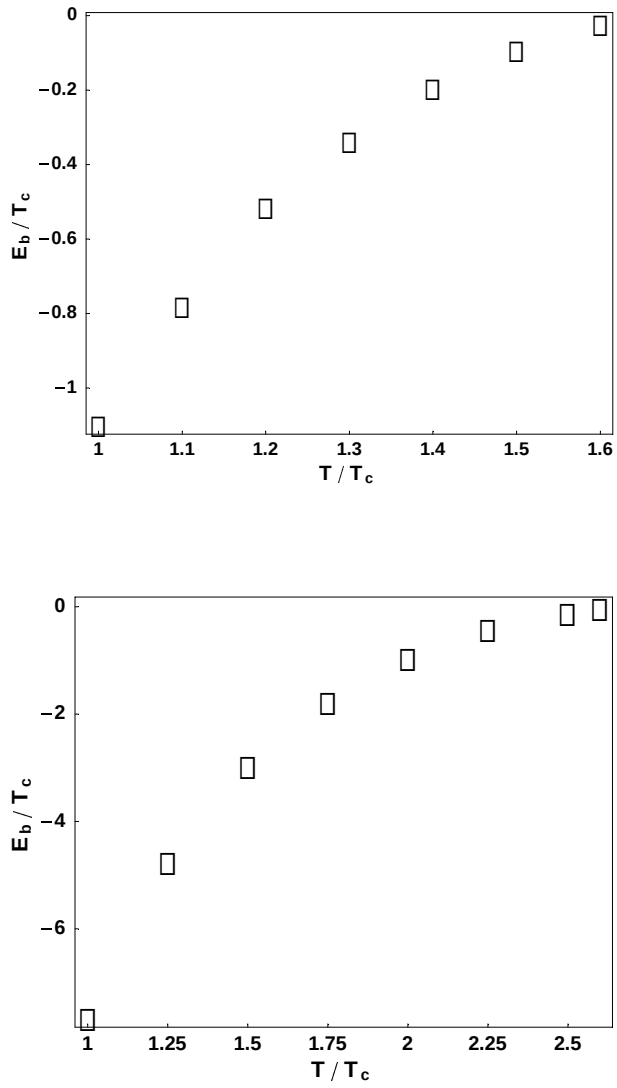

Figure 6.4: Dependence of the baryon (upper) and three gluon (lower) binding energy on the temperature. The units are in T_c.

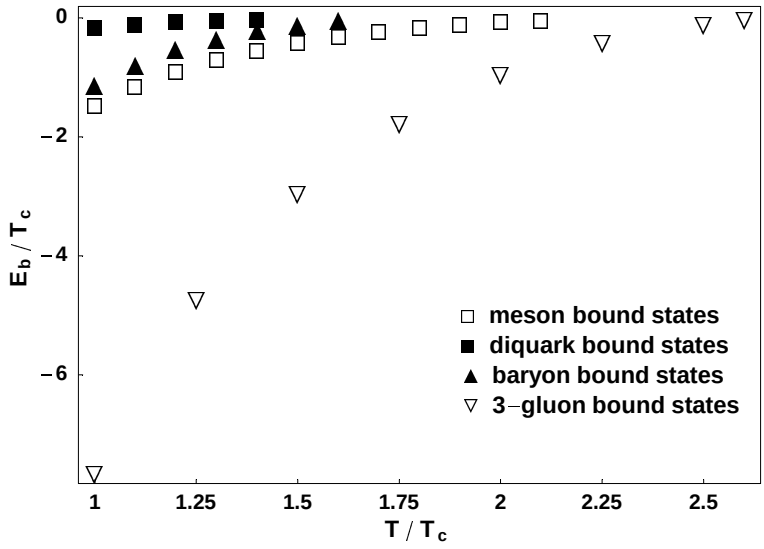

Figure 6.5: Dependence of various states' binding energy on the temperature. The units are in T_c.

relativistic corrections, we warn the reader that close to T_c the ggg binding (the only one!) becomes too large to be reliably evaluated inside the approximations made[5].

6.4 Summary and Discussion

To sum up, three *multi-body* bound states have been studied via variational approach: (i) "polymer chains" of the type $\bar{q}gg..gq$; (ii) baryons (qqq); (iii) closed (3-)chains of gluons (ggg). For the chains (i) we have proved that they have the same binding energy per bond as mesonic states and thus form in the same temperature range as mesonic states. We have established the binding energies and survival T-ranges for all these three structures. All the results are summarized in Fig.6.5 and Table.6.1. We conclude that between temperature region 1-1.5 T_c the existence of all these multi-body bound states is not only possible but very robust.

Before we go forward with a general discussion, let us try to summarize the proposed scenario as a single picture, see Fig.6.6. From relatively short string-like configuration of color fields at low T, fig (a), one moves to longer strings (b) at the critical point [31]. New is picture (c) which depicts "polymeric

[5]On top of relativistic effects we ignored, the simplification of the potential $log(1/r + 3T) \to log(1 + 3T)$ used above also affects binding close to T_c.

Table 6.1: Summary of different bound states at $T > T_c$ studied in this paper. The column $C/C_{\bar{q}q}$ gives the relative potential strengths used in calculation, E_b means the binding energy, and T_m refers to the melting temperatures for different structures.

structure	-body	$C/C_{\bar{q}q}$	E_b/T_c at T_c	T_m
$\bar{q}q$	2	1	-1.45	2.1
$\bar{q}g\cdots gq$ (polymer chain)	N	1	-1.45∗(N-1)	2.1
ggg (closed chain)	3	1	-7.64	2.6
qq / $\bar{q}\bar{q}$	2	1/2	-0.13	1.4
qqq / $\bar{q}\bar{q}\bar{q}$ (closed chain)	3	1/2	-1.10	1.6

chains" considered in this work, significant at $T = (1 - 1.5)T_c$. Eventually, at high T, one goes into (d) with independent quark and gluon quasiparticles, neutralized by isotropic Debye clouds.

We have not studied in this work neither more complicated states, such as a hybrid of baryons and polymers or a network of chains connected by color junctions, nor have we attempted to evaluate the possible role of polymers/baryons in thermodynamical[6] and transport properties of sQGP (to be done elsewhere).

The contribution of polymers into partition function can be easily evaluated via a geometric series: the resulting enhancement factor, correcting the contribution of the $\bar{q}q$ mesonic states to those with any number of intermediate gluons $\bar{q}g...gq$, is

$$f_{polymers} = \frac{1}{1 - 6exp[(|\delta E| - M_g)/T]} \tag{6.17}$$

where 6 is the color and spin degeneracy added by each link. If one takes literally the bond binding we found, up to $1.4T_c$, and the effective gluon mass

[6]The only calculation we have done in [46] deals with baryonic susceptibilities – up to the 6-th derivatives over chemical potential – studied recently on the lattice by the UK-Bielefeld collaboration [77].

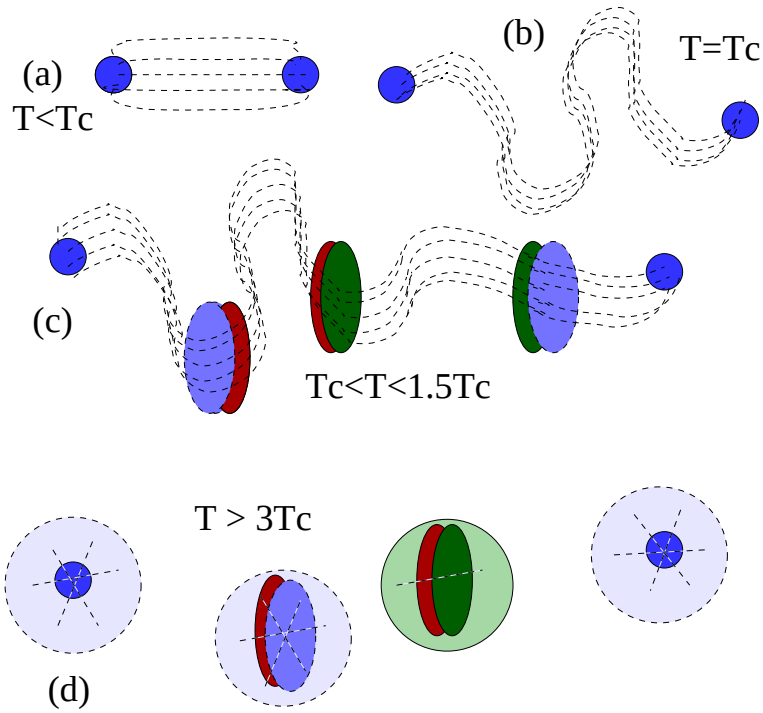

Figure 6.6: A schematic picture of the distribution of color fields, at different temperatures. Single color circles are quarks, bi-colored ovals are gluons.

we used, one finds that even at $T = T_c$ this factor only reaches about 1.2, and rapidly decreases at higher T. The corresponding enhancement factor for baryons is a cube of that, but baryons themselves are a small effect. So, the multi-body states we discussed above provide a few percent corrections into thermal properties of sQGP [7].

The reader may thus ask why had we studied those states at all. One reason is the baryons dominate the high density QGP, at large checmical potential.Another reason is we hope "polymers" may be important for *transport properties* such as jet quenching, which we will study in the future.

[7]However if some missing effects would increase this binding by about a factor of two, the zero in the denominator can be reached, forcing total "polymerization" of matter. We think it is unlikely to happen.

Chapter 7

Quarks, Diquarks and Baryons in sQGP as Diagnosed by Baryonic Susceptibilities

In this Chapter, we examine one particular thermodynamical observable that has been accurately determined recently on lattice: the baryonic susceptibilities. In particular, we extract from these lattice data important information about the baryon-number-carrying states in the $1-2$, namely the quarks, diquarks and baryons in sQGP [1].

To put the discussion below into proper perspective, we repeat one argument from [21] which says that there should be 3 categories of bound states, in decreasing robustness: (i) glueballs, (ii) $(qg)_3$ and mesons $\bar{q}q$; and (iii) $(qg)_6$, diquarks and baryons. If the strength of the effective potential in $\bar{q}q$ states is counted as 1, the relative color Casimirs for categories (i),(ii) and (iii) are $9/4$, $9/8 \sim 1$ and $\approx 1/2$, respectively. In the previous Chapter we have extended the same approach to some many-body states. We found new 3-gluon configuration ggg belonging to category (i), the polymeric chains $\bar{q}.g.g...gq$ of the category (ii) and diquarks and baryons in category (iii).

The last two are the baryon number carrying states we will discuss in this Chapter. Since these states belong to the *third*, most weakly bound category, they are naturally most vulnerable to uncertainties of the potential and their existence can be questioned. Besides, these states are relatively heavy: such states have not been included in [21] in the calculation of thermodynamic pressure.

The reason we will discuss them now is because they are more important at increasing baryonic chemical potential μ. Alternative way to look at the same

[1] The works in the present chapter are based on [46].

thing is to consider higher derivatives over μ at $\mu = 0$: this way the role of such states is enhanced due to powers of their baryon number. At some point the diquarks and baryons should become noticeable in these quantities even if their role in pressure is small: and this is precisely what we think happened in the lattice data of the UK-Bielefeld collaboration (UKB) [77], especially in susceptibilities with 4 and 6 derivatives.

Definition of the Baryonic Susceptibilities and its Values below T_c

From now on we will concentrate on the so called baryonic susceptibilities part of the free energy, which can be singled out via derivatives over quark chemical potentials $\mu_q = (\mu_u + \mu_d)/2$ and $\mu_I = (\mu_u - \mu_d)/2$ calculated recently by the UKB. They use it in a context of Taylor expansion of the thermodynamical quantities in powers of baryonic chemical potential μ/T[2] up to the order $O(\mu^6)$ of 2-flavor QCD, but we will not discuss this expansion per se and concentrate on (T-dependent) susceptibilities of the kind[3]:

$$d_n(T) = \frac{\partial^n (p/T^4)}{\partial(\mu/T)^n}\bigg|_{\mu=0} = n! c_n(T) \tag{7.1}$$

for $n = 2, 4, 6$. (The odd ones vanish at $\mu = 0$ by symmetry.) These data are shown in Fig.7.1 and also below. The UKB also studied what they called isospin susceptibilities defined as

$$d^I_n(T) = \frac{\partial^n (p/T^4)}{\partial(\mu/T)^{n-2}\partial(\mu_I/T)^2}\bigg|_{\mu=\mu_I=0} = n! c^I_n(T) \tag{7.2}$$

and in a flavor diagonal-non-diagonal language there are

$$d^{uu}_n = (d_n + d^I_n)/4\,,\; d^{ud}_n = (d_n - d^I_n)/4\;. \tag{7.3}$$

Let us also mention another recent independent lattice studies on susceptibilities of 2-flavor QCD in [96], where they defined so-called nonlinear susceptibilities(NLS)

$$\chi_{n_u,n_d} = \frac{\partial^{(n_u+n_d)} p}{\partial \mu_u^{n_u} \partial \mu_d^{n_d}} \tag{7.4}$$

[2]We follow notations used in this work where μ is the chemical potential per quark, not per baryon. Thus the associated charge is $B = 1$ for a quark, $B = 2$ for a diquark and $B = 3$ for a baryon.

[3]Since we would not discuss any Taylor series in this work, we would prefer to leave out the factorials and thus discuss susceptibilities d_n defined without them, not c_n.

and evaluated their values on lattice. To see the connection between these two approaches, we give the following relations

$$d_n^{uu} = T^{n-4} \sum_{l=0}^{n-2} C_{n-2}^l [\chi_{l+2,n-l-2} + \chi_{l,n-l}]/2 \,, \tag{7.5}$$

and

$$d_n^{ud} = T^{n-4} \sum_{l=0}^{n-2} C_{n-2}^l \chi_{l+1,n-l-1} \,. \tag{7.6}$$

While the two approaches are very closely related, their numerical results, however, are not quantitatively comparable, partly because they have used very different mass setup in the lattice calculation. We nevertheless emphasize that in a qualitative view both of them have found very similar and interesting patterns in those susceptibilities, especially for the 4th and the 6th, which are the central issues to be addressed in this paper.

To set the stage, we start with the hadronic phase below T_c. Here the relevant states are only the baryons with the baryon number (per quark) 3. Their spectrum is known at $T = 0$ experimentally, and thus an obvious question is: Can a simple resonance gas of known baryons explain the behavior of these susceptibilities below T_c? Indeed it is the case, as shown by the dotted curves in Fig.7.1 (obtained by including contributions of nucleon states from N(940) to N(1675) and Δ states from $\Delta(1232)$ to $\Delta(1700)$, for two-flavor theory one should not include strange baryons). No $T-$ or $\mu-$ dependence of these masses is assumed, nor do we take into account the fact that lattice is dealing with non-massive quarks[4]: tuning these will shift the curves down a bit, making the agreement even better. So the susceptibilities in the hadronic phase, $T < T_c$, can be described by the usual resonance gas of baryons.

A Discussion about Naive Free Gas Model of Quark Quasiparticles

The main issue to be discussed is what these lattice data actually tell us about the nature of baryonic states *above* T_c, and whether one can describe them with sQGP model or as well with some other model.

Before we proceed to the argumentation in literature, let us remind standard thermodynamical expressions for massive fermions, which can be put in

[4]In fact the input quark mass in these calculations is $0.4T$.

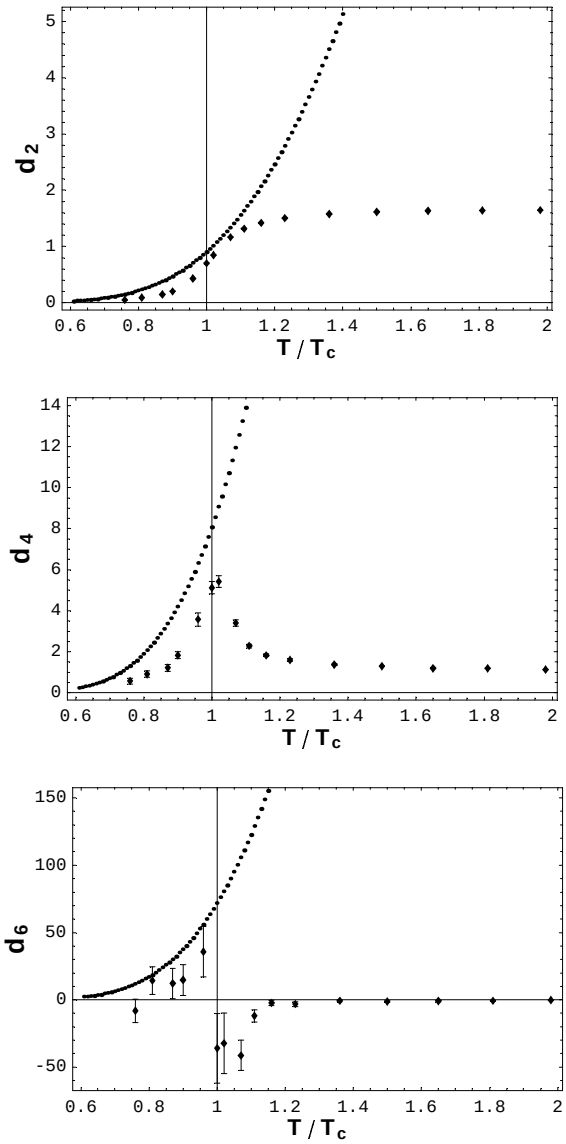

Figure 7.1: The dotted lines correspond to a gas of baryonic resonances, the points with error bars are the susceptibilities $d_2(T), d_4(T), d_6(T)$ from lattice data (after removal of factorials in $c_{2,4,6}$).

the following well known form

$$\frac{p}{T^4} = N\frac{M^2}{2\pi^2 T^2}\sum_{l=1}^{\infty}\left[\frac{(-)^{l+1}}{l^2}\quad\left(e^{lB\mu/T}\right.\right.$$
$$\left.\left.+e^{-lB\mu/T}\right)K_2(lM/T)\right] \tag{7.7}$$

where B, M is the baryon number of the corresponding particle and its mass, N is the statistical weight and K_2 is the Bessel function.[5] This form is very convenient for taking derivatives over μ, for example the first derivative, the baryon density is

$$\begin{aligned}\frac{n_B}{T^3} = &\quad NB\frac{M^2}{2\pi^2 T^2}\sum_{l=1}^{\infty}\left[\frac{(-)^{l+1}}{l}\left(e^{lB\mu/T}\right.\right.\\ &\left.\left.-e^{-lB\mu/T}\right)K_2(lM/T)\right]\\ = &\quad NB\,\mathcal{N}[B\mu/T, M/T]\end{aligned} \tag{7.8}$$

where the function $\mathcal{N}[x,y]$ is defined by these series. Note at this point we don't really consider mass as depending on μ so no extra derivatives against M appear.

In a number of talks Karsch (and also a paper [97]) has presented what we would refer to as a "naive" argument: the subsequent ratios

$$d_{n+2}/d_n \approx < B^2 > \tag{7.9}$$

are directly related to the squared baryon number of the constituents. The argument goes as follows: (a) For massive particles with $M >> T$ one can use the so called Boltzmann approximation, keeping only the first term in the sum above; (b) after that the $\mu-$ dependence factorizes, and thus each two derivatives over μ restore the same expression, modulo the factor B^2. In the matter dominated by quark quasiparticles, or qg bound states, the r.h.s. would be 1, but it would instead be 4 or 9 for matter dominated by diquarks or baryons, respectively. The measured ratio d_4/d_2 is ~ 10 at $T < T_c$ but at $T > T_c$ it rapidly drops and becomes close to 1. Comparing it to the formula above Karsch concluded that at $T > T_c$ matter is a gas of some $B = 1$ objects, while the contribution of the $B = 2$ diquarks is strongly restricted.

[5] If there are more than one species of particle we then sum over different species. Yet there will be particular concern when dealing with quasiparticles instead of particles where some background term may arise in the pressure, as will be discussed in later section.

But if one looks closer at this argument, one finds it missing a lot of effects that should be there as well. For example, the next similar ratio d_6/d_4 above T_c is nowhere close to 1 but is in fact a large negative number ~ -10 which cannot be interpreted as a B^2 of anything.

Furthermore, the idea that one can keep only the main term in the sum so that the μ and T dependence can factorize, must be wrong by itself. The T-dependence of $d_2(T)$, $d_4(T)$ and $d_6(T)$ is not at all similar: while $d_2(T)$ resembles the behavior of the pressure itself and can easily be interpreted as a transition from hadron to quark gas, the next one $d_4(T)$ has a sharp maximum near T_c, with even more complicated "wiggle" in the $d_6(T)$.

Another perspective on that issue can be made if one converts baryon number and isospin susceptibilities into flavor-diagonal (uu or dd) and flavor non-diagonal ud susceptibilities. The lattice data show that the second flavor-mixing derivatives are small[6] $d_2^{ud}/d_2^{uu} << 1$, but similar ratios for higher derivatives n=4,6 are not small $d_n^{ud}/d_n^{uu} \sim 1/2$.

Does it imply that the quark gas model is also inadequate and should be excluded as well as the "bound state" gas? Or, if the argument is wrong, what exactly is missing?

(i) Even if the Boltzmann approximation (keeping the first term in sum in (7.7)) may be good for pressure, it still fails for higher susceptibilities because the l-th term has $l\mu$ in the exponent, and subsequent differentiation their role grows as l^n. By the time one comes to the sixth derivative, these terms start canceling each other. In physics terms, this is a form of Fermi blocking effect not included in the simple Boltzmann approximation.

(ii) The second to recognize is the fact that quasiparticles are not particles and their effective masses depend on matter parameters, such as T and especially μ. Subsequent differentiation of this effective mass over μ would add powers of derivatives like

$$M'' = \frac{\partial^2 M}{\partial \mu^2}(T, \mu = 0) \tag{7.10}$$

to susceptibilities and to their ratios such as (7.9). Provided those are large enough, they may completely invalidate the naive interpretation of those ratios as baryon number squared. This was already pointed out by Bluhm, Kempfer and Soff [98], and we will refer to it below as the "BKS effect". The same is true for bound states such as baryons, and similar derivatives of their masses $M_B''(T)$ would play an important role below.

(iii) the contribution of diquarks has been grossly overestimated, while the

[6] This is also the main point of the paper [95].

contribution of baryons was not discussed at all. We will show below that it may naturally explain the features seen in higher derivatives.

This Chapter is organized as follows. In section 7.1 we will start with an "unconstrained" quark gas model, and will use the lattice data to extract the quasiparticle mass together with its dependence on matter, $M(T,\mu)$. We would not need to rely on perturbative arguments used by BKS [98] (since even their own fit leads to rather strong coupling at $T \approx T_c$). Furthermore, we will conjecture possible relation between the $T-$ and $\mu-$ dependences due to known shape of the phase boundary on the phase diagram. In section 7.2 we will further impose a number of constraints on quark mass, from other lattice data and also from confinement, a condition that there should not be any colored degrees of freedom at $T < T_c$. We will conclude that these constraints basically make it impossible to ascribe the observed features of the data to the BKS effect. After that we will proceed to section 7.3 in which we will discuss the contribution of diquark and baryons: here we will find good fits to the data satisfying all the needed constraints and nicely joining the baryon gas picture below T_c.

7.1 Model I: A Quark Gas with an Unconstrained Mass $M(T,\mu)$

The idea to use thermodynamical quantities calculated on the lattice to fit the mass parameters of quasiparticles is by itself quite old. For example, Levai and Heinz [99] have used the data on $p(T)$ for determination of quark and gluon effective masses $M(T)$[7].

One well known problem with quasiparticle gas models is that the derivatives over T and μ upset thermodynamical consistency between gas-like expressions for different thermodynamical quantities. Only one of them can be assumed to have a simple additive form over quasiparticles: then there is no freedom left and all other quantities can be calculated from it by thermodynamics. Thus only one "primary" expression can be additive, while others will have extra "derivative" terms complementing simple gas formulae.

Following conventions of the BKS paper, we will use as such "primary" expression that for the baryon number density (7.8). The expressions for pressure and energy density would then be corrected by some T,μ-dependent

[7]It was not as direct as our approach below, because one cannot get 2 functions out of one without assumptions.

"bag terms". Higher derivatives terms d_n will be calculated by differentiating (7.8) $n-1$ times. To be more specific, we explicitly give the baryon number density for this quark gas model

$$\frac{n_B}{T^3} = \frac{\partial(p/T^4)}{\partial(\mu/T)} = \frac{g}{2\pi^2}\int dx x^2\, n\,[F(\epsilon - n\tilde{\mu}) - F(\epsilon + n\tilde{\mu})] \tag{7.11}$$

Here $g = N_s * N_c * N_f = 12$ is the degeneracy factor for quarks in the two-flavor case, n is the baryon quantum number of quark which is defined here to be $n = 1$ by setting μ to be the quark chemical potential. $\tilde{\mu} = \mu/T$ is made to be dimensionless, and $\epsilon = \sqrt{x^2 + \tilde{m}}$ with $\tilde{m} = M/T$. And finally we have introduced Fermi distribution function $F(y) = \frac{1}{e^y+1}$. Starting from (7.11) the explicit formulae for d_2, d_4, d_6 are given to be:

$$d_2 = \left.\frac{\partial(n_B/T^3)}{\partial\tilde{\mu}}\right|_{\mu=0} = -\frac{2g}{2\pi^2}\int dx x^2\, n^2 F^{(1)}(\epsilon_0) \tag{7.12}$$

$$\begin{aligned} d_4 &= \left.\frac{\partial^3(n_B/T^3)}{\partial\tilde{\mu}^3}\right|_{\mu=0} \\ &= -\frac{2g}{2\pi^2}\int dx x^2 \Big[n^4 F^{(3)}(\epsilon_0) \\ &\qquad +3n^2\, F^{(2)}(\epsilon_0)\,\frac{\tilde{m}_0}{\epsilon_0}\,\big(\frac{\partial^2\tilde{m}}{\partial\tilde{\mu}^2}\big|_{\mu=0}\big)\Big] \end{aligned} \tag{7.13}$$

$$\begin{aligned} d_6 &= \left.\frac{\partial^5(n_B/T^3)}{\partial\tilde{\mu}^5}\right|_{\mu=0} \\ &= -\frac{2g}{2\pi^2}\int dx x^2 \Big[n^6 F^{(5)}(\epsilon_0) \\ &\qquad +10n^4\, F^{(4)}(\epsilon_0)\,\frac{\tilde{m}_0}{\epsilon_0}\,\big(\frac{\partial^2\tilde{m}}{\partial\tilde{\mu}^2}\big|_{\mu=0}\big) \\ &\qquad +15n^2\, F^{(3)}(\epsilon_0)\,\frac{\tilde{m}_0^2}{\epsilon_0^2}\,\big(\frac{\partial^2\tilde{m}}{\partial\tilde{\mu}^2}\big|_{\mu=0}\big)^2 \\ &\qquad +5n^2\, F^{(2)}(\epsilon_0)\left(\frac{\tilde{m}_0}{\epsilon_0}\,\big(\frac{\partial^4\tilde{m}}{\partial\tilde{\mu}^4}\big|_{\mu=0}\big)\right. \\ &\qquad \left.+\frac{3x^2}{x^2+{\tilde{m}_0}^2}\big(\frac{\partial^2\tilde{m}}{\partial\tilde{\mu}^2}\big|_{\mu=0}\big)^2\right)\Big] \end{aligned} \tag{7.14}$$

In the above equations we have used $\epsilon_0 = \sqrt{x^2 + \tilde{m_0}^2}$ and $\tilde{m}_0(T) = M(T, \mu = 0)/T$, and also $F^{(i)}(y)$ means the ith derivative of the function $F(y)$.

The model used in the BKS paper assumes some Hard Thermal Loop based perturbative form for the T, μ-dependent mass with the coupling $g^2(T, \mu)$ running in a complicated fashion fitted to reproduce the susceptibilities we discuss in this work. However, we do not see why any assumptions about the mass dependence are actually needed[8] at this point.

We thus suggest a generalization of what was done in [98]. Assuming a simple ideal gas model of quark quasiparticles, one has their mass to be the only input needed. With the lattice data on $d_2(T)$, $d_4(T)$ and $d_6(T)$ used as input, one can simply solve for the three functions of T which would ideally fit them: we have chosen those to be: (i) the quark mass $M(T, \mu = 0)$; and its two lowest non-zero[9] derivatives over μ (ii) $M'' = \frac{\partial^2 M}{\partial \mu^2}(T, \mu = 0)$ and (iii) $M'''' = \frac{\partial^4 M}{\partial \mu^4}(T, \mu = 0)$. With these at hand, of course, we are able to develop the Taylor's expansion for quark mass as a function of $|\frac{\mu}{T}| < 1$:

$$M(T, \frac{\mu}{T}) = M(T, \mu = 0) \quad + \frac{1}{2!}\frac{\partial^2 M}{\partial \mu^2}(T, \mu = 0) \cdot (\frac{\mu}{T})^2 + \frac{1}{4!}\frac{\partial^4 M}{\partial \mu^4}(T, \mu = 0)(\frac{\mu}{T})^4 \tag{7.15}$$

The procedure is iterative: First we used $c_2(T)$ data to solve for the mass $\tilde{m}_0$ as unknown. Then we go to c_4, the equation of which includes both $\tilde{m}_0$ and $\frac{\partial^2 \tilde{m}}{\partial \tilde{\mu}^2}\big|_{\mu=0}$, but since we have already solved $\tilde{m}_0$ from c_2 now the only unknown term is $\frac{\partial^2 \tilde{m}}{\partial \tilde{\mu}^2}\big|_{\mu=0}$, which could be solved out from lattice results of c_4. finally we can obtain $\frac{\partial^4 \tilde{m}}{\partial \tilde{\mu}^4}\big|_{\mu=0}$ from c_6 with $\tilde{m}_0$ and $\frac{\partial^2 \tilde{m}}{\partial \tilde{\mu}^2}\big|_{\mu=0}$ already being solved from c_2 and c_4. The results for these three functions are shown in Fig.7.2. (The error bars in $\tilde{m}_0$ are determined from uncertainty in c_2. While for $\frac{\partial^2 \tilde{m}}{\partial \tilde{\mu}^2}\big|_{\mu=0}$ the errors should come from both c_4 and $\tilde{m}_0$, the error bars in the figure only include those from c_4, and also for $\frac{\partial^4 \tilde{m}}{\partial \tilde{\mu}^4}\big|_{\mu=0}$ the error bars solely include that originated from c_6.)

As an independent check, we have also extracted the same three quantities, $M(T, \mu = 0)$, $\frac{\partial^2 M}{\partial \mu^2}(T, \mu = 0)$ and $\frac{\partial^4 M}{\partial \mu^4}(T, \mu = 0)$ from the lattice data set for $c_2^I(T)$, $c_4^I(T)$ and $c_6^I(T)$ from [77] by the same strategy (but starting with isospin densities).

[8] There is of course no reason to trust any perturbative formula near T_c at all, where the coupling becomes as strong as it was found by BKS themselves.

[9] The quasiparticle masses and other quantities obviously can depends only quadratically on μ because of $\mu \to -\mu$ symmetry based on CP invariance.

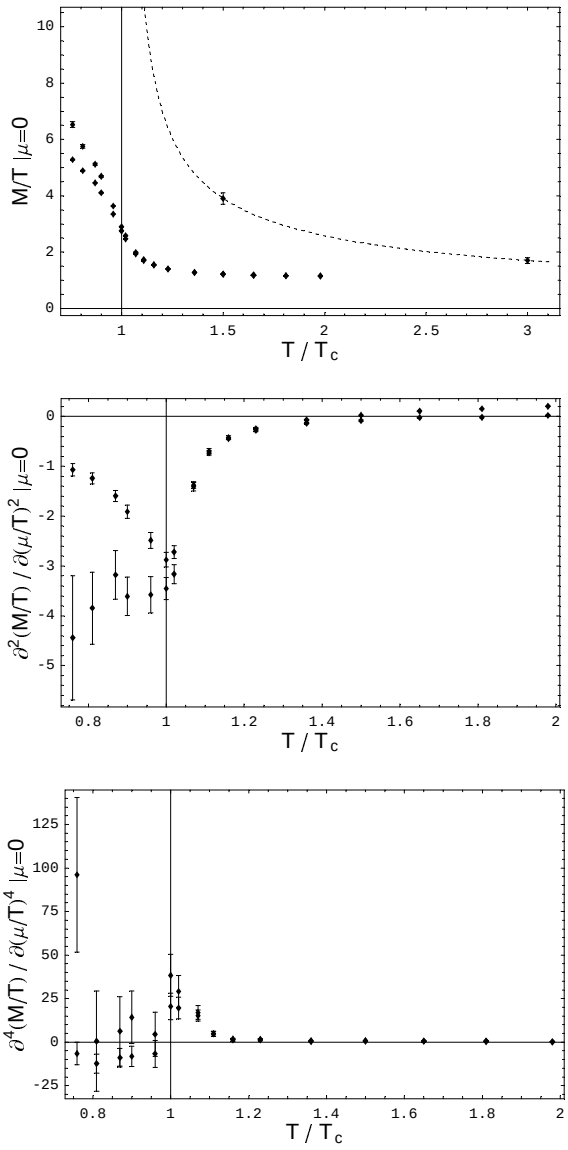

Figure 7.2: Quark quasiparticle mass and its second and fourth derivatives over μ as a function of temperature T, extracted from lattice data for susceptibilities. There are two sets of points in each figure that are obtained from c_2, c_4, c_6 and from c_2^I, c_4^I, c_6^I respectively. In the top figure for quark mass, we also plotted the two points with error bars measured by lattice via propagator, and the mass given by (7.20) as well. (the dashed line).

The results are shown in Fig.7.2. As can be seen, two sets of parameters we extracted from both data sets are well consistent with each other at $T > T_c$, while for $T < T_c$ they do not agree. It is a good feature, as the quark gas model is not supposed to work there, in the domain of the baryon resonance gas.

Let us summarize these results. The most important lessons are: (i) the mass $M(T)$ strongly increases when cooling down toward the critical point T_c; (ii) Large and *negative* $\frac{\partial^2 M}{\partial \mu^2}(T, \mu = 0)$ close to T_c; (iii) The 4-th derivative is positive: so this decrease of the mass due to the 2nd derivative will stop at about $\mu/T \sim 1$, see (7.15).

The first two points are the trends already emphasized by BKS [98]. In their approach these two features are related with each other because of the assumed perturbative origin of the effective quark mass:

$$M = g^2(T, \mu) T^2 \left(1 + N_f/6 + \frac{1}{2\pi^2 T^2} \sum_f \mu_f^2 \right) \tag{7.16}$$

where the sum runs over all flavors f. Ignoring for a moment a (rather complicated) running of the coupling, the BKS mass is thus constant at the particular ellipsoids in the $T - \mu$ plane, thus the derivatives over T and μ are related.

We would like to propose another reasoning that leads to similar effect, but is free from perturbative assumptions. Its idea can be described as follows: the quark mass should be getting large not only near the critical point $T \to T_c, \mu = 0$, but near the *whole critical line*, at all μ. It is needed to ensure that quark degrees of freedom do not contribute in the confined phase, at any μ.

The critical line at nonzero μ is schematically shown in Fig.7.3, its shape at not-too-large μ/T can be described by an ellipsoid, or an unit circle, if the units are chosen appropriately. One may further think that the mass dependence on the radial coordinate R on such a plot is much more important than on the angular one ϕ since the "lines of constant mass" should be nearly parallel to the critical line, at least in its vicinity where the discussed effect takes place.

So, the proposed extension of the T-dependence of the mass to its μ-dependence is based on a substitution

$$M(T, \mu = 0) \to M(R(T, \mu)) \tag{7.17}$$

$$R^2 = \frac{T^2}{T_c^2} + \frac{\mu^2}{\mu_c^2} \tag{7.18}$$

We have introduced here a new parameter μ_c: its value can be readily obtained from the experimental freezeout curve measured in heavy ion collisions at small

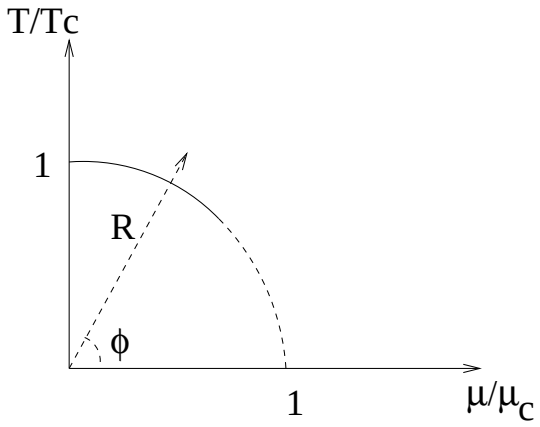

Figure 7.3: In the plane of temperature T-baryonic chemical potential μ, both appropriately normalized, the phase boundary looks like a part of a circle. (At least for the part marked by the solid line, studied well at SPS and RHIC, with quite well established chemical freezout. The dashed line is a continuation of the freezout line where its association with the critical line is questionable.) The polar coordinates to be used are the radial distance R and the angle ϕ.

μ, believed to represent the critical line. If so, the value of this parameter is

$$\mu_c/T_c = 1.7 \tag{7.19}$$

which is quite different from the value given by "perturbative scaling" (7.16): $\sqrt{(1+\frac{N_f}{6})\pi^2} \approx 3.63$ which is not supposed to work in the non-perturbative regime near T_c.

7.2 Model II: the constrained quark gas

The "unconstrained Model I" discussed above, although consistent with both data sets $d_n(T), d_n^I(T)$, is unfortunately unacceptable, for two main reasons: (i) It contradicts direct lattice measurements of the quasiparticle masses ; (ii) It implies that quark degrees of freedom still significantly contribute in the confining phase at $T < T_c$. In this section we will show what happens if one tries to modify the unconstrained model to make it compatible with both.

One feature of the Model I is the relatively light quark mass $M(T, \mu = 0)$ in region $1 - 2T_c$ ranging from about $1.7T_c$ to $2.2T_c$. Such mass conflicts with

another lattice data about quark quasiparticle mass at $1.5T_c$ and $3T_c$, see [100] which are $m_q/T = 3.9 \pm 0.2$ and $m_q/T = 1.7 \pm 0.1$, respectively, and are shown in Fig.2 by two crosses with the error bars. Although these results are based on only one paper and have not been systematically studied by other lattice groups so far, they nevertheless represent direct measurements from the quark propagators. Furthermore, such large masses correspond to the inter-particle potentials at large distances measured in separate lattice study [72].

Although the mass extracted via the Model I grows toward T_c, this effect is still not robust enough to make quark contribution near-zero (or negligible) at $T = T_c$. (In fact, BKS proceeded to fit equally well some region below T_c.) This is unacceptable, since we know that there are no propagating quark degrees of freedom in the confining phase.

Both these reasons force us to reconsider Model I, basically by increasing the quark mass significantly to meet both constraints. This can be achieved by a quark mass formula similar to that used in [21]

$$M(T) = \frac{0.9}{T-1} + 3.45 + 0.4T \tag{7.20}$$

with all units in proper powers of T_c (This and subsequent mass formula would then be generalized to finite μ according to (7.17) . The coefficients are chosen so that the curve goes through the two lattice-measured points for quark mass at $T = 1.5, 3.0\, T_c$, see the dashed line in Fig.7.2.

We show what happens then to the susceptibilities, see the medium-thickness solid lines in Fig.7.7. In short, good description of $c_2(T)$ is definitely ruined The issue is the same as for pressure in [21], and perhaps can be cured by qg and other bound states. But this is not the only problem of the constrained model: although it can produce a peak in $d_4(T)$ and a "wiggle" in $d_6(T)$, given large enough derivatives over μ, those get displaced toward larger T as compared to the data. It is an inevitable consequence of the second constraint, insisting that quark effect be effectively zero at T_c.[10]

Completing our discussion of purely quark models, we now proceed to the possible role of their bound states, diquarks and baryons.

[10]The very heavy mass due to the constraints significantly decrease quark contribution to thermodynamics and hence disfavor quark-only model, yet on the other hand, it strongly favors the formation of bound states.

Table 7.1: Summary of states with baryon number at $T > T_c$ studied in this Chapter.

state	spin	flavor	color	multiplicity
q	2	2	3	12
$(qg)_3$	4	2	3	24
$(qg)_6$	4	2	6	48
$(qq)_3^{J=I=0}$	1	1	3	3
$(qq)_3^{J=I=1}$	3	3	3	27
N	2	2	1	4
Δ	4	4	1	16

7.3 The effect of diquarks and baryons

We will now proceed to contributions of the bound states to the baryonic susceptibilities. Let us remind the reader that the particular reason to focus on diquarks and especially baryons is that the role of diquarks and baryons relative to quarks grows with μ because of their larger baryon charges. Alternatively, their contribution to the susceptibility d_n grows exponentially with n: by the factors 2^n for the diquarks and and 3^n for baryons. For example, the contribution of N, Δ is enhanced by a factor 81 for d_4 and 729 for d_6 relative to pressure: with estimates of pressure given above one may then expect to see their contribution there. On the other hand, for lower derivative d_2 we expect quark-gluon bound states, which are more numerous and more tightly bound, to contribute significantly. We summarized all bound states, together with their multiplicities, in the Table.7.1.

(In passing, let us comment about the numbers in the real world with strangeness, $N_f = 3$. The number of diquark flavor states is increased to be 3 times larger, for baryons the total spin-flavor multiplicity increases from 4+16=20 to 56(an octet $J = 1/2$ and a decuplet $J = 3/2$) which is roughly enhanced by 3 times, so the numbers both diquarks and baryons states are increased by the factor 3. The quark number increases as 3/2, so the overall enhancement of the ratios we will discuss below from $N_f = 2$ to $N_f = 3$ is the factor 2.)

Quark-gluon bound states: Before we proceed to actual calculation, let us make simple estimates of the relative weighing in pressure of quark-gluon bound states. The 2-body states qg are thermodynamically suppressed by additional Boltzmann factor, $exp(-M/T) \sim 0.02 - 0.04$ (by including their considerable binding). However, due to their relatively large multiplicity (6 times the number of the quark states) they contribute to the pressure and susceptibilities at the level of about 1/10 or more.

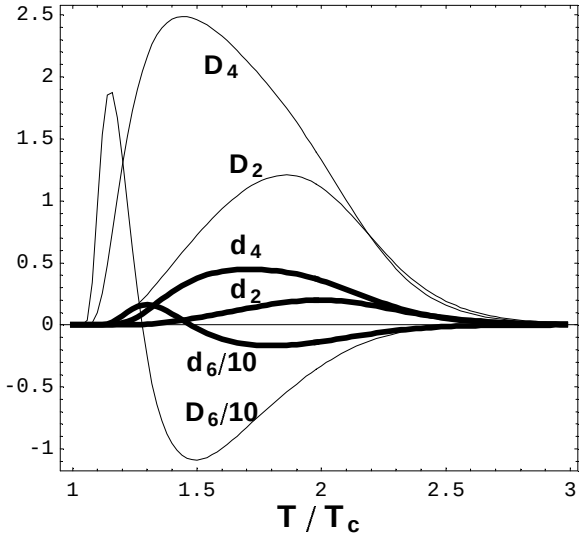

Figure 7.4: Comparison of susceptibilities from quark-gluon states with two limiting case, zero-binding ($d_{2,4,6}$) and "full-compensation" binding ($D_{2,4,6}$).

To get more quantitative answer one has to know the binding energy of these states. While the binding of the category three states $(qg)_6$ can be reasonably neglected, the category two $(qg)_3$ states have considerable binding at the same order as meson states. The potential model calculations in [22] lead to $(qg)_3$ binding up to $|\delta E|/T \approx 1.4$ at $T = T_c$, which means their contribution increases relative to simple estimate above by extra factor 2-3.

However there are many reason to doubt that close to T_c this calculation can be trusted quantitatively. In particular, the potential used is measured on the lattice for *static* charges only, and the corresponding calculations are supposed to be reliable only when the binding is small: near T_c more complicated dynamics beyond the potential model will contribute as well.

Let us thus just suggest an *upper limit* for the qg states' contribution. Since the qg states are colored, they should gets infinitely heavy at T_c, together with all other colored states. Furthermore, as (the more tightly bound) qg_3 states have the total charge of one quark, their mass should not be smaller than that of one charge $|\delta E| < M_q(T \approx T_c)$. So we expect $M(qg)$ to interpolate between $M_q + M_g \approx 2M_q$ at zero binding to a a single M_q at $T \approx T_c$). The contribution of these states to susceptibilities in the two limiting cases, namely the zero-binding case (labeled in figure by d_i) and "full-compensation" binding case (labeled by D_i), are shown in Fig.7.4. We conclude that large uncertainty, of

the order of factor 3, remains in the contributions of such states.

(These results are calculated with $(qg)_6$ always having twice quark mass and melting at $1.4T_c$ while with $(qg)_3$ having twice quark mass in the former case and the same mass as quark in the latter, both melting at $2.1T_c$. The actual contribution of quark-gluon bound states should be somewhere in between, near to D_i around T_c while rapidly decreasing to d_i for higher temperature.)

One may also ask what is the contribution of the various polymer-like qg states qg, qgg, $qggg, \cdots$ which, according to [22], has the same binding energy per bond. The effect of these states can be easily evaluated via a geometric series: the resulting enhancement factor is

$$f_{polymers} = \frac{1}{1 - 6exp[(|\delta E| - M_g)/T]} \tag{7.21}$$

where 6 is the color and spin degeneracy added by each link. For small binding this is just a few percent correction, but if it may get to be strong enough to drive the denominator toward zero, a total "polymerization" of sQGP would occur.

Diquarks: for $N_f = 2$ gauge theory corresponding to the UKB data at hand there is only one attractive diquark channel, the antisymmetric color triplet $(qq)_3$. Because of Fermi statistics, it means that the product of spin and flavor should be symmetric, and thus there are two options: (i) spin-0 isospin-0 ud diquark $(qq)_3^{J=I=0}$, and (ii) spin-1 isospin-1 one $(qq)_3^{J=I=1}$. These are the diquarks which are familiar in hadronic spectroscopy, the former appears inside the N, the latter inside Δ (octet and decuplet members, for 3 flavors). The lesson from this spectroscopy (at T=0, of course) is that while the former is well bound, by about 300 MeV, the latter is not. In view of the rather marginal character of diquark binding, we expect only the former one able to be seriously considered as bound state above T_c. Nevertheless to confirm the point that diquarks will not play any role in all susceptibilities measured, we include both of them in calculation of Fig.7.7. If we only use antisymmetric states, then the contribution will be reduced to only 1/10 of that.

The diquark-to-quark pressure ratio can be estimated as following:

$$\frac{(qq)_3}{q} \approx \frac{3+27}{12} exp(\frac{\mu - M + |\delta E|}{T}) 2^{3/2} \tag{7.22}$$

where the binding $|\delta E|$ is negligible (actually only the 3 $(qq)_3^{J=I=0}$ states are very likely bound)[11]. At small μ where the data under consideration are cal-

[11]The last factor comes from $M^{3/2}$ in the pre-exponent, originated from momentum integral.

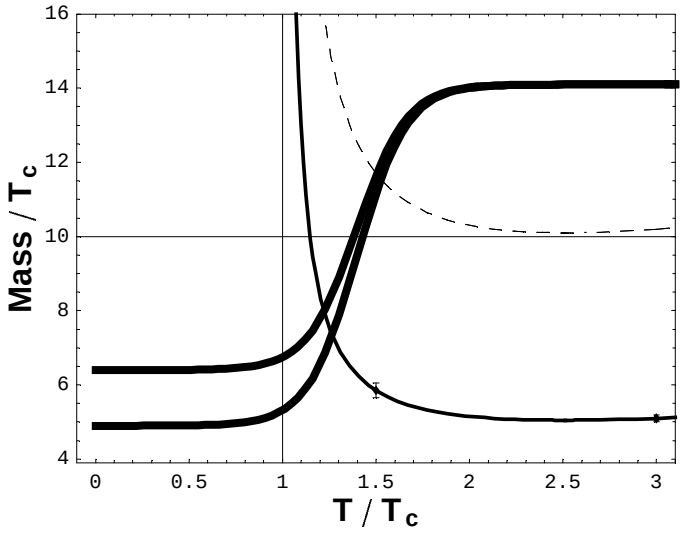

Figure 7.5: Masses of various states studied in this work. The thin solid line is for quark and the dashed line is twice quark mass which is roughly for quark-gluon and diquark. The lower thick solid line is for nucleon states and the upper one for Δ states. These masses are used for calculation of Fig.7.7.

culated, $M/T \approx 5$ and their contribution is at few percent level, negligible compared to uncertainties.

Baryons: as we found in [22] they are bound till about $T = 1.6T_c$. In the 2-flavor theory they are the N, Δ 3-quark states. Only the s-wave basic states survive above T_c, while all other resonances (used in the first section at $T < T_c$) which are orbital or radial excitations of N, Δ families are "melted".

The baryons are also numerous (20) but the suppression factor due to mass is much smaller

$$\frac{(qqq)}{q} \approx \frac{20}{12} exp(\frac{2\mu - 2M + |\delta E|}{T})3^{3/2} \tag{7.23}$$

Near the "endpoint" of baryons with zero binding (which according to [22] is at $T = 1.6Tc$) their mass is $3M_q$, expected to be in the range of 2.5- 3 GeV. As it is an order of magnitude larger than T, one would not expected to contribute to pressure etc.

However, unlike the quark, quark-gluon and diquarks (which after all are colored objects existing only above T_c), N, Δ baryons are colorless and thus survive on both sides of the boundary of (a continuous) phase transition (a crossover, more accurately), thus the masses of baryons at $T \to Tc$ are ex-

pected to join continuously to their known values at lower T. This of course implies that the binding energy near T_c gets very large due to some deeper yet poorly-known mechanism, and the potential model used in [22] to evaluate this binding will not be applicable. The situation is basically the same as with mesons: as emphasized in [21] the pion mass must (by definition of chiral breaking) vanish (in the chiral limit) at $T \to Tc$, which potential model also cannot reproduce. we will use below the following parameterization (in T_c units)

$$M_N = 9.5 + 4.6 * \tanh[3.8 * (T - 1.4)] \tag{7.24}$$

$$M_\Delta = 10.25 + 3.85 * \tanh[3.8 * (T - 1.4)] \tag{7.25}$$

interpolating between the nucleon and Δ vacuum masses at low T, while approaching the same value $3M_q$ at high temperatures. We plot it in Fig.7.5, together with the masses of various other states to be used in later in Fig.7.7 for susceptibilities. The main feature is fundamentally again enforcing confinement: when going from QGP side toward T_c, all colored degrees of freedom get extremely heavy and drop out from system, while all colorless degrees of freedom get more tightly bound and eventually dominate.

We now approach the central point of the paper: the baryon contribution provides a natural interpretation of the structures observed in susceptibilities measured on the lattice, the large peak near T_c in $d_4(T)$ and a more complicated "wiggle" structure is seen in $d_6(T)$. This happens because the expected mass dependence of baryons on T, μ, shown in Fig.7.5, should have a characteristic shape with an inflection point, separating the region in which the second derivative M_B'' is negative (above T_c) and positive (below T_c). That is why the contributions of the baryons to d_6 show a "wiggle" as seen from the corresponding curves in Fig.7.7. Note also, that there is a less pronounced wiggle of the same origin in baryonic d_4: we think its negative part is the reason why the qg and qq contributions above T_c can get compensated and by coincidence the d_4/d_2 ratio gets close to 1 there.

One additional argument for baryonic nature of the structures seen in d_4, d_6 is the following one. Each derivative over μ_q leads to factor 3, so 2 of them give 9. If instead one has two derivatives over μ_I the factor obtained is $(2I_3)^2$, which is 1 for p, n, Δ^+, Δ^0 and 9 for Δ^{++}, Δ^-. As a result, if one ignores the mass difference between these states, one finds that baryonic contribution to both should have the ratio $d_n^I/d_n = (1/9) * (4/20) + (1 + 1/9)(8/20) = .467$, while this ratio should be 1 for ideal quark gas. The actual ratio of these quantities according to UKB data are shown in Fig.7.6. We see near T_c the data obviously favor the existence of baryons, especially for d_6^I/d_6, and the quark asymptotic end is arrived at about $1.4T_c$ for d_4^I/d_4 while only after $1.8T_c$ for d_6^I/d_6. These evidences strengthen the necessity of baryonic interpretation

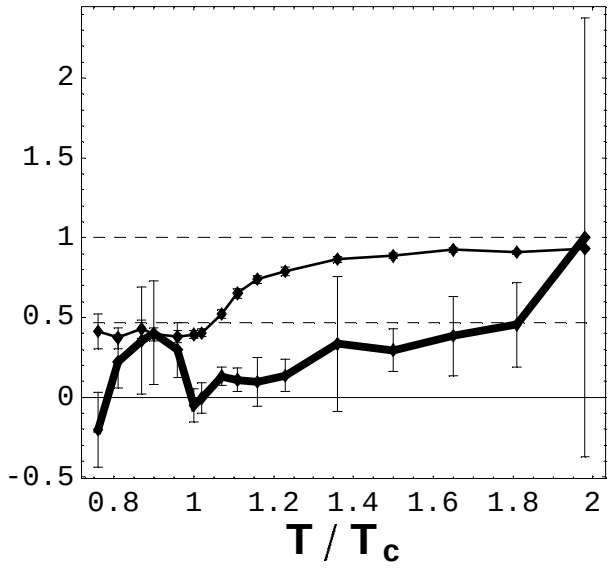

Figure 7.6: The susceptibilities ratios d_4^I/d_4 (the thin solid) and d_6^I/d_6 (the thick solid). The dashed lines correspond to ideal quark gas (upper) and ideal baryonic gas (lower).

of the higher susceptibilities.

Taking everything together, including quarks, quark-gluons, diquarks and baryons, we arrived at summary plots shown in Fig.7.7. We repeat that all masses used are as shown in Fig.7.5 and their $\mu-$dependence is introduced in the same way according to (7.17).

(The bound states' "endpoints" are set to be $2.1T_c$ for $(qg)_3$ quark-gluons, $1.4T_c$ for $(qg)_6$, $1.4T_c$ for diquarks, and $1.6T_c$ for baryons, according to [22]. The gradual removal near melting point is done by similar means as in [21]. The results are shown in Fig.7.7, where the overall values as well as the contributions of each kind of states are all present.)

Let's focus on the $T > T_c$ side. The conclusions are:
(i) as expected the diquark contribution is negligible for all three quantities even after including the suspect $(qq)_3^{J=I=1}$ states, but it is clearly growing as getting to higher derivatives;
(ii)For d_2 quark provides main contribution, and we emphasize the fitting will be much better if we include the large binding of qg states near T_c. We have shown above that large uncertainty in its binding, including polymers, would allow for a good fit here, which we decided not to do.

(iii) In d_4 it is precisely the baryons that produce the desired large peak near T_c till about $1.3T_c$ where quarks become important;
(iv) The baryons' contribution extremely dominant the behavior of d_6, especially the "wiggle" shape.

We conclude that two prominent structures, a peak in $d_4(T)$ and a "wiggle" in $d_6(T)$ are naturally reproduced by baryons.

7.4 Summary

In one sentence, the main lessons from the UKB susceptibilities is that the baryons $N\Delta$ do survive the QCD phase transition, but are rapidly becoming quite heavy across it.

More generally, the discussed data set on the baryonic and isospin susceptibilities at $T > T_c$ can be described in two different scenarios. (i) The first is a quark quasiparticle gas, with the effective mass which is strongly *decreasing* near the phase boundary into the QGP phase; (ii) the second is a picture including baryons with the mass rapidly *increasing* across the phase boundary toward QGP, to about $3M_q$.

The first scenario was already pointed out by BKS [98], while our discussion makes it a bit more general. Its attractive features notwithstanding, it suggests the values of the mass not large enough to accommodate the existing constraints from other lattice measurements. We also think it is not possible to have quark degrees of freedom in hadronic phase. Thus we conclude that success of such scenario is unlikely.

The second scenario, based on baryons, can provide another explanation of the main features of the data, namely the observed peak in $d_4(T)$ and a "wiggle" in $d_6(T)$. It also naturally explains the flavor-changing d_4^{ud}, d_6^{ud}, which are not small relative to flavor-diagonal ones. Last but not least, this scenario provides a desired continuity to the baryon resonance gas picture at $T < T_c$.

Although the susceptibilities $d_n(T)$ we used in this work are highly sensitive tools, they are quite indirect. Thermodynamical observable in general cannot tell the difference between "melting" baryons (getting unbound) and baryons remaining well bound but just getting too heavy: in both cases all one finds is that their contribution to thermodynamics effectively disappears. Besides, the ideal gas models used in these studies are probably too naive to claim really quantitative description of the data. One should instead study directly the spectral densities of the correlators of the appropriate baryonic currents (qqq) and see if there are baryonic peaks there, like what has been done for charmonium and light mesonic channels. Only such direct measurements would tell

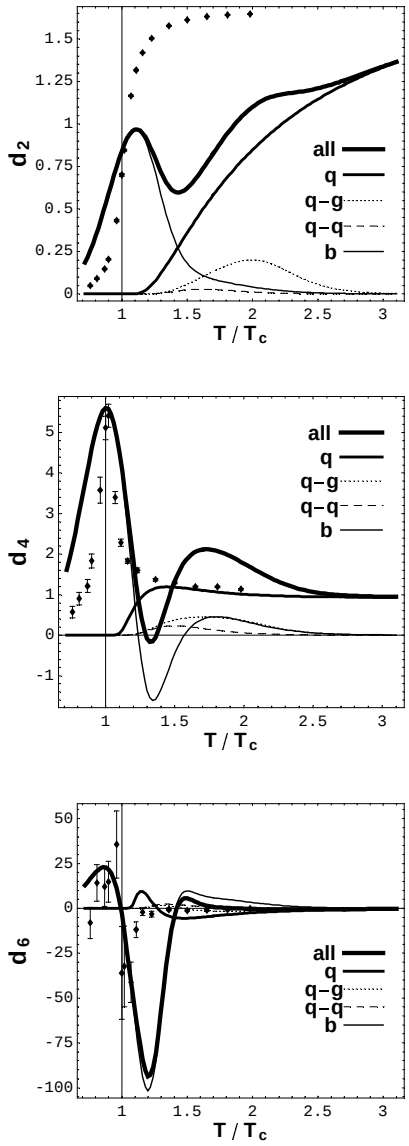

Figure 7.7: The contributions of different states to (a) d_2, (b) d_4 and (c) d_6, as well as the summed total values. The thickest solid lines are for taking all together, while the medium solid lines for quark, the thin solid lines for baryon, the dotted lines for quark-gluon, and the dashed lines for diquark, respectively.

us which scenario is the correct one.

Speaking about experimental confirmation of the "bound state" scenario, we think the best chance could be observation of the vector mesons. As described in detail in [101], vector mesons ρ, ω, ϕ are expected to become heavy near their disappearence point, like the baryons discussed above, reaching the mass $\approx 2M_q = 1.5 - 2\,GeV$. The next generation of RHIC dilepton experiments have a chance to see if this is indeed what is happening in QGP.

Chapter 8

Conclusions

In this dissertation, we have proposed to view finite-T QCD as a competition between electrically charged quasiparticles (EQPs) and the magnetically charged (MQPs). The high-T/high density limit is known to be perturbative QGP, which is electric-dominated. This implies that EQPs are more numerous, with density $\sim N_c^2 T^3$, while the density of MPQs is $\sim N_c^2 T^3/log^3(T/\Lambda_{QCD})$. In this case the electric coupling is *weaker* than the magnetic $e < g$. We have conjectured, based on a few lattice results, that at some intermediate $T \sim 300\,MeV$ both sectors' couplings and densities are similar, and below it $T < 300\,MeV$ the roles are reversed, with dominant MQPs and electric coupling being *stronger* than magnetic $e > g$. One of the important consequences of this picture is "postconfinement" phenomena and (electrically) strongly coupled QGP right above the deconfinement phase transition $T = (200 - 300)\,MeV$.

Using these ideas as a motivation, we have started a program of studies aimed at understanding the many-body aspects of matter composed of both electrically and magnetically charged quasiparticles.

We began in Chapter 2 with single monopole motion in the presence of certain electric field configurations, i.e. a static electric dipole and an electric flux tube. By studying the dipole case, we demonstrated how the monopole could be trapped locally for a long time and bounced back and forth between the two standing charges, an effect that later has been shown to be crucial for the transport properties. The monopole scattering on an electric flux tube has been solved exactly and the induced magnetic current calculated.

We have then used molecular dynamics in Chapter 3 to do the first systematic study of a plasma with both electric and magnetic charges. The correlation functions and the transport coefficients have been evaluated and compared among plasmas with different magnetic contents. Most interestingly we found that by increasing the concentration of magnetic charges to about

50% we get a factor 2 down for viscosity, which is particularly important in view of explaining the surprisingly low viscosity of sQGP as observed at RHIC.

In Chapter 4, by applying the results of our MD simulations to the sQGP system, we have concluded that the transport properties of the "perfect liquid" created at RHIC could be mimicked by our 50%-50% mixture with $\Gamma \approx 3$. We have then further elucidated the microscopic mechanism, i.e. the Lorentz trapping effect, which makes the mixture plasma a good liquid. Separately the analysis of the monopole-anti-monopole equal-time spatial correlation function has confirmed the monopoles indeed form a liquid. Further investigation of the accurate lattice data of this correlation function has helped us to extract important information about the magnetic coupling, which again suggests that the magnetic component in $1 - 4T_c$ is a good liquid.

As an application of the above magnetic scenario, in Chapter 5 we have developed a model for the static $\bar{Q}Q$ potential energy at $T \approx T_c$. In particular we have argued that the fast separation of the two charges will dynamically excite the dense magnetic medium and create meta-stable elongated flux bag which leads to the linear part in the potential with effective tension as large as about 5 times the vacuum string tension. Based on our model we have derived a formula which relates the effective tension of the linear part in the potential energy to the monopole density: by our formula consistency has been achieved between the lattice data for the tension and the independent lattice data for the monopole density.

Finally in Chapter 6 and 7 we have re-examined the electric component of sQGP, especially the roles of quark quasiparticles and their possible bound states. Using a potential model calculation we have shown that multiple-body bound states, e.g. baryons and polymer chains, could survive up to $1.6 - 2T_c$. Using the accurate lattice data of baryonic susceptibilities as a powerful diagnostic tool, we have been able to show that quark quasiparticles have to become rather heavy, at least about $4T$, when going close to T_c, and thus thermodynamically play a minor role, while the diquarks and baryons (heavy too but carrying more baryonic numbers) have to be included in order to explain the nontrivial structures in the higher-order susceptibilities. This study also indirectly supports our idea that the magnetic component is the most dominant degrees of freedom close to T_c.

To sum up in one sentence, the works presented in this dissertation have laid down the foundation toward a final and deep theoretical understanding of the strongly coupled quark-gluon plasma based on generic electric-magnetic duality. We believe as time evolves, with more and more dedicated and accurate lattice results coming out, and with more and more RHIC data and related phenomenological studies converging, the magnetic scenario for sQGP

which we suggest will gain more and more success, and the values of the many parameters characterizing the magnetic component (and the electric component as well) of sQGP will be more and more precisely determined.

Bibliography

[1] E. V. Shuryak. *The QCD Vacuum, Hadrons and Superdense Matter*. World Scientific Lecture Notes in Physics, 2004.

[2] Edward V. Shuryak. Theory of Hadronic Plasma. *Sov. Phys. JETP*, 47: 212–219, 1978.

[3] Edward V. Shuryak. SUPPRESSION OF INSTANTONS AS THE ORIGIN OF CONFINEMENT. *Phys. Lett.*, B79:135, 1978. doi: 10.1016/0370-2693(78)90453-7.

[4] Larry D. McLerran and Raju Venugopalan. Gluon distribution functions for very large nuclei at small transverse momentum. *Phys. Rev.*, D49: 3352–3355, 1994. doi: 10.1103/PhysRevD.49.3352.

[5] Larry D. McLerran and Raju Venugopalan. Computing quark and gluon distribution functions for very large nuclei. *Phys. Rev.*, D49:2233–2241, 1994. doi: 10.1103/PhysRevD.49.2233.

[6] K. Adcox et al. Formation of dense partonic matter in relativistic nucleus nucleus collisions at RHIC: Experimental evaluation by the PHENIX collaboration. *Nucl. Phys.*, A757:184–283, 2005. doi: 10.1016/j.nuclphysa.2005.03.086.

[7] John Adams et al. Experimental and theoretical challenges in the search for the quark gluon plasma: The STAR collaboration's critical assessment of the evidence from RHIC collisions. *Nucl. Phys.*, A757:102–183, 2005. doi: 10.1016/j.nuclphysa.2005.03.085.

[8] I. Arsene et al. Quark gluon plasma and color glass condensate at RHIC? The perspective from the BRAHMS experiment. *Nucl. Phys.*, A757:1–27, 2005. doi: 10.1016/j.nuclphysa.2005.02.130.

[9] The PHOBOS perspective on discoveries at RHIC. *Nucl. Phys.*, A757: 28–101, 2005.

[10] Edward Shuryak. Why does the quark gluon plasma at RHIC behave as a nearly ideal fluid? *Prog. Part. Nucl. Phys.*, 53:273–303, 2004. doi: 10.1016/j.ppnp.2004.02.025.

[11] Edward V. Shuryak. What RHIC experiments and theory tell us about properties of quark-gluon plasma? *Nucl. Phys.*, A750:64–83, 2005. doi: 10.1016/j.nuclphysa.2004.10.022.

[12] Miklos Gyulassy and Larry McLerran. New forms of QCD matter discovered at RHIC. *Nucl. Phys.*, A750:30–63, 2005. doi: 10.1016/j.nuclphysa.2004.10.034.

[13] E. V. Shuryak. Strongly coupled quark-gluon plasma: The status report. 2006.

[14] Edward Shuryak. Quark-Gluon Plasma - New Frontiers. 2008.

[15] D. Teaney, J. Lauret, and Edward V. Shuryak. Flow at the SPS and RHIC as a quark gluon plasma signature. *Phys. Rev. Lett.*, 86:4783–4786, 2001. doi: 10.1103/PhysRevLett.86.4783.

[16] Derek Teaney. Effect of shear viscosity on spectra, elliptic flow, and Hanbury Brown-Twiss radii. *Phys. Rev.*, C68:034913, 2003. doi: 10.1103/PhysRevC.68.034913.

[17] P. F. Kolb, P. Huovinen, Ulrich W. Heinz, and H. Heiselberg. Elliptic flow at SPS and RHIC: From kinetic transport to hydrodynamics. *Phys. Lett.*, B500:232–240, 2001. doi: 10.1016/S0370-2693(01)00079-X.

[18] Peter F. Kolb and Ulrich W. Heinz. Hydrodynamic description of ultra-relativistic heavy-ion collisions. 2003.

[19] Edward V. Shuryak and Ismail Zahed. Rethinking the properties of the quark gluon plasma at T approx. T(c). *Phys. Rev.*, C70:021901, 2004. doi: 10.1103/PhysRevC.70.021901.

[20] Hendrik van Hees, Vincenzo Greco, and Ralf Rapp. Thermalization and flow of heavy quarks in the quark-gluon plasma. *AIP Conf. Proc.*, 842: 77–79, 2006.

[21] Edward V. Shuryak and Ismail Zahed. Towards a theory of binary bound states in the quark gluon plasma. *Phys. Rev.*, D70:054507, 2004. doi: 10.1103/PhysRevD.70.054507.

[22] Jinfeng Liao and Edward V. Shuryak. Polymer chains and baryons in a strongly coupled quark- gluon plasma. *Nucl. Phys.*, A775:224–234, 2006. doi: 10.1016/j.nuclphysa.2006.06.169.

[23] Boris A. Gelman, Edward V. Shuryak, and Ismail Zahed. Classical strongly coupled QGP I: the model and molecular dynamics simulations. *Phys. Rev.*, C74:044908, 2006. doi: 10.1103/PhysRevC.74.044908.

[24] Boris A. Gelman, Edward V. Shuryak, and Ismail Zahed. Classical strongly coupled QGP. II: screening and equation of state. *Phys. Rev.*, C74:044909, 2006. doi: 10.1103/PhysRevC.74.044909.

[25] P. Hartmann, Z. Donko, P. Levai, and G. J. Kalman. Molecular dynamics simulation of strongly coupled QCD plasmas. *Nucl. Phys.*, A774:881–884, 2006. doi: 10.1016/j.nuclphysa.2006.06.157.

[26] Paul A. M. Dirac. Quantised singularities in the electromagnetic field. *Proc. Roy. Soc. Lond.*, A133:60–72, 1931.

[27] S. Mandelstam. Vortices and quark confinement in nonabelian gauge theories. *Phys. Rept.*, 23:245–249, 1976. doi: 10.1016/0370-1573(76)90043-0.

[28] Gerard 't Hooft. Topology of the gauge condition and new confinement phases in nonabelian gauge theories. *Nucl. Phys.*, B190:455, 1981. doi: 10.1016/0550-3213(81)90442-9.

[29] Nathan Seiberg. Exact results on the space of vacua of four-dimensional SUSY gauge theories. *Phys. Rev.*, D49:6857–6863, 1994. doi: 10.1103/PhysRevD.49.6857.

[30] N. Seiberg and Edward Witten. Electric - magnetic duality, monopole condensation, and confinement in N=2 supersymmetric Yang-Mills theory. *Nucl. Phys.*, B426:19–52, 1994. doi: 10.1016/0550-3213(94)90124-4.

[31] Alexander M. Polyakov. Thermal Properties of Gauge Fields and Quark Liberation. *Phys. Lett.*, B72:477–480, 1978. doi: 10.1016/0370-2693(78)90737-2.

[32] Saumen Datta, Frithjof Karsch, Peter Petreczky, and Ines Wetzorke. Charmonium systems after the deconfinement transition. *J. Phys.*, G30:S1347–S1350, 2004. doi: 10.1088/0954-3899/30/8/124.

[33] M. Asakawa and T. Hatsuda. J/psi and eta/c in the deconfined plasma from lattice QCD. *Phys. Rev. Lett.*, 92:012001, 2004. doi: 10.1103/PhysRevLett.92.012001.

[34] Gunnar S. Bali. The mechanism of quark confinement. 1998.

[35] Y. Koma, M. Koma, Ernst-Michael Ilgenfritz, T. Suzuki, and M. I. Polikarpov. Duality of gauge field singularities and the structure of the flux tube in Abelian-projected SU(2) gauge theory and the dual Abelian Higgs model. *Phys. Rev.*, D68:094018, 2003. doi: 10.1103/PhysRevD.68.094018.

[36] M. Baker, James S. Ball, and F. Zachariasen. Dual QCD: A Review. *Phys. Rept.*, 209:73–127, 1991. doi: 10.1016/0370-1573(91)90123-4.

[37] Edward V. Shuryak. Quantum Chromodynamics and the Theory of Superdense Matter. *Phys. Rept.*, 61:71–158, 1980. doi: 10.1016/0370-1573(80)90105-2.

[38] A. Nakamura, T. Saito, and S. Sakai. Lattice calculation of gluon screening masses. *Phys. Rev.*, D69:014506, 2004. doi: 10.1103/PhysRevD.69.014506.

[39] C. P. Korthals Altes. Magnetic monopoles in hot QCD. 2006.

[40] Thomas C. Kraan and Pierre van Baal. Exact T-duality between calorons and Taub - NUT spaces. *Phys. Lett.*, B428:268–276, 1998. doi: 10.1016/S0370-2693(98)00411-0.

[41] Ki-Myeong Lee and Piljin Yi. Monopoles and instantons on partially compactified D- branes. *Phys. Rev.*, D56:3711–3717, 1997. doi: 10.1103/PhysRevD.56.3711.

[42] Christof Gattringer, E. M. Ilgenfritz, and Stefan Solbrig. Cooling, smearing and Dirac eigenmodes: A comparison of filtering methods in lattice gauge theory. 2006.

[43] P. Gerhold, E. M. Ilgenfritz, and M. Muller-Preussker. An SU(2) KvBLL caloron gas model and confinement. *Nucl. Phys.*, B760:1–37, 2007. doi: 10.1016/j.nuclphysb.2006.10.003.

[44] R. D. Pisarski and L. G. Yaffe. THE DENSITY OF INSTANTONS AT FINITE TEMPERATURE. *Phys. Lett.*, B97:110–112, 1980. doi: 10.1016/0370-2693(80)90559-6.

[45] C. Montonen and David I. Olive. Magnetic Monopoles as Gauge Particles? *Phys. Lett.*, B72:117, 1977. doi: 10.1016/0370-2693(77)90076-4.

[46] Jinfeng Liao and Edward V. Shuryak. What do lattice baryonic susceptibilities tell us about quarks, diquarks and baryons at T ¿ T(c)? *Phys. Rev.*, D73:014509, 2006. doi: 10.1103/PhysRevD.73.014509.

[47] Jinfeng Liao and Edward Shuryak. Electric Flux Tube in Magnetic Plasma. *Phys. Rev.*, C77:064905, 2008. doi: 10.1103/PhysRevC.77.064905.

[48] Hugh Osborn. Topological Charges for N=4 Supersymmetric Gauge Theories and Monopoles of Spin 1. *Phys. Lett.*, B83:321, 1979. doi: 10.1016/0370-2693(79)91118-3.

[49] Jinfeng Liao and Edward Shuryak. Strongly coupled plasma with electric and magnetic charges. *Phys. Rev.*, C75:054907, 2007. doi: 10.1103/PhysRevC.75.054907.

[50] A. G. Goldhaber and W. P. Trower. Magnetic monopoles. *Am. J. Phys.*, 58:429–439, May 1990.

[51] Kimball A. Milton. Theoretical and experimental status of magnetic monopoles. *Rept. Prog. Phys.*, 69:1637–1712, 2006.

[52] J. D. Jackson. *Classical Electrodynamics*. Wiley, 3rd edition, 1998.

[53] Y. M. Shnir. *Magnetic Monopoles*. Berlin, Germany: Springer, 2005.

[54] Georges Ripka. Dual superconductor models of color confinement. 2003.

[55] J. P. Hansen and I. R. McDonald. *Phys. Rev.*, A11:2111, 1975.

[56] Jorge Casalderrey-Solana and Derek Teaney. Heavy quark diffusion in strongly coupled N = 4 Yang Mills. *Phys. Rev.*, D74:085012, 2006. doi: 10.1103/PhysRevD.74.085012.

[57] M. P. Allen and D. J. Tildesley. *Computer Simulation of Liquids*. Oxford, 1987.

[58] S. Tanaka and S. Ichimaru. *Phys. Rev.*, A34:4163, 1986.

[59] Jinfeng Liao and Edward Shuryak. Magnetic Component of Quark-Gluon Plasma is also a Liquid! 2008.

[60] Guy D. Moore and Derek Teaney. How much do heavy quarks thermalize in a heavy ion collision? *Phys. Rev.*, C71:064904, 2005. doi: 10.1103/PhysRevC.71.064904.

[61] Simon C. Huot, Sangyong Jeon, and Guy D. Moore. Shear viscosity in weakly coupled N = 4 super Yang-Mills theory compared to QCD. *Phys. Rev. Lett.*, 98:172303, 2007. doi: 10.1103/PhysRevLett.98.172303.

[62] P. M. Chesler and A. Vuorinen. Heavy flavor diffusion in weakly coupled N = 4 super Yang- Mills theory. *JHEP*, 11:037, 2006.

[63] P. Kovtun, D. T. Son, and A. O. Starinets. Viscosity in strongly interacting quantum field theories from black hole physics. *Phys. Rev. Lett.*, 94:111601, 2005. doi: 10.1103/PhysRevLett.94.111601.

[64] Alessio D'Alessandro and Massimo D'Elia. Magnetic monopoles in the high temperature phase of Yang- Mills theories. *Nucl. Phys.*, B799:241–254, 2008. doi: 10.1016/j.nuclphysb.2008.03.002.

[65] Lisa Randall, R. Rattazzi, and Edward V. Shuryak. Implication of exact SUSY gauge couplings for QCD. *Phys. Rev.*, D59:035005, 1999. doi: 10.1103/PhysRevD.59.035005.

[66] Jinfeng Liao and Edward Shuryak. Electric $\bar{Q}Q$ potentials at $T \approx T_c$ and magnetic component of QCD plasma. 2008.

[67] Gunnar S. Bali. QCD forces and heavy quark bound states. *Phys. Rept.*, 343:1–136, 2001. doi: 10.1016/S0370-1573(00)00079-X.

[68] J. Greensite. The confinement problem in lattice gauge theory. *Prog. Part. Nucl. Phys.*, 51:1, 2003. doi: 10.1016/S0146-6410(03)90012-3.

[69] P. Petreczky and K. Petrov. Free energy of a static quark anti-quark pair and the renormalized Polyakov loop in three flavor QCD. *Phys. Rev.*, D70:054503, 2004. doi: 10.1103/PhysRevD.70.054503.

[70] Olaf Kaczmarek, Frithjof Karsch, Edwin Laermann, and Martin Lutgemeier. Heavy quark potentials in quenched QCD at high temperature. *Phys. Rev.*, D62:034021, 2000. doi: 10.1103/PhysRevD.62.034021.

[71] O. Kaczmarek, F. Karsch, P. Petreczky, and F. Zantow. Heavy quark anti-quark free energy and the renormalized Polyakov loop. *Phys. Lett.*, B543:41–47, 2002. doi: 10.1016/S0370-2693(02)02415-2.

[72] Olaf Kaczmarek, Shinji Ejiri, Frithjof Karsch, Edwin Laermann, and Felix Zantow. Heavy quark free energies and the renormalized Polyakov loop in full QCD. *Prog. Theor. Phys. Suppl.*, 153:287–294, 2004. doi: 10.1143/PTPS.153.287.

[73] O. Kaczmarek, F. Karsch, P. Petreczky, and F. Zantow. Heavy quark free energies, potentials and the renormalized Polyakov loop. *Nucl. Phys. Proc. Suppl.*, 129:560–562, 2004. doi: 10.1016/S0920-5632(03)02641-0.

[74] Olaf Kaczmarek and Felix Zantow. Static quark anti-quark interactions at zero and finite temperature QCD. II: Quark anti-quark internal energy and entropy. 2005.

[75] Olaf Kaczmarek and Felix Zantow. Static quark anti-quark interactions in zero and finite temperature QCD. I: Heavy quark free energies, running coupling and quarkonium binding. *Phys. Rev.*, D71:114510, 2005. doi: 10.1103/PhysRevD.71.114510.

[76] Olaf Kaczmarek and Felix Zantow. Static quark anti-quark free and internal energy in 2- flavor QCD and bound states in the QGP. *PoS*, LAT2005:192, 2006.

[77] C. R. Allton et al. Thermodynamics of two flavor QCD to sixth order in quark chemical potential. *Phys. Rev.*, D71:054508, 2005. doi: 10.1103/PhysRevD.71.054508.

[78] D. Antonov, S. Domdey, and H. J. Pirner. A Heavy Quark-Antiquark Pair in Hot QCD. *Nucl. Phys.*, A789:357–378, 2007. doi: 10.1016/j.nuclphysa.2007.03.009.

[79] E. Megias, E. Ruiz Arriola, and L. L. Salcedo. The quark-antiquark potential at finite temperature and the dimension two gluon condensate. *Phys. Rev.*, D75:105019, 2007. doi: 10.1103/PhysRevD.75.105019.

[80] M. N. Chernodub and V. I. Zakharov. Magnetic component of Yang-Mills plasma. *Phys. Rev. Lett.*, 98:082002, 2007. doi: 10.1103/PhysRevLett.98.082002.

[81] M. N. Chernodub and V. I. Zakharov. Magnetic strings as part of Yang-Mills plasma. 2007.

[82] M. N. Chernodub et al. Topological defects and equation of state of gluon plasma. *PoS*, LAT2007:174, 2007.

[83] Jinfeng Liao and Edward Shuryak. Magnetic Component of Quark-Gluon Plasma. 2008.

[84] C. Wittig. The Landau-Zener Formula. *J. Phys. Chem.*, B109:8428, 2005.

[85] Adriano Di Giacomo. Monopole condensation and colour confinement. *Prog. Theor. Phys. Suppl.*, 131:161–188, 1998. doi: 10.1143/PTPS.131.161.

[86] Adriano Di Giacomo. Confinement of color: A review. 2003.

[87] J. Casalderrey-Solana, E. V. Shuryak, and D. Teaney. Conical flow induced by quenched QCD jets. *J. Phys. Conf. Ser.*, 27:22–31, 2005. doi: 10.1016/j.nuclphysa.2006.06.091.

[88] A. Chodos, R. L. Jaffe, K. Johnson, Charles B. Thorn, and V. F. Weisskopf. A New Extended Model of Hadrons. *Phys. Rev.*, D9:3471–3495, 1974. doi: 10.1103/PhysRevD.9.3471.

[89] Z. X. Wang and D. R. Guo. *Special Functions*. World Scientific, Singapore, 1989.

[90] M. Baker, N. Brambilla, Hans Gunter Dosch, and A. Vairo. Field strength correlators and dual effective dynamics in QCD. *Phys. Rev.*, D58:034010, 1998. doi: 10.1103/PhysRevD.58.034010.

[91] V. G. Bornyakov, E. M. Ilgenfritz, and M. Mueller-Preussker. Universality check of abelian monopoles. *Phys. Rev.*, D72:054511, 2005. doi: 10.1103/PhysRevD.72.054511.

[92] J. Carlson, John B. Kogut, and V. R. Pandharipande. A Quark Model for Baryons Based on Quantum Chromodynamics. *Phys. Rev.*, D27:233, 1983. doi: 10.1103/PhysRevD.27.233.

[93] K. Hubner, O. Kaczmarek, F. Karsch, and O. Vogt. Free energies of static three quark systems. 2004.

[94] N. Metropolis, A. W. Rosenbluth, M. N. Rosenbluth, A. H. Teller, and E. Teller. Equation of state calculations by fast computing machines. *J. Chem. Phys.*, 21:1087–1092, 1953.

[95] V. Koch, A. Majumder, and J. Randrup. Baryon-strangeness correlations: A diagnostic of strongly interacting matter. *Phys. Rev. Lett.*, 95: 182301, 2005. doi: 10.1103/PhysRevLett.95.182301.

[96] R. V. Gavai and Sourendu Gupta. Simple patterns for non-linear susceptibilities near T(c). *Phys. Rev.*, D72:054006, 2005. doi: 10.1103/PhysRevD.72.054006.

[97] S. Ejiri, F. Karsch, and K. Redlich. Hadronic fluctuations at the QCD phase transition. *Phys. Lett.*, B633:275–282, 2006. doi: 10.1016/j.physletb.2005.11.083.

[98] M. Bluhm, Burkhard Kampfer, and G. Soff. The QCD equation of state near T(0) within a quasi- particle model. *Phys. Lett.*, B620:131–136, 2005. doi: 10.1016/j.physletb.2005.05.083.

[99] Peter Levai and Ulrich W. Heinz. Massive gluons and quarks and the equation of state obtained from SU(3) lattice QCD. *Phys. Rev.*, C57: 1879–1890, 1998. doi: 10.1103/PhysRevC.57.1879.

[100] P. Petreczky, F. Karsch, E. Laermann, S. Stickan, and I. Wetzorke. Temporal quark and gluon propagators: Measuring the quasiparticle masses. *Nucl. Phys. Proc. Suppl.*, 106:513–515, 2002. doi: 10.1016/S0920-5632(01)01764-9.

[101] Jorge Casalderrey-Solana and Edward V. Shuryak. Can binary bound states in a strongly coupled quark gluon plasma be observed via dileptons and photons? 2004.